

Aerosol Vertical Exchange in the Convective Planetary Boundary Layer

Turbulent particle flux measurements with combined wind and aerosol lidar

Der Fakultät für Physik und Geowissenschaften
der Universität Leipzig
eingereichte

D I S S E R T A T I O N

zur Erlangung des akademischen Grades

DOCTOR RERUM NATURALIUM
Dr. rer. nat.

vorgelegt

von Diplom-Physiker Ronny Engelmann
geboren am 10. Februar 1978 in Guben

Leipzig, Mai 2009

Bibliographische Beschreibung:

Engelmann, K. Ronny

Aerosol Vertical Exchange in the Convective Planetary Boundary Layer:
Turbulent particle flux measurements with combined wind and aerosol lidar

Universität Leipzig, Dissertation

135 S., 147 Lit., 43 Abb., 8 Tab.

Referat:

In der vorliegenden Arbeit wurde der turbulente Vertikalfluss von Aerosolpartikeln anhand von Lidarmessungen ermittelt. Die entwickelte Methode ermöglicht es somit den vertikalen Austausch von Aerosolpartikeln in der planetaren Grenzschicht quantitativ zu untersuchen. Zunächst wurden räumlich und zeitlich hoch aufgelöste Profile des Vertikalwinds mit einem kohärenten Doppler-Windlidar und, parallel dazu, die optischen Aerosoleigenschaften mit einem Ramanlidar erfasst. Die beiden Systeme wurden für diesen Einsatz weiterentwickelt und synchron und in unmittelbarer Nähe zueinander am Leibniz-Institut für Troposphärenforschung betrieben.

Auf die so gewonnenen Datensätze, bestehend aus dem Vertikalwind und aus dem Partikelrückstreukoeffizienten mit einer zeitlichen Auflösung von 5 s, wurde die Eddykorrelationsmethode angewendet. Mit Hilfe eines Inversionsalgorithmus wurden dann aus den optischen Partikeleigenschaften bei verschiedenen Wellenlängen die mikrophysikalischen Eigenschaften abgeleitet. Es ergab sich ein Umrechnungsfaktor vom Partikelrückstreukoeffizienten in ein Gesamtpartikelvolumen, woraus sich letztendlich der Massenfluss bestimmen ließ. Die Anwendung der Methode beschränkte sich auf trockene Grenzschichten, da für diese Fälle hygroskopisches Partikelwachstum auszuschließen war.

Die Messungen für diese Arbeit fanden zwischen 2006 und 2007 statt. Die entwickelte Methode wurde zunächst für zwei unterschiedliche Fallbeispiele diskutiert. Die im Spätsommer (12.09.2006) gemessenen turbulente Partikel-Massenflüsse betrugen $0.5\text{--}2.5 \mu\text{g m}^{-2}\text{s}^{-1}$ im oberen Teil der konvektiven Grenzschicht. Ähnliche Werte von $1.0\text{--}3.0 \mu\text{g m}^{-2}\text{s}^{-1}$ ergaben sich auch für einen Frühlingstag (26.04.2007). Weiterhin wurde beobachtet, wie durch konvektive Prozesse neu herangetragene Partikel von der Grenzschichtoberkante heruntergemischt wurden. Dabei ergaben sich Werte um $-(1.0\text{--}1.5) \mu\text{g m}^{-2}\text{s}^{-1}$ für den Massenfluss.

Aus der Zusammenfassung dieser zwei und fünf weiterer Messungen ergab sich als Mittel von 27 einzelnen Flussprofilen ein aufwärts gerichteter Partikel-Massenfluss von $0.045 \pm 0.025 \text{ ms}^{-1}$ mal der mittleren Partikelmasse an der Oberkante der turbulenten Grenzschicht. Es konnte gezeigt werden, dass der gemessene Partikelfluss mit dem Wachstum der konvektiven Grenzschicht einhergeht.

Curriculum Vitae

Ronny Engelmann

Leibniz Institute for Tropospheric Research (IfT)
Permoserstraße 15
04318 Leipzig
Germany

Phone: +49 341 235 2941
Mobile: +49 176 23296996
E-mail: ronny@tropos.de

Academic Education:

- Since 06/2004 Ph.D. thesis at the IfT: *Aerosol Vertical Exchange in the Convective Planetary Boundary Layer: Turbulent particle flux measurements with combined wind and aerosol lidar*
- 10/2002 – 10/2003 Diploma thesis at the IfT: *Entwicklung eines Mini-Ramanlidar und Aufbau einer kombinierten Sende- und Empfangseinheit für ein Doppler-Wind-Lidar, (Development of a portable Raman lidar and setup of transmitting and receiving optics for a Doppler-wind lidar)*
- 10/1998 – 10/2003 Studies of physics at the Faculty of Physics and Earth Science in Leipzig, Germany

Research Projects:

- Since 2008 Autonome Messplattformen zur Bestimmung des Stoff- und Energieaustausches zwischen Ozean und Atmosphäre (OCEANET)
- 2008 Amazonian aerosol characterization experiment (AMAZE), Manaus, Brazil
- 2008 Saharan mineral dust experiment (SAMUM-2), Praia, Cape Verde
- 2006 Convective and orographically-induced precipitation study (COPS), Black Forest, Germany
- 2005 International Lindenberg campaign for assessment of humidity and cloud profiling systems and its impact on high-resolution modelling (LAUNCH-2005), northern Germany
- 2004 Pearl River Delta experiment (PRD), GuangDong Province, southern China

Publications:

- R. Engelmann, U. Wandinger, A. Ansmann, D. Müller, E. Žeromskis, D. Althausen, and B. Wehner, 2008: *Lidar observations of the vertical aerosol flux in the planetary boundary layer*. J. Atmos. Oceanic Technol., 25, 1296–1306.
- D. Althausen, R. Engelmann, H. Baars, B. Heese, A. Ansmann, D. Müller, M. Komppula, 2009: *Portable Raman lidar PollyXT for automated profiling of aerosol backscatter, extinction, and depolarization*. J. Atmos. Oceanic Technol., revised version submitted.
- A. Ansmann, H. Baars, M. Tesche, D. Müller, D. Althausen, R. Engelmann, T. Pauliquevis, P. Artaxo, 2009: *Dust and smoke transport from Africa to South America: Lidar profiling over Cape Verde and the Amazon rainforest*. Geophys. Res. Letts., 36, 2009GL037923.
- M. Tesche, A. Ansmann, D. Müller, D. Althausen, R. Engelmann, V. Freudenthaler, S. Groß, 2009: *Vertically resolved separation of dust and smoke over Cape Verde by using multiwavelength Raman and polarization lidars during SAMUM 2008*. 114, 2009JD011862.
- A. Ansmann, M. Tesche, P. Seifert, D. Althausen, R. Engelmann, J. Fruntke, U. Wandinger, I. Mattis, D. Müller, 2009: *Evolution of the ice phase in tropical altocumulus: SAMUM lidar observations over Cape Verde*. J. Geophys. Res., 2008JD011659, revised version submitted.
- H. Baars, A. Ansmann, R. Engelmann, D. Althausen, 2008: *Continuous monitoring of the boundary-layer top with lidar*. Atmos. Chem. Phys., 8, 7281–7296.
- M. Grzeschik, H. Bauer, V. Wulfmeyer, D. Engelbart, U. Wandinger, I. Mattis, D. Althausen, R. Engelmann, M. Tesche, A. Riede, 2008: *Four-dimensional variational data analysis of water vapor Raman lidar data and their impact on mesoscale forecasts*. J. Atmos. Oceanic Technol., 25, 1437–1453.
- M. Wendisch, O. Hellmuth, A. Ansmann, J. Heintzenberg, R. Engelmann, D. Althausen, H. Eichler, D. Müller, M. Hu, Y. Zhang, 2008: *Radiative and dy-*

namic effects of absorbing aerosol particles over the Pearl River Delta, China. Atmos. Env., 42, 6405–6416.

- Y. F. Cheng, A. Wiedensohler, H. Eichler, Y. Zhang, W. Birmili, E. Brüggemann, T. Gnauk, M. Tesche, H. Herrmann, A. Ansmann, D. Althausen, R. Engelmann, M. Wendisch, H. Su, M. Hu, 2008: Relative humidity dependence of aerosol optical properties and direct radiative forcing in the surface boundary layer of southeastern China. In: *Nucleation and Atmospheric Aerosols*, C. D. O'Dowd, P. E. Wagner, Eds., Springer, Netherlands, 489–493.
- S. Fan, B. Wang, M. Tesche, R. Engelmann, D. Althausen, J. Liu, W. Zhu, Q. Fan, M. Li, N. Ta, 2008: *Meteorological conditions and structures of atmospheric boundary layer in October 2004 over Pearl River Delta area.* Atmos. Env, 42, 6174–6186.
- M. Tesche, A. Ansmann, D. Müller, D. Althausen, R. Engelmann, M. Hu, Y. Zhang, Y., 2007: *Particle backscatter, extinction, and lidar ratio profiling with Raman lidar in south and north China.* Appl. Opt., 46, 6302–6308.
- D. Müller, M. Tesche, H. Eichler, R. Engelmann, D. Althausen, A. Ansmann, Y. F. Cheng, Y. H. Zhang, and M. Hu., 2006: *Strong particle light absorption over the Pearl River Delta (south China) and Beijing (north China) determined from combined Raman lidar and Sun photometer observations.* Geophys. Res. Lett., 33, 2006GL027196.
- A. Ansmann, R. Engelmann, D. Althausen, U. Wandinger, M. Hu, Y. Zhang, Q. He, 2005: *High aerosol load over the Pearl River Delta, China, observed with Raman lidar and Sun photometer.* Geophys. Res. Lett., 32, 2005GL023094.

Conference Contributions:

- R. Engelmann, A. Ansmann, U. Wandinger, D. Althausen, D. Müller. *Measurements of turbulent particle fluxes in the dry CBL over a continental European site with combined wind lidar and multiwavelength Raman lidar*, 8th International Symposium on Tropospheric Profiling: Needs and Technologies, Delft, NL (2009), submitted.

- R. Engelmann, D. Althausen, D. Müller, M. Tesche, V. Lehmann. *Wind Profiles and Turbulent Particle Fluxes Measured with Lidar during LAUNCH 2005.*, 7th International Symposium on Tropospheric Profiling: Needs and Technologies, Boulder, USA (2006).
- R. Engelmann, D. Althausen, U. Wandinger, E. Žeromskis. *Coherent Doppler Wind Lidar for Aerosol Flux Measurements.*, 13th Coherent Laser Radar Conference, Kamakura, Japan (2005).
- R. Engelmann, P. Rhone, D. Althausen. *The Mini Raman Lidar 'Polly' - Setup and Experiments.*, 6th International Symposium on Tropospheric Profiling: Needs and Technologies, Leipzig, Germany (2003).
- R. Engelmann, P. Rhone, T. Müller, D. Althausen. *Das Mini-Ramanlidar Polly: Optischer Aufbau und Erprobung des Systems.*, Tagung der Deutschen Physikalischen Gesellschaft, Hannover, Germany (2003).

Acknowledgements

I would like to thank Jost Heintzenberg, Professor at the University of Leipzig, for giving me the opportunity to develop this thesis at the Leibniz Institute for Tropospheric Research. I enjoyed the warm, welcome, and, moreover, the inspiring atmosphere here.

Especially, I want to express my deepest gratitude to the people who had most of the *trouble* with me and my research—Ulla Wandinger, Albert Ansmann, and Dietrich Althausen. You always motivated me to look around, pushed me forward, and helped me to find my way back to the *red line*. This thesis would not have been performed without your engagement. Of course, your comments on the thesis were absolutely indispensable.

Furthermore, I want to thank Ina Mattis for introducing me into the calculation of the optical aerosol data. Without your help I still wouldn't know how to do the *magic*.

The inversion code of Detlef Müller was one of the main pillars of this PhD. I thank him for introducing me into the application of his code and for showing me how to review the results critically.

I really enjoyed working with Patric Seifert. Our joined project *lidar_eval_gui* would have never been completed without you. You spend loads of your time to enhance this computer program in order to derive the highly-resolved time series of the Klett solution in a very convenient way.

I personally thank Holger Linné who brought me onto the right course for the improvements of the Doppler lidar. Additionally, his various computer code fragments were extraordinary helpful.

I am specially grateful to Cornelia Kurze, Simone Schlecht, Gerd Freiberg, and Peter Glomb—the team of the mechanical workshop—who always had an open ear and a pair of skillful hands for my special wishes. Everything that came from their workshop left nothing to be desired.

Helgard Hube is the fairy godmother of the lidar group. She is the best lab assis-

tant in the world. She took care of all the little things that were necessary to setup, perform, and maintain the measurements.

Many more people at the IfT helped me in one way or the other. My special thank is to everyone who helped in order to perform and evaluate the time consuming measurements.

I want to thank Eike Bierwirth, a scientific colleague—but moreover a very close friend, for all his motivations, his comments on the thesis, and, of course, for all the entertaining evenings we spent playing Canasta.

Last but not least I want to thank my family—in particular my wife Ines for her extraordinary love and patience. She married me although I hadn't finished this thesis in time.

My parents, who always believed in me from their hearts, supported me with everything I could think of. I thank you for that.

'I am an old man now, and when I die and go to heaven there are two matters on which I hope for enlightenment. One is quantum electrodynamics, and the other is the turbulent motion of fluids. And about the former I am rather optimistic.'

Horace Lamb, 1932, in an address to the British Association for the Advancement of Science (Davidson, 2004, p. 24).

Table of Contents

1	Introduction	1
2	Turbulent planetary boundary layer	7
2.1	Turbulence	8
2.2	Vertical aerosol transport in the CBL	11
2.3	Turbulent flux	13
2.3.1	Concept of the eddy flux	14
2.3.2	Measurements of vertical fluxes by eddy correlation	15
2.3.3	Parameterization of the vertical turbulent flux	17
2.4	Mathematical concepts	19
2.4.1	Mean, variance, and correlation functions	19
2.4.2	Integral scale	20
2.4.3	Spectral examination of atmospheric measurements	22
3	Method—Aerosol flux measurements with lidar	25
3.1	Lidar measurements of aerosol optical properties	25
3.1.1	Light scattering in the atmosphere	25
3.1.2	Lidar principle	26
3.1.3	Determination of particle backscatter and extinction coefficients	27
3.2	Inversion with regularization	29
3.3	Wind measurements with coherent Doppler lidar	32
3.4	Aerosol flux measurements with lidar	34
3.5	Error analysis	37
3.5.1	Random errors	38
3.5.1.1	Sampling error	38

TABLE OF CONTENTS

3.5.1.2	Random errors of aerosol and wind lidar measurements	39
3.5.2	Systematic errors	40
3.5.2.1	Flux error	40
3.5.2.2	Vertical-wind-speed error	41
3.5.2.3	Errors of optical lidar data	41
3.5.2.4	Errors of microphysical properties	42
3.6	Measurement requirements	43
3.6.1	Length of the time series	43
3.6.2	Temporal resolution	43
3.6.3	Measurement accuracy of the vertical wind and the optical lidar data	44
3.6.4	Displacement of the sensors	44
3.6.5	Relative humidity	45
4	Instrumentation—Two co-located lidars	47
4.1	Aerosol Raman lidar MARTHA	47
4.1.1	System summary	47
4.1.2	Implementation of the analog channel	48
4.1.3	Error determination from an example measurement	50
4.2	Doppler lidar WiLi	51
4.2.1	Optical system setup	54
4.2.2	Laser pulse characterization	56
4.2.3	Data acquisition software	57
4.2.4	Peak finding and wind determination	60
4.3	Experimental setup	61
4.3.1	Synchronization and coherence of the datasets	61
4.3.2	Vertical beam alignment by use of specular reflections from ice crystals	63
5	Measurements and results	65
5.1	Case study of 12 September 2006	65
5.1.1	Synoptic situation	66
5.1.2	Lidar measurements	69

5.1.3	Microphysical parameters of aerosol particles	71
5.1.4	Spectral analysis	75
5.1.5	Vertical profiles of aerosol mass flux	78
5.1.6	Errors	80
5.2	Case study of 26 April 2007	81
5.2.1	Synoptic situation	81
5.2.2	Lidar measurements	81
5.2.3	Microphysical parameters of aerosol particles	89
5.2.4	Spectral analysis	92
5.2.5	Vertical profiles of aerosol mass flux	93
5.3	Further observations of dry CBL	95
5.3.1	Synoptic situations	96
5.3.2	Lidar measurements	96
5.3.3	Particle mass concentrations	99
5.3.4	Vertical profiles of the aerosol mass flux	99
5.4	Summary of results	107
5.5	Conclusions	109
6	Summary and outlook	113
	Bibliography	117
	List of symbols	133

1 Introduction

Climate change and air pollution have become major issues of atmospheric research. Anthropogenic aerosols are identified to play an important role because they influence the radiation budget of the Earth's atmosphere (direct aerosol effect), cloud evolution, cloud lifetime, and the formation of precipitation (indirect aerosol effects) as well as air quality (Heintzenberg and Charlson, 2009; Kahn et al., 2004; Anderson et al., 2003). The complexity of the chemical and physical properties of atmospheric particles and the large temporal and spatial variability of the aerosol characteristics are main reasons for the high uncertainties in our quantitative understanding of the role of atmospheric aerosol in environmental, weather and climate-relevant processes, and thus in the prediction of future climate (CCSP, 2009; IPCC, 2007).

An understanding and subsequent modeling of the complex influence of atmospheric particles requires the knowledge of the entire life cycle of the aerosol. This cycle includes the generation, the aging in terms of chemical transformation, coating, and mixing, the transport, and the removal of particles from the atmosphere. Most particles are generated at the Earth's surface due to dust emissions, particle formation from gaseous precursors, or stem from biomass burning and numerous anthropogenic emission sources. Various mechanisms are responsible for the vertical transport of aerosol which is the first step of long-distance transport and thus of the regional to intercontinental dissemination of natural and anthropogenic aerosol particles. Lifting of aerosol from the ground can be caused by deep convection and frontal passages, and occurs via turbulent processes in the planetary boundary layer (PBL).

Vertical exchange in general depends in a complicated way on surface characteristics and meteorological conditions in the PBL. These mechanisms within the PBL and in the turbulent transition layer between PBL and free troposphere, which is also known as the entrainment zone, are not well understood and thus are not well parameterized in atmospheric models.

The description of buoyancy-driven turbulence and the connected fluxes in the

convective boundary layer (CBL) has always been of special interest because the asymmetry of narrow, intense rising plumes versus low-intensity subsiding motions and non-local aspects, e.g., microfronts, dust devils, roll vortices (cloud streets), or hexagonal patterns of mesoscale cellular convection, complicate the situation (e.g., Kaimal et al., 1976; Wyngaard and Brost, 1984; Wyngaard and Weil, 1991; Wyngaard, 1992; Holtslag and Boville, 1993; Zilitinkevich et al., 1999). Furthermore, interpretations of *in situ* measurements of aerosol particle concentrations at the ground during unstable conditions often lack the information about the vertical transport, e.g., by the daytime dilution of the CBL or by downward mixing of aerosol particles from higher altitudes.

The vertical transport in the PBL is usually described by means of turbulent vertical fluxes and can be measured with the eddy-correlation technique. Such observations of particle fluxes covering the entire PBL and the entrainment zone are not easy to perform for three reasons.

Firstly, long averaging times are required for flux measurements to be statistically significant. But the planet's atmosphere is not stationary for arbitrary time scales. Thus the maximum time to average is predetermined by the diurnal variations in the PBL. This fact could be overcome by airborne measurements because large areas can be sampled in short time periods. Because of their immense costs airborne sensors can only be applied during special campaigns.

Secondly, fast sensors are required to determine turbulent fluxes. So far, turbulent aerosol fluxes have been investigated with *in situ* techniques only (e.g., Gallagher et al., 1997; Buzorius et al., 1998; Nilsson et al., 2001; Dorsey et al., 2002; Held, 2004; Buzorius et al., 2006; Schmidt and Klemm, 2008). Typically, an ultrasonic anemometer is applied together with a fast particle counter and fluxes of particle number concentration are derived. Although wind measurements can be performed quite quickly with this method, fast particle sampling in terms of aerosol mass concentration is still difficult. The required improvements in the *in situ* sampling technique are still ongoing (e.g., Shah and Cocker III, 2005; Wang et al., 2002; Graskow, 2001). Buzorius et al. (1998) have reported such ground-based aerosol flux measurements over a pine forest in southern Finland. These observations at ground are preferably conducted on towers below 100 m height. However, *in situ* measurements near the ground are representative for relatively small areas and can be used for describing local fluxes from very specific sources, e.g., a forest, a field, or an urban site. For

example, Dorsey et al. (2002) used the ground-based *in situ* method of Buzorius to derive particle fluxes and particle emission velocities above the city of Edinburgh, UK. They found reasonable correlations between the anthropogenic particle production caused by road traffic and the vertical particle flux. However, for the unstable boundary layer they found significant scatter in their data and speculate that downward mixing from particle production at higher altitudes may be the reason.

This directly refers to the third point: vertically resolved observations of the turbulence characteristics are needed to satisfactorily describe the relevant vertical exchange processes throughout the PBL. Flux profile observations throughout the PBL are representative of a much larger scale than surface measurements and can be used for the improvement of flux parameterizations in mesoscale and general circulation models. In a first step, the *in situ* technique has been applied already on an aircraft above an ocean surface (Buzorius et al., 2006).

Remote sensing is another approach for observations throughout the PBL. With state-of-the-art lidar technique the parameters of interest can be measured with high accuracy (<5%–10%) and with a high vertical resolution of the order of 50 m and a temporal resolution of a few seconds.

Remote measurements of turbulent fluxes in the planetary boundary layer were first shown by Senff et al. (1994). A water-vapor differential-absorption lidar (DIAL) was combined with a radar-RASS (RASS = radio acoustic sounding system) to simultaneously obtain the fluctuations of the water-vapor density and of the vertical wind velocity. From these data the turbulent latent-heat flux was derived by applying the eddy-correlation technique. Later the method was used to study ozone budgets (Senff et al., 1996). Turbulent water-vapor fluxes solely based on lidar measurements were shown by Giez et al. (1999), who combined a water-vapor DIAL with a Doppler wind lidar. Meanwhile, this approach is established and has been used from ground as well as on aircraft in several field campaigns (Linné et al., 2007; Kiemle et al., 2007). By applying the Doppler wind lidar technique one of the most limiting factors in the observation of vertical exchange phenomena, namely the lack of highly accurate measurements of the profile of the vertical wind component, could be overcome. Only with lidar, profiles of the vertical wind speed can be measured with an accuracy of $<10 \text{ cm s}^{-1}$ and with the required high resolution up to the top of the entrainment zone, i.e., up to 2–3 km height in summer.

Lidar also allows the observation of aerosol scattering properties throughout the

PBL with adequate spatial and temporal resolution. However, for the investigation of aerosol fluxes, not only optical aerosol properties, which control the radiative impact of the aerosol particles and possible feedbacks on the wind field, but also microphysical parameters such as particle number and mass concentrations are of primary interest. The application of the multiwavelength Raman lidar technique shows great potential in this context (Müller, 2007). This technique permits accurate determination of particle extinction and backscatter coefficients at several wavelengths. Particle surface-area and volume concentrations can be derived from the multiwavelength backscatter and extinction data with an inversion scheme (Müller et al., 2001).

A first successful feasibility study on the measurement of particle fluxes with lidar was presented by Wandinger et al. (2004). Combined measurements with the three-wavelength Raman lidar of the Leibniz Institute for Tropospheric Research (IfT) and the Doppler wind lidar of the Max Planck Institute for Meteorology were performed in Leipzig. Since the new Doppler wind lidar of the IfT was completed in 2005, this instrument has been used in conjunction with the IfT six-wavelength lidar (Althausen et al., 2000) in field campaigns such as the Convective and Orographically-induced Precipitation Study (COPS) in the Black Forest area in the summer of 2007 or the Saharan Mineral Dust Experiment (SAMUM-2) in Cape Verde in the winter and the summer of 2008. Also it has been operated together with the IfT three-wavelength Raman lidar (Mattis et al., 2002) during the AVEC (Aerosol Vertical Exchange) campaign for long-term observations of the PBL development under different meteorological conditions in flat terrain at the IfT site in Leipzig from March 2006 to May 2007 (Baars et al., 2008).

The aim of this work is the assessment of the vertical aerosol transport in the convective planetary boundary layer solely based on lidar measurements. For the first time, profiles of the vertical turbulent aerosol flux throughout the entire PBL are presented. The methodology for lidar measurements of turbulent aerosol fluxes by application of the eddy correlation technique was developed and adopted for this problem. In the first step I focus on the most simple case of a dry PBL (relative humidity $<60\%$) to avoid complications by hygroscopic growth of particles that can introduce unwanted effects in the vertical aerosol mass fluxes to be determined. The theory is presented in Chapters 2 and 3, where the vertical turbulent exchange is addressed in a more general manner first and afterwards the special application of the lidar technique to this problem is discussed. For successful measurements further im-

provements of the existing instruments became necessary. The needed hardware and software developments are fully addressed in Chapter 4. Chapter 5 presents the application of the developed method and the results from the measurements. In Chapter 6 a summary and the conclusions are given.

2 Turbulent planetary boundary layer

The planetary boundary layer is the lower part of the troposphere which is in contact with the planet's surface (see Garratt, 1992, for further details). Stull (1997, p. 2) defines it as 'that part of the troposphere that is directly influenced by the presence of the earth's surface, and responds to surface forcings with a timescale of about an hour or less.' The height of the PBL in mid-latitudes reaches from a few hundred meters in wintertime to 2–3 km in summer (e.g., Baars et al., 2008). Closer to the equator it can grow to heights of 5 km above ground at continental sites (e.g., Ansmann et al., 2008). Capped by a temperature inversion on the top, the PBL is separated from the free troposphere (FT) above.

The lowest few millimeters of the PBL where molecular diffusion determines the vertical exchange of heat, moisture, or momentum is called the *diffusion layer*. The *surface layer* or *Prandtl layer* covers the next tens of meters of height where a logarithmic wind profile can often be observed (Tennekes, 1973). The subsequent and major part to the top of the PBL is known as the *Ekman layer*. During daytime, turbulence in the Ekman layer causes vertical mixing. Therefore, this part of the PBL is also called the *mixing layer*. If respective sources are absent the mixing causes the mean values of potential temperature, momentum, humidity, and dry aerosol mass concentration to be constant throughout the PBL. Affected by surface friction the wind direction crosses the isobars close to the planet's surface and rotates towards the geostrophic wind at high altitudes. In contrast to the surface layer, the wind speed within the mixing layer is relatively constant.

The following chapter summarizes the basics of turbulence description in the atmosphere. At the beginning, a brief introduction on turbulence in the PBL is given. Then the mechanisms of vertical aerosol exchange processes in the mixing layer are described. In the following, the concept of the turbulent aerosol flux, which is the qualitative measure for the particle exchange processes in the PBL, is introduced. The general method for flux measurements—the eddy correlation technique—is briefly

described. Afterwards, parameterizations of the turbulent flux which are commonly used in atmospheric models are given. The required mathematical concepts which are used for the analysis of the data are introduced at the end of this chapter.

2.1 Turbulence

The three-dimensional turbulence in the PBL covers a large range of scales reaching from several tens of kilometers in organized cloud-roll structures down to the millimeter range where viscous energy dissipation occurs. However, this is only part of the entire spectrum of motions in the planet's atmosphere. Turbulent structures can be observed in synoptic weather systems and even up to global scales where the turbulence approaches two-dimensionality, which behaves quite differently (Tennekes, 1978). Van der Hoven (1957) used data sets of 43–60 hours and found a minimum in the turbulent spectrum at about 1 hour for surface winds between 30–125 m above ground level (agl). Figure 2.1 shows the results from his original work. At the low frequency range—on the order of four days—a peak from passages of large, synoptic-scale pressure systems occurs. Additionally, a small 12-hour peak was found in some of the data that were averaged to obtain the spectrum. The micrometeorological peak at high frequencies (30 s–3 min) is caused by turbulent motions within the PBL.

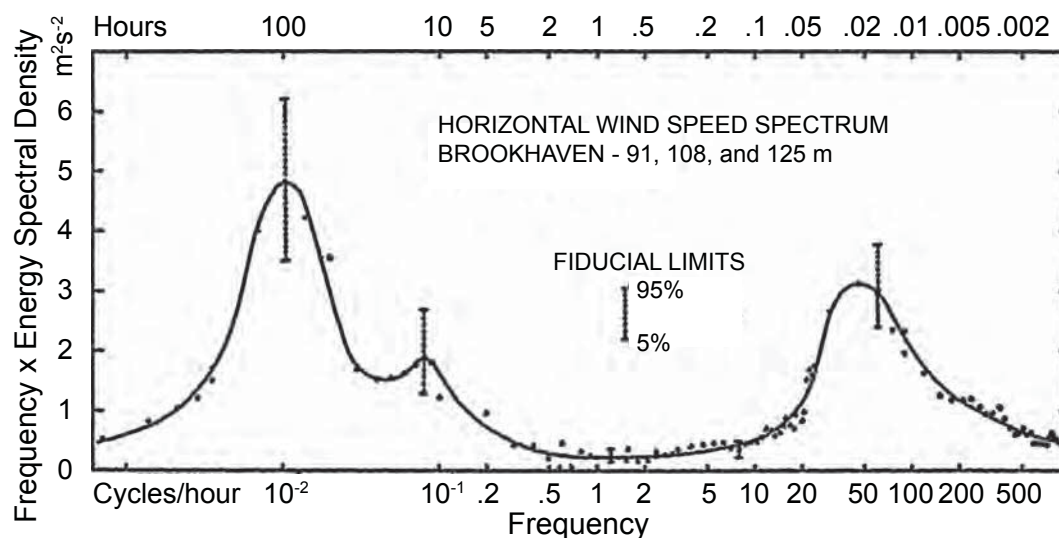


Figure 2.1: Generalized horizontal wind-speed spectrum measured at about 100 m height; after Van der Hoven (1957).

The fact that there is a spectral gap on the order of one hour is the underlying

concept for many measurements of turbulence in the PBL. It has become standard practice to treat dynamics faster than 1 hour as boundary layer turbulence. This is also found in the basic definition of the boundary layer after Stull (1997). Slower fluctuations are seen to be part of the meteorological mean field.

The turbulent structures of the PBL are either caused by mechanical or thermal processes. Mechanical turbulence is induced by wind shear, surface roughness, and friction or flows around obstacles. It can usually be observed close to the ground, in cities, in mountain regions, during periods with high wind speeds in the PBL, or on days with a stratus sky cover when solar radiation is attenuated. Thermal turbulence is observed on days with clear skies and medium wind speeds or if cold air is advected over a warmer surface (land or water). Then convection often dominates the generation of turbulence in the PBL. As the ground is heated by solar radiation warmer air parcels are formed and rise in updraft regions with $3\text{--}5\text{ ms}^{-1}$. These buoyant updrafts are also referred to as *thermals*. As a result of the conservation of mass cooler air parcels are forced to sink at the same time. These downdraft regions are usually larger with smaller downward wind speeds of $0.5\text{--}2\text{ ms}^{-1}$. When the generation of turbulence is dominated by buoyancy the mixed layer is also called a convective boundary layer (CBL).

The complex atmospheric flow is completely described by the Navier-Stokes equation with the boundary condition of the concept of continuity (Stull, 1997). These governing equations form a system of second-order non-linear partial differential equations which cannot be solved analytically in general. Therefore, simulation methods are applied for the solution. For a small degree of turbulence or for very small scales, i.e. for small Reynolds numbers of 50–100, the method of direct numerical simulation (DNS) is useful (Wyngaard, 1992). But for atmospheric flows with very high Reynolds numbers of 10^4 or more the amount of necessary grid cells is very high and the problem becomes unsolvable very rapidly. To overcome these numerical problems, different authors (e.g., Moeng and Wyngaard, 1984; Fedorovich et al., 2001; Helmert, 2003, and many others) have used large-eddy simulations (LES) where the large energy-containing eddies are simulated by an exact set of governing equations which describe the essential physics. The sub-grid eddies are assumed to follow the similarities of turbulence and therefore are modeled by means of approximates or parameterizations found from measurements (Wyngaard, 1992).

A common solution for the chaotic behavior of turbulence is the statistical de-

scription and the application of averaging over a certain regime x , what is commonly known as Reynolds averaging. A meteorological variable $\varphi(x)$ is described in this sense by an ensemble mean value and a turbulent fluctuation (see Kaimal and Finnigan, 1994; Stull, 1997, for further details):

$$\varphi(x) = \langle \varphi \rangle + \varphi'(x), \text{ with } \langle \varphi'(x) \rangle = 0, \quad (2.1)$$

where $\langle \varphi \rangle$ indicates the ensemble average over a volume which represents the statistical behavior completely. The fluctuation $\varphi'(x)$ is owed to the turbulence in the atmosphere.

The fluctuations of the components of the wind-velocity vector ($u_1, u_2, u_3 = w$) in horizontal and vertical direction constitute the energy of motions in a turbulent field. The turbulent kinetic energy (TKE) $E^{\text{kin,t}}$ per mass is given by

$$E^{\text{kin,t}} = \frac{1}{2} \left(\langle u_1'^2 \rangle + \langle u_2'^2 \rangle + \langle u_3'^2 \rangle \right). \quad (2.2)$$

In 1941 Kolmogorov showed that for stationary turbulence the TKE shows a characteristic spectral dependence. On large scales—in the spectrum's *energy containing part*—the energy is produced by shear, friction, or convection. The large vortices induce new turbulent structures at smaller scales on their outer boundaries. Thus the energy is not dissipated but reached down to smaller whirls by an *energy cascade*. This part of the spectrum is known as the *inertial subrange*. Within this range Kolmogorov found from self-similarity considerations and analysis of dimensions that the spectral energy density of the TKE follows a *-5/3rd power law* (Frisch, 1995):

$$\frac{dE^{\text{kin,t}}}{dk} = a_k \varepsilon^{2/3} k^{-5/3}, \quad (2.3)$$

where a_k is Kolmogorov's constant, ε the turbulent energy dissipation rate per mass and $k = 1/L$ is the wavenumber or the reciprocal value of the turbulent scale L . Lenschow and Stankov (1986) performed measurements and found that the inertial subrange begins at about 100–200 m in the PBL. The dissipation of energy to heat takes place on length scales of the order of 1 mm (*Kolmogorov microscale*) in the PBL because of viscosity, which predefines the end of the *-5/3rd* subrange.

It was found that energy spectra of many basic parameters that describe the state of

the atmosphere follow Kolmogorov's power law. Therefore, by plotting the energy spectrum (see Subsection 2.4.3) of a parameter ϕ' versus the wavenumber, or the frequency in case of a point measurement, in a log-log representation we can identify the inertial subrange by a linear slope of $-5/3$.

2.2 Vertical aerosol transport in the CBL

During daytime the scale of the energy-containing (and flux-carrying) eddies that are responsible for most of the mixing is typically on the order of the boundary-layer depth z_i . To some extent the eddies can be squeezed due to the confinement between the planet's surface and the temperature inversion at the CBL top. From measurements in the upper half of the CBL Kaimal et al. (1976) found values of about $1.5 z_i$ for the peak wavelength λ_{\max} in the spectrum of the vertical velocity w .

Figure 2.2 shows a schematic view of a transect through a dry CBL. The colors in this scheme refer to the mass concentration of an air constituent in general or of aerosol particles in our specific case. As warm and buoyant air rises, it transports the surface aerosol particles, whose concentration is usually higher, upwards. These *plumes* or *thermals* rise until they reach the temperature inversion at the top of the boundary layer. Additionally, clean air from the FT is mixed into the CBL and reduces the aerosol mass concentration at the ground. The layer between the highest thermal boundaries and deepest parts of sinking air from the FT is called the *entrainment zone* (EZ). Especially in the late morning, when the surface-layer temperature gradient becomes very strong, the entrainment process is very effective. At this time the CBL grows in a few hours almost to its complete depth. The combination of updrafts and downdrafts are referred to as *large eddies*. Additionally, these large eddies trigger a lot of smaller-scale eddies throughout the mixing layer following Kolmogorov's law. Consequently, the internal friction (precisely, the downward flux of momentum) influences the horizontal wind speed which becomes almost constant throughout the mixing layer.

However, with respect to aerosol the vertical transport is much more complicated than, e.g., the latent (water vapor) or sensible (temperature) heat flux. The ascent of particles is often combined with water uptake because of relative-humidity (r.h.) increase with height. This effect of hygroscopic growth is shown in Fig. 2.3. The am-

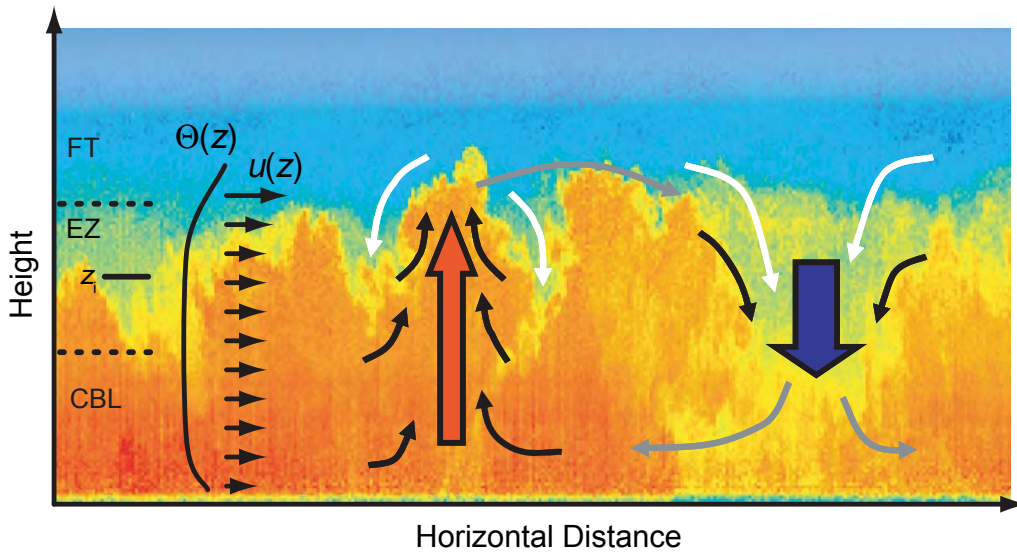


Figure 2.2: Schematic view of a transect through a dry CBL based on a time-height contour plot. In our case, the colors represent the aerosol mass concentration in the air. $\Theta(z)$ and $u(z)$ are the profiles of the potential temperature and horizontal wind speed, respectively.

bient particle mass concentration, optical and microphysical properties thus change with height during lifting processes even if the boundary layer is well mixed. If the deliquescence point were, for example, at 70% r.h. (e.g., Wexler and Seinfeld, 1991), hygroscopic growth of the particles would occur at the respective height levels. At a certain level of water-vapor supersaturation (usually at the PBL top) the swollen aerosol particles can be activated to cloud condensation nuclei (CCN). Subsequently, fast dynamic growth takes place. This rapid change from hygroscopic to dynamic growth is the onset of the cloud formation process (e.g., Pruppacher and Klett, 1997).

The cloud droplet size distribution sensitively depends on the amount of available aerosol particles, their chemical composition, and the aerosol flux into the cloud (Khain et al., 2000) and is thus sensitively dependent on the vertical wind at the cloud base. Subsequent cloud dissolution in downdrafts will affect the particle size distribution, volume and mass concentration, and the related optical effects, too.

Because of the r.h. hysteresis effect (e.g., Swietlicki et al., 1999; Tang and Munkelwitz, 1994) the hygroscopic growth factors are different for updrafts and downdrafts. In downdrafts the dry particle diameter might not be reached until the relative humidity drops significantly below 40%. Additionally, entrainment of free-tropospheric dry air is another factor that influences growth and shrinking of particles and thus the

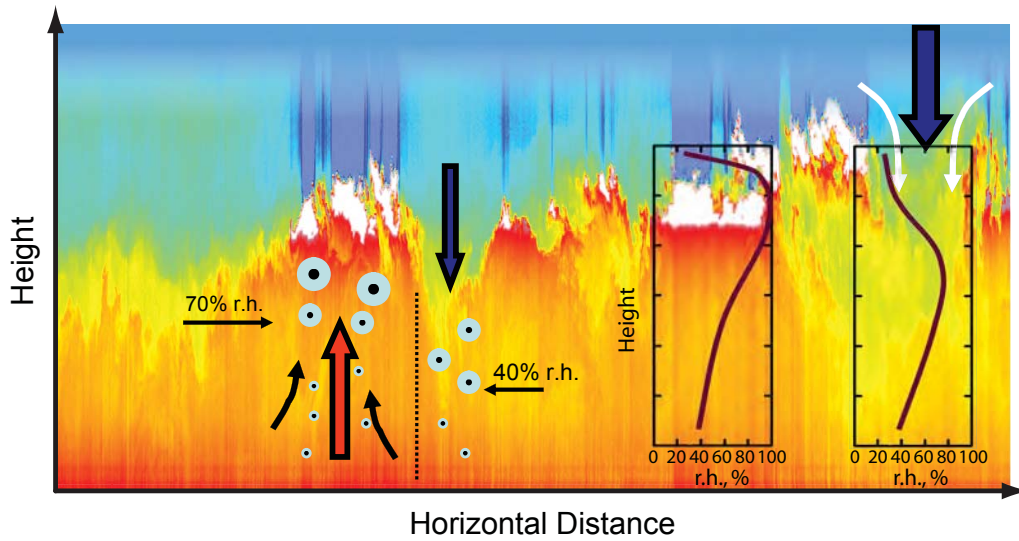


Figure 2.3: Turbulent mixing of aerosol in the humid CBL. The variable profiles of the relative humidity and the connected hygroscopic growth of particles are illustrated. The increase of the ambient aerosol mass concentration (dry aerosol mass+water) is color coded from blue to red. White colors represent boundary-layer cumulus clouds.

particle mass concentration. Because the dry air in the downdrafts is mixed with the PBL air it is uncertain where substantial shrinking of particles occurs.

All these processes are far away from being well understood because adequate observations are missing. This circumstance makes the description of aerosol, including the vertical transport, in atmospheric models very difficult and diverse (e.g., Textor et al., 2005; Kinne et al., 2006). As a consequence, the uncertainty in the estimation of the vertical aerosol exchange and the related direct and indirect aerosol effects remains rather high unless these aerosol-related processes are studied in detail based on measurements. This work is a first attempt to get more insight into these complex processes.

2.3 Turbulent flux

The transport of a quantity φ through an area A per time interval is given by the flux:

$$F_{\varphi}(t) = \frac{1}{A} \frac{d\varphi(t)}{dt} = c_{\varphi}(t) u_n(t), \quad (2.4)$$

where c_φ is the concentration of the quantity φ , and u_n is the velocity component perpendicular to the observed area. In the following, we will see that turbulence—although the mean value of u_n can vanish—is connected to real transport processes of meteorological quantities.

2.3.1 Concept of the eddy flux

Using Reynold's averaging for the instantaneous flux $F_\varphi(t)$ and separating the concentration $c_\varphi(t)$ and the velocity $u_n(t)$ into a mean and perturbation part we obtain:

$$\begin{aligned} F_\varphi &= \overline{F_\varphi(t)} = \overline{c_\varphi(t) u_n(t)} = \overline{\overline{c_\varphi} \overline{u_n} + \overline{c'_\varphi u'_n} + c'_\varphi \overline{u_n} + \overline{c'_\varphi u'_n}} \\ &= \overline{c_\varphi u_n} + \overline{c'_\varphi u'_n}, \end{aligned} \quad (2.5)$$

where the overbar indicates the temporal average of a measured time series. The mixed terms vanish because $\overline{c'_\varphi} = \overline{u'_n} = 0$. The two remaining terms are the advective flux resulting from the average motion of the air and the turbulent flux as the covariance of the fluctuations. Usually, horizontal transport processes in the PBL are dominated by advection, whereas the vertical exchange is primarily caused by turbulence since the average vertical velocity is much smaller than its fluctuations.

With respect to aerosol transport in the CBL, $c'_\varphi = m'$ for the fluctuations of the total aerosol mass concentration M_d . Looking back to Fig. 2.2, we find that upward (positive) vertical wind speeds w' correlating with positive fluctuations m' contribute to a positive turbulent particle flux F_p . Additionally, downward (or negative) vertical velocities correlate with cleaner air parcels from above, which contributes to a positive flux, too. Thus aerosol particles are vertically exchanged within the CBL although the average values $\overline{w'}$ and $\overline{m'}$ disappear. Both processes contribute in the same direction to the turbulent flux. In fact, Wyngaard and Brost (1984) showed that the vertical diffusion of passive or conservative scalars in the CBL is actually a superposition of what they call *bottom-up* and *top-down* diffusions. They substantiated their findings by LES and found the bottom-up transport substantially larger by a factor of 2–3 at $0.5 z_i$.

Considering a horizontally homogeneous area and stationary conditions we can assume that horizontal advection and sources or sinks of aerosol mass can be neglected. Then the temporal change rate of the aerosol mass concentration is only determined

by the gradient of the vertical turbulent flux:

$$\frac{\partial M_d}{\partial t} = -\frac{\partial \overline{m'w'}}{\partial z}. \quad (2.6)$$

We see that in this case there will only be a change in the aerosol mass concentration due to turbulence, if the turbulent flux profile is not constant with height.

2.3.2 Measurements of vertical fluxes by eddy correlation

Eddy correlation measurements are usually done with *in situ* instruments. This method of flux measurements of various parameters such as momentum, sensible and latent heat, or trace gases at ground levels is well established (Foken, 2003; Stull, 1997). For instance, various observations of CO₂ fluxes over a forest canopy have been made to study the carbon cycle. Surface flux networks and interdisciplinary research programs have been implemented in the past, e.g., Ameriflux (Law, 2005), CarboEurope (Dolman et al., 2006), Fluxnet (Baldocchi et al., 2001), and iLEAPS (Integrated Land Ecosystem—Atmosphere Processes Study, iLEAPS, 2005).

The vertical flux can be generally measured by the eddy correlation method as the covariance of the vertical-wind fluctuation w' and the fluctuation of a variable c' (in our case m'). If N measurements of the specific variables are taken, the flux can be calculated by

$$\overline{c'w'} = \frac{1}{N} \sum_{i=1}^N (c_i - \bar{c})(w_i - \bar{w}). \quad (2.7)$$

Atmospheric flux measurements are always bound to the averaging regime. There must be an agreement what scales are connected to fluctuations and what scales are treated as the mean flow. Usually, measurements deliver only limited series of data sets φ_n and ψ_n . For a sufficient amount of data points $n = 1..N$ the average of the data converges to the ensemble average:

$$\overline{\varphi'_n \psi'_n} \xrightarrow{N=\infty} \langle \varphi' \psi' \rangle. \quad (2.8)$$

There are two major limitations for the validity of the eddy correlation method. On the one hand, the sampling must be fast enough to cover the smallest scales of turbulence that contribute to a flux. On the other hand, the sampled data must represent

the area in a statistically significant manner and cover the large scales of turbulence. While such datasets can be obtained, for example, from LES, atmospheric measurements have certain limitations. Generally, atmospheric observations are a reasonable compromise between averaging times during which the turbulence can be assumed to be stationary and for which a full-scale coverage is given.

Another regular issue is that a time series is taken at a single point (e.g., on meteorological towers) instead of a spatial series at a fixed time. This problem was already addressed by Taylor (1938). What is known as *Taylor's hypothesis* states that the turbulence can be treated as *frozen* when it advects over a sensor. In this case the temporally averaged covariance equals its spatial average. Stationary turbulence within the averaging interval must be assumed therefore. However, this scenario is only true if the time scale of the eddies' evolution is much smaller than the time it takes for the eddies to pass the sensor (e.g., Stull, 1997). Taylor's formulation is the basic principle which connects the time or frequency scale of a variable to its spatial scale of wavelength or wavenumber, respectively, by use of the mean horizontal velocity. The equivalence of a spatial and a temporal measurement is also known as ergodicity.

To overcome this problem extremely fast turbulence sensors have been applied on airplanes or airborne platforms (e.g., Buzorius et al., 2006; Siebert et al., 2006). With their help large scales can be covered in a short time. However, Wyngaard (1992) emphasizes that flow-distortion effects can occur at airborne platforms and may be severe under certain conditions. Compressibility effects at airspeeds around 0.3 Mach can interact with the turbulent velocity and create *false fluctuations*.

In contrast, remote-sensing observations do not suffer from the distortion of the measurement volume. Lidar seems to be the preferred method for remote flux measurements in the PBL, because it allows observations in the undisturbed sample volume from ground or airborne platforms. In the recent years major advances in resolution of lidar systems have been made, so that various atmospheric parameters can be measured with time resolutions of several seconds and height resolutions of several meters.

For instance, during the International H₂O Project (IHOP_2002) Kiemle et al. (2007) operated a water-vapor DIAL and a Doppler lidar on board the DLR (Deutsches Zentrum für Luft- und Raumfahrt, German Aerospace Center) Falcon research aircraft over the U.S. Southern Great Plains. Latent heat flux profiles in the CBL were

successfully derived. They found significant contributions to the flux between 1 and 10 km wavelength, with peaks between 2 and 6 km, originating from large eddies. Although they applied airborne measurements, the sampling error was found to be 55% at a height of $0.5 z_i$ for flight legs of 12 km length. The instrument noise (15%) and systematic errors (7%) played a minor role (see Section 3.5 for the examination of the different error types).

2.3.3 Parameterization of the vertical turbulent flux

In atmospheric models the vertical component of the turbulent flux of a scalar variable φ can be parameterized at the height z by the local closure approximation or the K-theory:

$$F_\varphi(z) = \langle \varphi' w' \rangle = -K_\varphi \frac{\partial \langle \varphi(z) \rangle}{\partial z}. \quad (2.9)$$

The vertical flux is thus determined by the turbulent diffusion coefficient (or eddy diffusivity coefficient) K_φ and the local gradient of φ , only. This formulation is also referred to as small-eddy approach and is in complete analogy to the molecular diffusion theory (*Fick's first law*), although turbulent fluxes in the PBL are far larger than those due to molecular diffusion (by a factor of 10^5 , e.g., Wyngaard, 1992). The description above can be extended to the moments of the variable as well, in order to derive prognostic equations for the mean variables (1st order), the variances (2nd order), or even higher-order moments (see Helmert, 2003, for more details).

According to Eq. (2.9), a vanishing gradient of the mean variable implies a vanishing turbulent flux as well. This is valid and was found to be useful for modeling mechanical turbulence within the surface layer, stable daytime and nocturnal boundary layers. In contrast, observations and LES of convective situations have shown a different behavior (Wyngaard, 1992). In these cases, turbulent transport arises from much larger eddies which are not described by the local-closure schemes.

Consequently following these findings, Deardorff (1972) originated the counter-gradient approach. As a simple adoption of the above parameterization to the nonlocal formulation a counter-gradient γ_a is introduced:

$$F_\varphi = \langle \varphi' w' \rangle = -K_\varphi \left(\frac{\partial \langle \varphi \rangle}{\partial z} - \gamma_a \right). \quad (2.10)$$

This additional gradient takes the vertical large-eddy transport into account and leads to non-vanishing fluxes in the well-mixed CBL. Improved parameterizations for such cases where the concentration gradient is zero are given by Holtslag and Boville (1993) and Holtslag et al. (1995). Wyngaard and Weil (1991) found by LES, which qualitatively reproduced the scalar transport in the CBL, that the asymmetry in the bottom-up and top-down fluxes is determined by the skewness of the vertical velocity. They used a Taylor-series expansion for the scalar flux and changed Eq. (2.10) accordingly:

$$\begin{aligned} \langle \varphi' w' \rangle &= -K_\varphi \left(\frac{\partial \langle \varphi \rangle}{\partial z} - \frac{\tilde{S}_w \sqrt{\langle w'^2 \rangle} \Lambda}{2} \frac{\partial^2 \langle \varphi \rangle}{\partial z^2} + \dots \right) \text{ and with Eq. (2.9) :} \\ &\approx -K_\varphi \frac{\partial \langle \varphi \rangle}{\partial z} - \tilde{S}_w \frac{\sqrt{\langle w'^2 \rangle} \Lambda}{2} \frac{\partial \langle \varphi' w' \rangle}{\partial z}, \end{aligned} \quad (2.11)$$

where $\tilde{S}_w = \langle w'^3 \rangle (\langle w'^2 \rangle)^{-3/2}$ is the skewness of the vertical velocity and Λ is the integral time scale (Wyngaard, 1992). In contrast, $K_\varphi = \langle w'^2 \rangle \Lambda$ is proportional to the variance of the vertical velocity (Van Dop and Verver, 2001; Zilitinkevich et al., 1999). From the discussion above we see that the key role in large-scale nonlocal fluxes is played by the *fluxes of fluxes* represented by third (and higher-order) moments of the vertical wind.

At the center of the entrainment zone z_i the gradient between particle-rich air in the CBL and clean air in the FT is maximal. Therefore, the vertical flux of particle mass reaches its maximum at the height z_i . We call $F_{p,\text{entr}} = F_p(z_i)$ the *entrainment flux*. In a simple budget consideration, the mean entrainment flux equals the column particle mass divided by the time of the convective period t_{cp} :

$$F_{p,\text{entr}} = \frac{M_d \Delta z_i}{t_{\text{cp}}}, \quad (2.12)$$

where M_d is the mean aerosol mass concentration throughout the CBL and Δz_i the growth of the CBL during the convective period. The stable nocturnal surface layer would act as the particle source reservoir at the beginning of convection. Assuming an aerosol mass concentration of $20 \mu\text{g m}^{-3}$, a maximum CBL height of 1.5 km, and a convective period of 7 h an entrainment flux of $1.2 \mu\text{g m}^{-2} \text{s}^{-1}$ would be expected for this simple case. However, real processes in the CBL are far more complex.

For instance, formation of new particles, coagulation, deposition, chemical reactions, entrainment of lofted layers, and horizontal advection are important factors which influence the aerosol properties.

2.4 Mathematical concepts

Several mathematical methods and parameters are used for the determination of the turbulent aerosol flux, its error, and for the evaluation of the observations in Chapter 5. These parameters and related concepts are introduced next.

2.4.1 Mean, variance, and correlation functions

The average of a measured time series φ_n is denoted by an overbar (in contrast to the true ensemble average $\langle \varphi \rangle$ of a turbulent process):

$$\bar{\varphi} = \frac{1}{N} \sum_{n=0}^{N-1} \varphi_n, \quad (2.13)$$

where $N = T/\Delta t$ is the number of samples of the time series. T is the overall sampling time and Δt the sampling interval.

A measure of how far atmospheric variables $\varphi_n = \bar{\varphi} + \varphi'_n$ are correlated with themselves is the autocovariance function:

$$R_{\varphi\varphi}(l) = \overline{\varphi'_n \varphi'_{n+l}} = \frac{1}{N} \sum_{n=0}^{N-l-1} \varphi'_n \varphi'_{n+l}, \quad (2.14)$$

where l is called the *lag*. The *time lag* is given by $l\Delta t$. For the zero lag, $R_{\varphi\varphi}(l=0)$ equals the variance $\sigma_\varphi^2 = \overline{\varphi'^2}$ of φ_n . Normalizing $R_{\varphi\varphi}(l)$ by the variance results in the autocorrelation function:

$$r_{\varphi\varphi}(l) = \frac{R_{\varphi\varphi}(l)}{R_{\varphi\varphi}(0)} = \frac{\overline{\varphi'_n \varphi'_{n+l}}}{\sigma_\varphi^2}. \quad (2.15)$$

This function can also be defined for two series φ_n and ψ_n . In this case, $R_{\varphi\psi}(l)$ and $r_{\varphi\psi}(l)$ are called the covariance and the (cross-)correlation functions, respectively,

with

$$r_{\phi\psi}(l) = \frac{R_{\phi\psi}(l)}{\sigma_{\phi}\sigma_{\psi}} = \frac{\overline{\phi'_n\psi'_{n+l}}}{(\overline{\phi'_n\phi'_n}\overline{\psi'_n\psi'_n})^{1/2}}. \quad (2.16)$$

The quantities $R_{\phi\psi}(l=0) = R_{\phi\psi}$ and $r_{\phi\psi}(l=0) = r_{\phi\psi}$ are called the covariance and the correlation, respectively.

2.4.2 Integral scale

Various publications have shown that the integral scale is important for characterizing the structure of turbulence (Lenschow and Stankov, 1986; Giez, 1996; Lothon et al., 2006). It is a measure of the longest correlation distance between the flow velocity (or vorticity, etc.) at two points in the flow field (Hinze, 1975). Additionally, it is also a measure of *randomness* in the turbulence. Small values imply a highly random turbulence and large values imply a more structured turbulence with larger eddies (Treviño and Andreas, 2004). Lumley and Panofsky (1964) have shown that the integral scale is also an important factor for the error determination, i.e., given a specific error limit the required averaging length for the representative determination of turbulent parameters can be calculated.

The integral scale Λ_{ϕ} of a variable ϕ is defined as the integral of the autocorrelation function $r_{\phi\phi}(l)$. For real atmospheric measurements the integral has to be replaced by a sum over discrete values:

$$\Lambda_{\phi} = \Delta t \sum_0^{l \rightarrow \infty} r_{\phi\phi}(l). \quad (2.17)$$

Boundary-layer measurements at a fixed point give estimations of the integral *time* scale. By multiplication with the average horizontal wind speed and the assumption of stationarity (Taylor's hypothesis) we obtain the atmospheric integral *length* scale.

Kaimal and Finnigan (1994) point out that the autocorrelation function in the CBL can be approximated by an exponential function

$$r_{\phi\phi}(l) \approx \exp\left(-\frac{|l|\Delta t}{\Lambda_{\phi}}\right). \quad (2.18)$$

But own observations as well as reports from several other authors often have shown that the autocorrelation function of a measured atmospheric time series can reach

negative values or even oscillates around zero, which are indications for organized coherent structures within the CBL (Yaglom, 1977; Lumley and Panofsky, 1964; Helmert, 2003). Hence the integration is usually performed to the first zero crossing point of $r_{\varphi\varphi}(l)$ (e.g., Lenschow and Stankov, 1986; O'Neill et al., 2004). Hereafter, the same method is applied for the calculation of the integral scale.

A cross-correlation function (like the vertical flux of an air constituent $\overline{w'_n c'_n}$) within the CBL is much less suitable for the calculation of the integral scale $\Lambda_{w,c}$ with Eq. (2.17), because the cross-correlation is not symmetric in general. The *flux integral scale* can also converge to negative values, e.g., in case of a negative flux. Hence Giez et al. (1999) suggested the conservative upper bound

$$\Lambda_{w,c} < \min(\Lambda_w, \Lambda_c) \quad (2.19)$$

for the flux integral scale. For further investigations the flux integral scale was replaced by the integral scale of the vertical wind or of the aerosol parameter, respectively, since the flux integral scale was used for the error calculation of the vertical flux (see Section 3.5).

Lenschow and Stankov (1986) derived height-dependent parameterizations for the integral length scales from aircraft measurements over the ocean during AMTEX (Air Mass Transformation Experiment, East China Sea, 1974 and 1975). In general, Λ was increasing with height. For the integral length scale of the vertical wind they found

$$\Lambda_w(z) = 0.24\sqrt{z z_i}. \quad (2.20)$$

For scalar fluxes of heat, humidity, and ozone they suggested the parameterization

$$\Lambda_{w,c}(z) = 0.16\sqrt[3]{z z_i^2}. \quad (2.21)$$

That means that for a given height z_i of the CBL of 1500 m we expect the integral scale of the vertical wind to be on the order of 250 m at the center of the CBL. The flux integral scale at the same height level would be about 190 m.

Recently, horizontal and vertical integral scales of the vertical wind were published by Lothon et al. (2006) and Lenschow et al. (2006). The measurements were taken with a Doppler lidar during LIFT (Lidars In Flat Terrain, central Illinois, USA, 1996). The integral scales were similar to the prior parameterization in the center of the CBL.

However, the complete profiles were quite different from Eq. (2.20). In contrast, they were almost constant with height. The authors speculate that heterogeneity of the surface (flat cropland) might have increased the values at the surface. On the other hand, the previously derived values may be inadequate for comparison because ‘the presence of some stratiform clouds in AMTEX may have generated larger-scale fluctuations near the CBL top’. In contrast, during LIFT boundary-layer clouds were absent (Lothon et al., 2006, pp. 529–530).

2.4.3 Spectral examination of atmospheric measurements

The decomposition of turbulent parameters into their frequency components v_i can reveal more about the nature of turbulence. A useful tool is the calculation of the energy spectral density (ESD) function of a time series φ_n because it helps drawing conclusions about the involved eddy sizes. The ESD describes the variance (or energy) distribution of a time series within the frequency range. The ESD is often used to visualize the $-5/3$ rd law of the inertial subrange of the TKE. For a discrete time series φ_n with the length N the ESD is defined as

$$S_\varphi(i) = \frac{2}{\Delta v} \left| \frac{1}{N} \sum_{n=0}^{N-1} \varphi_n e^{-2\pi j i n / N} \right|^2 = \frac{2 \Gamma_\varphi(i) \Gamma_\varphi^*(i)}{\Delta v}, \quad i = 1..N/2, \quad j = \sqrt{-1} \quad (2.22)$$

within the frequency range $v_i = i \Delta v$. $\Gamma_\varphi(i)$ and $\Gamma_\varphi^*(i)$ are the discrete Fourier transform of φ_n and its complex conjugate, respectively. The ESD is normalized by the width of a frequency bin $\Delta v = (\Delta t N)^{-1}$ and the factor of 2 accounts for neglecting the negative frequencies $i = -(N/2..1)$. The zero-frequency component of the spectrum at $i = 0$ is neglected, too, because the time series which are considered here are detrended (see Section 3.4) and thus have a zero mean. For the given definition the ESD is normalized such that

$$\sigma_\varphi^2 = \sum_{i=1}^{N/2} S_\varphi(i) \Delta v, \quad (2.23)$$

i.e., the integrated ESD equals the variance of the time series φ_n . In case of discrete time series, a Fast Fourier Transform (FFT) can be used for the calculation of $\Gamma_\varphi(i)$.

In the same way, a cross-spectrum for two time series φ_n and ψ_n can be defined:

$$\check{S}_{\varphi\psi}(i) = \frac{2 \Gamma_{\varphi}(i) \Gamma_{\psi}^*(i)}{\Delta v}, \quad i = 1..N/2. \quad (2.24)$$

In contrast to the ESD the cross-spectrum is complex:

$$\check{S}_{\varphi\psi}(i) = C_{\varphi\psi}(i) + j Q_{\varphi\psi}(i). \quad (2.25)$$

The real part $C_{\varphi\psi}(i)$ is called the *cospectrum* which accounts for the in-phase components of φ_n and ψ_n . In contrast, the 90°-out-of-phase components are covered by the imaginary part $Q_{\varphi\psi}(i)$ —the *quadrature spectrum*. Following Eq. (2.23) the integrated cospectrum results in the covariance:

$$\sigma_{\varphi\psi}^2 = \sum_{i=1}^{N/2} C_{\varphi\psi}(i) \Delta v = \overline{\varphi'_n \psi'_n}. \quad (2.26)$$

The cospectrum is especially useful when observing turbulent fluxes, i.e. $\overline{w'c'}$. For this special case, it is the spectral decomposition of various frequency contributions to the total turbulent flux. Hence it can be checked whether the turbulent scales that contribute to the turbulent transport are covered by the measurement. Then the cospectrum will reach values close to zero at both frequency ends.

Because a large range of frequencies account for to the turbulent flux, a plot of $v_i C_{\varphi\psi}(i)$ over a logarithmic frequency axis is a reasonable presentation. In this way, the area under the curve is representative for the flux contribution from different frequency ranges.

The dominating eddy sizes will usually result in maximum values of the cospectrum in the lower mixed layer (Kaimal and Finnigan, 1994):

$$v_{\max} \approx (2\pi\Lambda_{w,c})^{-1}. \quad (2.27)$$

However, the cospectra in the major part ($0.1z_i < z < z_i$) of the CBL become increasingly unpredictable with height and do not show a generalized envelope (Kaimal et al., 1976).

3 Method—Aerosol flux measurements with lidar

The aim of this work is the quantification of aerosol vertical exchange by means of turbulent aerosol fluxes. The technique is based on the respective method for water-vapor flux measurements with lidar (Senff et al., 1994; Giez et al., 1999; Wulfmeyer, 1999; Kiemle et al., 2007). However, it was necessary to extend the scheme for the application to the aerosol concentration.

In the first part of this chapter an overview of light scattering in the atmosphere with focus on lidar application is presented. Subsequently, the methods used for the determination of optical aerosol parameters are introduced. Thereafter, an overview of the applied optical-to-microphysical-data inversion scheme is given. In the following, the Doppler lidar principle for accurate and high-resolution wind measurements is explained. Then the method developed for aerosol flux measurements is illustrated, followed by the error analysis for the proposed approach. At the end of this chapter, specific requirements for the vertical aerosol flux measurements are discussed.

3.1 Lidar measurements of aerosol optical properties

3.1.1 Light scattering in the atmosphere

Lidar measurements are generally based on the interaction of transmitted laser light with molecules and particles in the atmosphere. The elastic light scattering by molecules is known as Rayleigh scattering. Here the scatterers are much smaller than the wavelength. The molecular-scattering intensity decreases with wavelength λ with λ^{-4} . Backscattering by air molecules is lower by a factor of 5, 80, and 1050 at the laser wavelengths of 532, 1064, and 2022 nm used in this work, respectively,

compared to backscattering at 355 nm.

Light scattering by particles has often been described as scattering by spheres with a complex refractive index, as introduced by Mie (1908). The Mie theory can be applied as an approximation to non-spherical particles as well, but only if the particle dimensions are not *much* larger than the wavelength of the scattered radiation (Wandinger et al., 2002; Müller et al., 2007b; Böckmann, 2001). In contrast, it is not applicable in the case of desert dust particles or ice crystals. A rigorous description of absorption and scattering of light by small particles is found in Bohren and Huffman (1983) and Mishchenko et al. (2002).

In addition to elastic scattering by particles and molecules, inelastic scattering processes such as Raman scattering occur in the atmosphere (Wandinger, 2005). In the case of aerosol Raman lidar, Raman backscattering by nitrogen molecules is measured. For nitrogen molecules, the vibration-rotation transition results in a wavenumber shift of the light of 2330.7 cm^{-1} .

3.1.2 Lidar principle

Lidar systems utilize time-resolved measurements of backscattered light. A short laser pulse with high energy is transmitted (vertically) into the atmosphere. The laser light is scattered at different heights. The backscattered portion of the light is collected by a receiver and measured temporally resolved with detectors. During the time t the light traveled to the height¹ z and back to the lidar, the respective height of scattering can be calculated with the speed of light c_L :

$$z = \frac{c_L t}{2}. \quad (3.1)$$

The signal strength received from a specific distance depends on the backscatter coefficient β in this region. It is comprised of molecular (β^m) and particle backscattering (β^p). With known temperature and pressure profiles the molecular fraction can be calculated and thus separated from the particulate part at every height range. Additionally, light is attenuated due to scattering and absorption by molecules and particles. The respective extinction coefficients are α , α^m , and α^p for total, molecular, and particle extinction, respectively.

¹We consider a vertically pointing lidar where the height z above ground equals the range from the lidar.

The lidar equations for the elastic backscatter signal P_{λ_0} and the signal P_{λ_R} caused by inelastic backscattering from nitrogen molecules can be written as (Wandinger, 2005):

$$P_{\lambda_0}(z) = P_0 \frac{c_L \tau_L}{2} \frac{A_t}{z^2} \eta_{\lambda_0} O(z) \beta_{\lambda_0}(z) \exp \left[-2 \int_0^z \alpha_{\lambda_0}(z') dz' \right], \quad (3.2)$$

$$P_{\lambda_R}(z) = P_0 \frac{c_L \tau_L}{2} \frac{A_t}{z^2} \eta_{\lambda_R} O(z) N_R(z) \frac{d\sigma(\pi, \lambda_0)}{d\Omega} \exp \left[- \int_0^z [\alpha_{\lambda_0}(z') + \alpha_{\lambda_R}(z')] dz' \right]. \quad (3.3)$$

The symbols used in these equations are:

- $P_\lambda(z)$... received power at the respective wavelength from distance z [W],
- $\beta_{\lambda_0}(z)$... 180°-backscatter coefficient at wavelength λ_0 at distance z [$\text{m}^{-1} \text{sr}^{-1}$],
- $\alpha_\lambda(z)$... extinction coefficient at wavelength λ at distance z [m^{-1}],
- P_0 ... average power of the laser pulse [W],
- τ_L ... laser-pulse length [s],
- c_L ... speed of light [m s^{-1}],
- A_t/z^2 ... solid angle from which the signal is detected, telescope area/ z^2 [sr],
- η_λ ... receiver efficiency at wavelength λ [1],
- $O(z)$... system-specific overlap function [1],
- $\frac{d\sigma(\pi, \lambda_0)}{d\Omega}$... Raman backscattering cross section of nitrogen molecules [$\text{m}^2 \text{sr}^{-1}$],
- $N_R(z)$... number density of nitrogen molecules [m^{-3}].

3.1.3 Determination of particle backscatter and extinction coefficients

Aerosol backscatter and extinction coefficients can be derived from the above lidar equations by different methods (Ansmann and Müller, 2005). The Raman lidar method is known as the most accurate method. However, long averaging times (usually more than 30 min) are required because the intensity of Raman-shifted return signals is about three orders of magnitude smaller than the one of elastic-backscatter signals from the same molecule. An alternative method for the determination of the particle backscatter or extinction coefficients is often referred to as the *Klett method* (Klett, 1981, 1985; Fernald, 1984; Sasano et al., 1985). This method uses only the

elastic-backscatter signals. The major advantage of this latter method is the high temporal resolution. But because of partly unknown input parameters the solution can be very erroneous under certain atmospheric conditions. Following the summary of Ansmann and Müller (2005) for the Klett solution the lidar ratio

$$S_{\lambda_0}^p(z) = \frac{\alpha_{\lambda_0}^p(z)}{\beta_{\lambda_0}^p(z)} \quad (3.4)$$

needs to be assumed and Eq. (3.2) can be solved for $\beta_{\lambda_0}^p$ as follows:

$$\beta_{\lambda_0}^p(z) = \frac{U(z_0, z, \lambda_0)}{V(z_0, \lambda_0) - 2 \int_{z_0}^z S_{\lambda_0}^p(z') U(z_0, z', \lambda) dz'} - \beta_{\lambda_0}^m(z), \quad (3.5)$$

with

$$U(z_0, z, \lambda_0) = \frac{z^2 P_{\lambda_0}(z)}{O(z)} \exp \left\{ -2 \int_{z_0}^z [S_{\lambda_0}^p(z') - S^m] \beta_{\lambda_0}^m(z') dz' \right\} \quad (3.6)$$

and

$$V(z_0, \lambda_0) = \frac{z_0^2 P_{\lambda_0}(z_0)}{O(z_0) [\beta_{\lambda_0}^p(z_0) + \beta_{\lambda_0}^m(z_0)]}. \quad (3.7)$$

$S^m = 8\pi/3$ is the known lidar ratio for molecules. The largest uncertainty in this method is the *a priori* assumption of the unknown particle lidar ratio $S_{\lambda_0}^p(z)$. Since values from about 20–100 sr for aerosol particles were found (Müller et al., 2007a) errors on the order of 100% can easily arise (Ansmann et al., 1992). Additionally, a reference value $\beta_{\lambda_0}^p(z_0)$ at a distance z_0 needs to be assumed for calibration purposes. Usually, it is fixed in height ranges with low aerosol concentration, i.e. $\beta_{\lambda_0}^p(z_0) \ll \beta_{\lambda_0}^m(z_0)$. However, it can also be set at any height if the reference value is known from another measurement. Another major drawback and error source is the influence of the height-dependent overlap between the laser beam and the receiver field of view in the near range. If the respective overlap profile is not well known and not corrected for, the solution of the above equation is only valid for distances outside the overlap regime.

If the weaker Raman-scattered signals are available, the method described by Ansmann et al. (1992) (also referred to as *Raman method*) can be used to derive the particle backscatter and extinction coefficients independently without an assumption

of $S_{\lambda_0}^p(z)$. The extinction coefficient for this case is directly derived from Eq. (3.3):

$$\alpha_{\lambda_0}^p(z) = \frac{\frac{d}{dz} \ln \frac{N_R(z)O(z)}{z^2 P_{\lambda_R}(z)} - \alpha_{\lambda_0}^m(z) - \alpha_{\lambda_R}^m(z)}{1 + \left[\frac{\lambda_0}{\lambda_R} \right]^{\hat{a}(z)}}. \quad (3.8)$$

Additionally, the backscatter coefficient is derived from the ratio of the elastic and inelastic signals at a height z and from a known reference value $\beta_{\lambda_0}^p(z_0)$ at a reference height z_0 :

$$\beta_{\lambda_0}^p(z) = [\beta_{\lambda_0}^p(z_0) + \beta_{\lambda_0}^m(z_0)] \frac{P_{\lambda_0}(z) P_{\lambda_R}(z_0) N_R(z)}{P_{\lambda_R}(z) P_{\lambda_0}(z_0) N_R(z_0)} \frac{\exp \left[- \int_{z_0}^z \alpha_{\lambda_R}(z') dz' \right]}{\exp \left[- \int_{z_0}^z \alpha_{\lambda_0}(z') dz' \right]} - \beta_{\lambda_0}^m(z). \quad (3.9)$$

A fixed spectral dependency of the extinction coefficient on the transmitted and received wavelengths is assumed and described by the Ångström exponent \hat{a} . The value of \hat{a} is about 1.5 ± 0.5 for urban aerosol in central Europe. Deviations of the true Ångström exponent from the assumed one by ± 0.5 lead to errors in the extinction retrieval of $\leq 5\%$ (Ansmann and Müller, 2005). The vertical molecular density profile can be either derived from radiosounding data or from a standard atmosphere.²

At lower distances the determination of the extinction coefficient is limited by the uncertainty of the systematic overlap function. Under certain conditions the overlap function can be determined and thus corrected (Wandinger and Ansmann, 2002). In contrast, the backscatter coefficient can ideally be determined down to the ground because by calculating the signal ratio, which is evaluated for the derivation of the backscatter coefficient, the instrumental overlap function cancels out. However, it needs to be assured that the overlap functions of the two channels are equal.

3.2 Inversion with regularization

Some of the microphysical parameters that are of great interest for the investigation of aerosol impact on climate in general are effective radius, volume and surface-area concentration, complex refractive index, and single-scattering albedo. For the determination of aerosol fluxes the aerosol volume and mass concentrations are of

²U.S. Standard Atmosphere, 1976, U.S. Government Printing Office, Washington, D.C., 1976.

specific interest.

The method of *inversion with regularization* was used within this work to retrieve microphysical parameters from the lidar data. We follow the explanations presented by Ansmann and Müller (2005) and Müller et al. (2001). The main difficulty of the inversion is that the input optical data are related to the microphysical parameters through non-linear integral equations of the first kind (Fredholm equations) which cannot be solved analytically:

$$g_p = \int_{R_{\min}}^{R_{\max}} K_p(R, \check{n}) v(R) dR + \varepsilon_p^{\text{exp}}, \quad \text{with } g_p = (\alpha_i, \beta_i). \quad (3.10)$$

The variables g_p represent the particle extinction α^p and backscatter coefficients β^p at different wavelengths λ_i . It was shown in the past, that three particle backscatter coefficients and two extinction coefficients at different wavelengths are needed at least to derive trustworthy inversion results. Thus a system what is known as a 3+2 *Raman lidar* was used for further investigations. Based on a Nd:YAG laser a 3+2 Raman lidar delivers backscatter coefficients at 355, 532, and 1064 nm and extinction coefficients at 355 and 532 nm.

The kernel functions $K_p(R, \check{n})$ are calculated from the respective dimensionless extinction and backscatter efficiency parameters Q_p per size interval (see Bohren and Huffman, 1983):

$$K_p(R, \check{n}) = \frac{3}{4R} Q_p(R, \check{n}). \quad (3.11)$$

The particle volume concentration $v(R)$ per size interval dR and the complex refractive index \check{n} are the quantities of interest. The integration limits R_{\min} and R_{\max} are given by the radius range in which particles are optically efficient ($R_{\min} \approx 50 - 80$ nm for the minimum measurement wavelength of 355 nm) and particle concentrations are high enough to contribute significantly to the signal ($R < 10 \mu\text{m}$). The error of the measured optical data g_p is $\varepsilon_p^{\text{exp}}$.

The numerical solution of Eq. (3.10) leads to an *ill-posed inverse problem*. The solutions are characterized by a strong sensitivity to uncertainties of the input data and non-uniqueness and incompleteness of the solution space (Hadamard, 1902). Thus specific mathematical methods such as regularization are required.

For the solution of the Fredholm equation system the particle volume concentration is approximated by a linear combination of base functions $B_j(R)$ and respective

weight factors f_j :

$$v(R) = \sum_j f_j B_j(R) + \varepsilon^{\text{math}}(R). \quad (3.12)$$

The use of eight base functions $B_j(R)$ of a triangular shape has lead to good results (Müller et al., 1999; Veselovskii et al., 2002). The mathematical residual error $\varepsilon^{\text{math}}(R)$ is caused by the approximation of $v(R)$ with the base functions.

In general, the exact position of the investigated particle size distribution in the size range used in Eq. (3.12) is not known. Hence inversion windows of variable width and variable position along the investigated size range are used. Within these inversion windows the base functions are distributed such that their nodes have the same distance on a logarithmic radius scale (see Müller et al., 1999, for a detailed explanation). The complex refractive index \check{n} of the aerosol particles is unknown, too. Therefore, the solution process is carried out for a range of wavelength- and size-independent \check{n} from 1.33–1.8 and 0–0.1 for the real and imaginary parts, respectively.

In the first step of solution finding, Eq. (3.10) is solved which delivers the mathematical solution space. Then physical constraints are introduced in order to further limit the solution space, so that a reasonable physical solution space is obtained. This step is called regularization. Constraints such as smooth and non-negative solutions of the derived particle size distribution are considered. Only those solutions which are physically meaningful and fall under the given constraints are selected from the entire solutions space. The mathematical formalism of regularization is presented in Ansmann and Müller (2005).

With the determined weight factors and the corresponding base functions the volume concentration per size interval ΔR can be calculated with Eq. (3.12). It was found that averaging the physical solutions (which can be 100–800 solutions out of 100,000 mathematical solutions) from the regularization is a useful concept, which significantly improves the inversion results (Veselovskii et al., 2002).

Finally, the total aerosol mass concentration M_d is calculated from the total volume concentration V_d by use of the particle density ρ_p :

$$M_d = \rho_p V_d = \rho_p \sum_R v(R) \Delta R. \quad (3.13)$$

3.3 Wind measurements with coherent Doppler lidar

When the scatterer moves along the light path, monochromatic light with a wavelength λ_0 is frequency-shifted by the Doppler effect during a scattering process. This effect is measured with Doppler wind lidars to determine the spatially resolved wind velocity along the laser beam (Henderson et al., 2005; Werner, 2005). The frequency shift $\Delta\nu_D$ of the incident light depends on the relative velocity u of the scatterer to the lidar system. The Doppler effect for the lidar configuration occurs twice because it results from a backscattering process during which the traveling direction of the light is reversed:

$$\Delta\nu_D = -\frac{2u}{\lambda_0}. \quad (3.14)$$

By this definition, positive velocities account for wind away from the lidar.

The respective Doppler shift is extremely small compared to the transmitted laser frequency. Special efforts are needed to detect these small frequency variations. At short wavelengths it is possible to measure the Doppler shift from particle and molecular backscattering processes with *direct-detection* methods. This can be achieved by the use of steep optical-edge filters (e.g., Korb et al., 1992; Gentry et al., 2000) or with interferometers such as the Fizeau interferometer implemented in a recent development for a space application (Durand et al., 2007; Morançais et al., 2004).

The use of longer wavelengths, e.g., 10.6 μm from a CO_2 laser, is of special interest because the Doppler shift is in the low range of radio frequencies (190 kHz per 1 m s^{-1} wind speed) and can be demodulated by optical mixing (e.g., Brewer and Hardesty, 1995; Schwiesow and Spowart, 1996). This technique is also known as *coherent detection* and can reach accuracies of wind measurements of 5–10 cm s^{-1} . The disadvantages are the relatively large CO_2 lasers and nitrogen-cooled detectors.

In the last two decades near-infrared solid-state lasers between 1 and 2 μm wavelength became available. They are much smaller and have better performance and handling characteristics than CO_2 lasers. Additionally, room-temperature photodetectors (Indium-Gallium-Arsenide) can be used for these wavelengths. Doppler lidars in the 1–2- μm wavelength region can be very robust (e.g., Linné et al., 2007; Grund et al., 2001). But compared to short-wavelength systems, a sufficient particle concentration is required in the scattering volume to act as a tracer for the wind velocity.

Figure 3.1 shows the operation principles of a wind lidar system with coherent detection. A continuous-wave laser referred to as the master oscillator (MO) generates the reference frequency ν_0 which is used for the optical mixing as well as for seeding a pulsed laser which is also called the power oscillator (PO). Since exclusive demodulation would not keep the sign of the Doppler shift, an intermediate frequency offset $\Delta\nu_{\text{int}}$ in the radio frequency regime is added before or during the seeding process. Thus the transmitted laser pulse is shifted by $\Delta\nu_{\text{int}}$ against the MO frequency. Then a transceiving optics transmits the laser pulse into the atmosphere where it is scattered by aerosol particles or hydrometeors (cloud droplets, ice crystals, rain, hail, etc.) adding the Doppler shift $\Delta\nu_{\text{D}}$. Afterwards, the backscattered and received signals are optically mixed with the reference frequency ν_0 and thus demodulated down to the radio frequency $\Delta\nu_{\text{int}} + \Delta\nu_{\text{D}}$ which can be digitized and analyzed for the Doppler frequency shifts. This specific coherent detection scheme, where the MO and the PO frequencies differ by $\Delta\nu_{\text{int}}$, is also known as *heterodyne* detection and allows the determination of the direction of the motion, too.

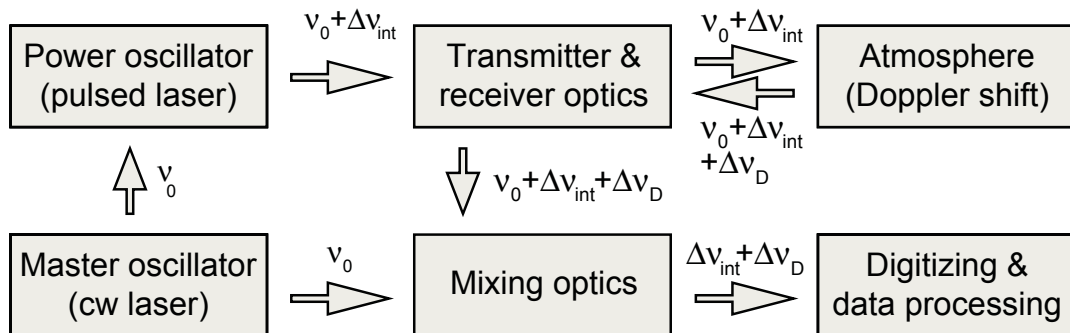


Figure 3.1: Principle of operation of a coherent Doppler wind lidar with heterodyne detection. The frequency indices are 0 for the central radiation frequency, int for the intermediate offset, and D for the Doppler shift induced by scattering from moving particles.

During data processing the signals from different height ranges are individually processed and the contained frequency components are determined. This is usually done either by autocorrelation hardware (Grund et al., 2001; Law and Brewer, 2006) or by a direct digitizing and FFT approach (Linné et al., 1999). Because the intermediate frequency is known, the Doppler shift, corresponding to the line-of-sight wind speed, can be derived.

3.4 Aerosol flux measurements with lidar

In the following it is discussed how the eddy correlation method can be applied to the lidar data. According to Subsection 2.3.2 highly resolved measurements of the vertical wind and of the concentration are combined in order to obtain the turbulent vertical flux. In the case of aerosols, the turbulent transport in terms of particle number, volume, or mass is of interest. Although a lidar measurement of the particle backscatter coefficient and of the vertical wind is almost common practice, a tradeoff is the low temporal resolution when determining the aerosol extinction coefficient. But the latter is very essential for the microphysical characterization of effective radius and volume concentration by inversion.

As a consequence, the method which is illustrated in Fig. 3.2 was developed for profiling of the aerosol mass flux with eddy correlation. In the first step, the required information on the actual lidar ratio $S_{\lambda_0}^p$ is obtained from the Raman lidar observations of $\alpha_{\lambda_0}^p$ and $\beta_{\lambda_0}^p$ taken with a resolution of about 30–60 min, preferably under low background light conditions after sunset. Thus trustworthy information on this input value for the Klett method is available.

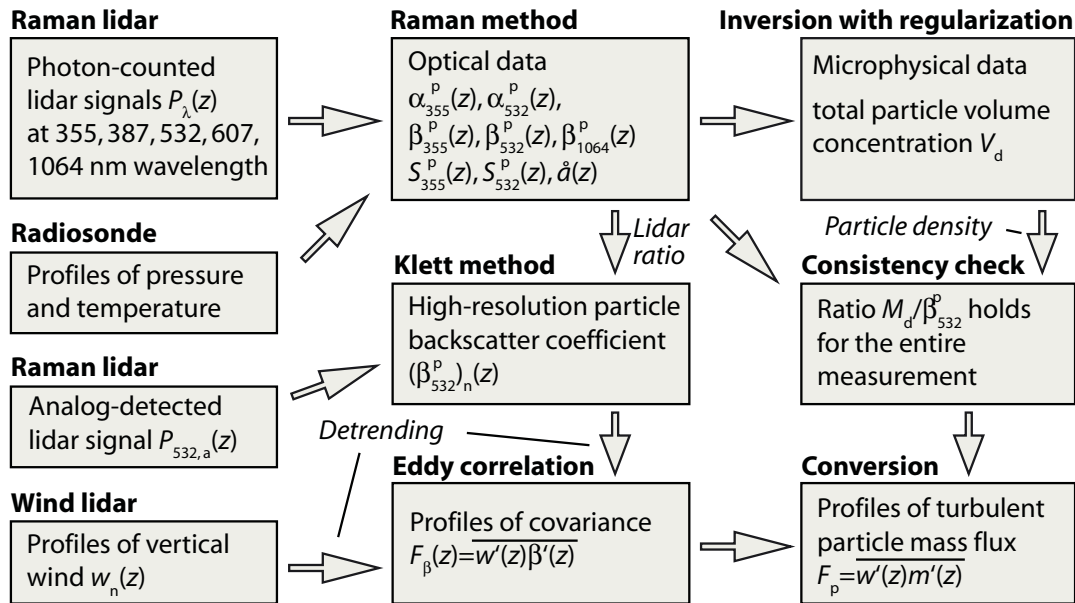


Figure 3.2: Illustration of the method for measurements of the turbulent particle flux with lidar.

Then the N single Klett solutions with index n of the profiles of the backscatter coefficient are calculated as time series $(\beta_{532}^p)_n(z)$ from highly resolved 532-nm

analog detection signals for the entire measurement period. Since the lidar ratio S_{532}^p is known, the profiles of the particle backscatter coefficient can be determined with an accuracy of 5%–10%.

For each analyzed time interval $T = N\Delta t$ and each height level z the time series are detrended and the means are removed by subtraction of the linear function

$$\xi_n(z) = \xi^{\text{trend}}(z)n + \xi^{\text{offset}}(z), \quad \text{with } n = 1 \dots N, \quad (3.15)$$

which was fitted to the respective time series $(\beta_{532}^p)_n(z)$:

$$\beta'_n(z) = (\beta_{532}^p)_n(z) - \xi_n(z). \quad (3.16)$$

This procedure has often been used to remove low-frequency variations which arise from features on the mesoscale that are much larger than the investigated eddies (cf. Kiemle et al., 2007; Giez et al., 1999; Wulfmeyer, 1999). Higher-order filtering of the time series is usually not applicable because of the short length of the time series. In the following, $\beta'_n(z)$ are the time series of the fluctuations of the particle backscatter coefficient at 532 nm (determined with the Klett method) for different height levels.

The vertical wind profiles $w_n(z)$, which are measured with the Doppler lidar, are detrended accordingly and give the time series $w'_n(z)$. Thus the primary output of the calculation of the turbulent flux profile $F_\beta(z)$ after Eq. (2.5) and (2.7) is the covariance

$$F_\beta(z) = \overline{\beta'_n(z)w'_n(z)} \quad (3.17)$$

of fluctuations of vertical wind and particle backscatter.

In a second step, the multiwavelength Raman lidar observation (extinction coefficients at 355 and 532 nm, backscatter coefficients at 355, 532, 1064 nm) are used in order to retrieve microphysical particle parameters with the inversion scheme (see Section 3.2). In this way we obtain—among other quantities—profiles of the particle volume concentration V_d with low temporal resolution, from which the mean particle mass concentration M_d can be estimated by assuming a typical particle density ρ_p .

In a third step, it is assumed that the obtained relationship between β_{532}^p and M_d holds for the entire measurement region (middle and upper PBL), so that any change of β_{532}^p with height and any fluctuations β'_n are caused by respective changes in the

mass concentration M_d and its fluctuations m'_n . I postulate

$$\frac{\beta'_n}{\beta_{532}^p} = \frac{m'_n}{M_d} \quad (3.18)$$

throughout the convective boundary layer and estimate the turbulent aerosol mass flux F_p at a given height to

$$F_p(z) = \overline{m'_n(z)w'_n(z)} = \frac{M_d}{\beta_{532}^p} \overline{\beta'_n(z)w'_n(z)}. \quad (3.19)$$

The basic assumption of this approach is that the conversion factor M_d/β_{532}^p is temporally and vertically constant. This, in turn, is true when the aerosol size distribution and the particle chemical composition do not vary with time and height in the convective PBL. Water uptake by particles must be negligible. This is the case when the relative humidity does not exceed 60% throughout the PBL. The Ångström exponent

$$\mathring{a} = -\frac{\ln(\alpha_{\lambda_1}^p/\alpha_{\lambda_2}^p)}{\ln(\lambda_1/\lambda_2)}, \quad (3.20)$$

with the observation wavelengths $\lambda_1, \lambda_2 = 355, 532$ nm, is a sensitive parameter for the aerosol properties (size distribution, chemical composition). If the Ångström exponent is invariant, it indicates constant aerosol properties and thus a constant M_d/β_{532}^p ratio (O'Neill et al., 2001a,b). The value of \mathring{a} can be derived as a vertical profile from lidar measurements of the extinction coefficient or, as a column-integrated value, from Sun photometer measurements of the aerosol optical depth (AOD)

$$\tau_\lambda = \int_0^\infty \alpha_\lambda^p(z) dz. \quad (3.21)$$

For lidar measurements during daytime it is more practical to use the *backscatter-related* Ångström exponent

$$\mathring{a}^B(z) = -\frac{\ln(\beta_{\lambda_1}^p(z)/\beta_{\lambda_2}^p(z))}{\ln(\lambda_1/\lambda_2)}, \quad (3.22)$$

because profiles of the backscatter coefficient can be obtained with smaller signal-

noise errors. Since the backscatter coefficient is also determined at 1064 nm $\hat{a}^{\beta}(z)$ can be calculated for the wavelengths $\lambda_1, \lambda_2 = 532, 1064$ nm, as well.

The conversion factor M_d/β_{532}^p can also be expressed in terms of the mass extinction efficiency (MEE) (e.g., CCSP, 2009, p. 68). With use of the lidar ratio follows

$$M_d = \frac{S_{\lambda_0}^p}{MEE_{\lambda_0}} \beta_{\lambda_0}^p. \quad (3.23)$$

Several measurements and calculations of MEE have been reported (e.g., Charlson et al., 1968; Jennings and Pinnick, 1980; Dillner et al., 2001). Husar et al. (2000) gives a review of $MEE_{550\text{nm}}$ for dry conditions. Values of 0.7 (0.5–0.8), 3.5 (2.9–4.2), and 4.9 (3.7–6.0) $\text{m}^2 \text{g}^{-1}$ were found on average (range) for dust, smoke, and haze, respectively. However, it should be noted that the MEE is highly diverse. For example, Kinne et al. (2006) compared annual means from 20 different aerosol modules in global modeling. The obtained values of the MEE (AOD/column-integrated aerosol mass) are summarized in Tab. 3.1. Values from 0.5–28 $\text{m}^2 \text{g}^{-1}$ were found, depending on the aerosol type and the specific aerosol module. This large range of values emphasizes the importance of local measurements of the MEE or of the conversion factor M_d/β_{532}^p , respectively.

Table 3.1: Mass extinction efficiency at 550 nm in units of $\text{m}^2 \text{g}^{-1}$ of annual global averages for 20 different aerosol component modules in global modeling (Kinne et al., 2006).

Aerosol type	Median	Range	Standard deviation/mean
Sulfate	8.5	4.2–28.3	56%
Black carbon	8.9	5.3–18.9	36%
Organic matter	5.7	3.2–9.1	26%
Mineral dust	1.0	0.46–2.05	45%
Sea salt	3.0	0.97–7.5	55%

3.5 Error analysis

As discussed in the literature (e.g., Senff et al., 1996; Giez et al., 1999; Linné et al., 2007), ground-based flux measurements with lidar can be very erroneous because a measurement along a laser beam in the atmosphere can never represent the complete

three-dimensional turbulent statistics. Long averaging periods are required to cover at least *most* of the turbulent spectrum. However, the atmosphere needs to be stationary so that averaging is reasonable, which is not always the case.

Another source of uncertainty is the measurement of aerosol properties with lidar. Errors arise from the signal detection method, which is either photon counting or analog detection, from the receiver geometry, and from the data-analysis scheme as already briefly discussed in Section 3.1.

In this section, an overview of the most important error sources is given. It is distinguished between random errors and systematic errors. Errors that are decreased by averaging over an increasing number of independent measurements are random errors. The Gaussian error propagation formula describes the relationship between random and independent uncertainties Δx_i of a variety of parameters x_i that are required to compute y and its random error:

$$\Delta y = \sqrt{\sum_i \left(\Delta x_i \frac{\partial y}{\partial x_i} \right)^2}. \quad (3.24)$$

Calibration uncertainties, wrong assumptions during the data processing, and errors caused by the analysis method itself contribute to the systematic error. For the case of systematic errors the linear error propagation has to be used:

$$\Delta y = \sum_i \left(\Delta x_i \frac{\partial y}{\partial x_i} \right). \quad (3.25)$$

3.5.1 Random errors

3.5.1.1 Sampling error

The error analysis for measurements of higher-order moments and fluxes in turbulent atmospheric systems was originally examined by Lumley and Panofsky (1964). Lenschow et al. (1994) extended the analysis and distinguished between systematic and random errors. They define the random error of the eddy correlation technique (also known as the sampling error) as the stochastic variation between different and uncorrelated representations of the same finite time interval.

Usually, an atmospheric measurement consists of only one representation (a single time series), so the sampling error cannot be calculated as the standard deviation from

a high number of flux results for the same turbulent field. However, if theoretical sampling was performed at many different and independent locations for a given measurement interval with the length T , the relative standard error of all hypothetical flux values results in (see also Giez et al., 1999)

$$\frac{\sigma_{F_{\beta},\text{samp}}(T)}{F_{\beta}(T)} = \left\{ \frac{2\Lambda_{w,\beta}}{T} \left[1 + \frac{\sigma_w^2 \sigma_{\beta}^2}{F_{\beta}^2(T)} \right] \right\}^{1/2} = \left[\frac{2\Lambda_{w,\beta}}{T} (1 + r_{w,\beta}^{-2}) \right]^{1/2}, \quad (3.26)$$

if the series w'_n and β'_n follow a joint Gaussian probability distribution function. Here, σ_w^2 and σ_{β}^2 are the variances of the vertical-wind and particle-backscatter time series, respectively. Hence Eq. (3.26) allows us to calculate the relative sampling error for a given averaging length from measured atmospheric parameters.

3.5.1.2 Random errors of aerosol and wind lidar measurements

Lidar measurements are affected by signal noise. The received photon events are Poisson distributed. The noise contribution to w'_n and β'_n can therefore be assumed to be completely uncorrelated with the adjacent data points $w'_{n\pm 1}$ and $\beta'_{n\pm 1}$. Hence the total variance of a measured turbulent time series can be considered to be the sum of the atmospheric variability and the instrumental random noise:

$$\sigma_{\text{total}}^2 = \sigma_{\text{atmos}}^2 + \sigma_{\text{instr}}^2. \quad (3.27)$$

On the other hand, observations during the sampling interval Δt_n are correlated with observations during adjacent signal sampling intervals $\Delta t_{n\pm 1,2,\dots}$ as a result of turbulence. Therefore, Eq. (3.27) allows us to separate the influence of system noise on the measurement result. Two equivalent methods are generally used in the literature for the deduction of σ_{instr}^2 of a time series φ_n . A third method for the determination of noise in Doppler lidar measurements is described by Frehlich (2001).

1. The auto-covariance function $R_{\varphi\varphi}(l) = \overline{\varphi'_n \varphi'_{n+l}}$ of φ'_n contains the white-noise peak at $l = 0$. Values of $R_{\varphi\varphi}(l)$ for $l > 0$ are extrapolated to $l = 0$. The difference between the extrapolated value at $l = 0$ and $R_{\varphi\varphi}(l = 0) = \sigma_{\varphi,\text{total}}^2$ is then assumed to be the random noise $\sigma_{\varphi,\text{instr}}^2$.
2. We assume that the energy spectral density function of the time series φ_n fol-

lows Kolmogorov's $-5/3$ rd law. If the function drops below the instrumental white-noise floor of the spectrum at high frequencies, the ESD values remain rather constant. Since the integral of the ESD function equals the total variance, the constant noise value times the largest frequency component equals the random error $\sigma_{\varphi,\text{instr}}^2$ (see Fig. 4.3 for an example).

3. Because Doppler lidar measurements are usually averaged over several laser shots N_L for a single wind measurement, Frehlich (2001) suggested to derive the time series of the wind speed w_n from separated measurements of odd and even laser pulses ($N_L/2$ each). The velocity estimate is given by the mean,

$$w_n = 0.5 \left(w_n^{\text{odd}} + w_n^{\text{even}} \right), \quad (3.28)$$

with w_n^{odd} and w_n^{even} having statistically similar random errors. The total instrumental random error for N_L laser shots per derived wind value is given by 0.25 of the variance of the differential time series:

$$\sigma_{w,\text{instr}}^2 = \frac{\sigma_{\Delta w}^2}{4}, \quad (3.29)$$

where the time series $(\Delta w)_n = w_n^{\text{odd}} - w_n^{\text{even}}$ and its variance $\sigma_{\Delta w}^2$ results from an average of $N_L/2$ laser shots.

The contribution of the noise error to a turbulent flux measured by eddy correlation was examined by Giez (1996). For our case, the random error of the flux can be calculated from the noise of the vertical wind and of the backscatter coefficient:

$$\sigma_{F_\beta,\text{instr}} = \left[\frac{\Delta t}{T} \left(\sigma_{w,\text{atmos}}^2 \sigma_{\beta,\text{instr}}^2 + \sigma_{w,\text{instr}}^2 \sigma_{\beta,\text{atmos}}^2 \right) \right]^{1/2}. \quad (3.30)$$

3.5.2 Systematic errors

3.5.2.1 Flux error

The systematic error of a flux measurement ΔF is understood as the deviation of the (theoretical) infinite ensemble average of the flux F_{ens} from any averaged flux $F(T)$

derived from (measured) finite time series of the length T (Lenschow et al., 1994):

$$\frac{\Delta F}{F} = \frac{F_{\text{ens}} - F(T)}{F} \approx 2 \frac{\Lambda_{w,\beta}}{T}, \quad (3.31)$$

where $\Lambda_{w,\beta} \ll T$ is the integral time scale of the flux. Lenschow et al. (1993) discussed difficulties in the experimental determination of the flux integral scale. However, they were able to derive an upper bound for the systematic flux error:

$$\frac{\Delta F}{F} = \frac{F_{\text{ens}} - F(T)}{F} \leq 2 \frac{\sqrt{\sigma_w^2 \sigma_\beta^2}}{F} \frac{\sqrt{\Lambda_w \Lambda_\beta}}{T}, \quad (3.32)$$

with Λ_w , Λ_β , σ_w^2 , and σ_β^2 representing the integral scales and the variances of the vertical wind and the backscatter coefficient, respectively. These values, especially the vertical-wind and backscatter integral scales, can be derived from measurements with a higher certainty than the flux integral scale.

3.5.2.2 Vertical-wind-speed error

Systematic errors in the determination of the vertical wind speed with Doppler lidar can occur in case of a non-vertical alignment of the laser beam, and hence *contamination* from horizontal wind components, especially their fluctuations. In Subsection 4.3.2 a method to check the alignment with sufficient accuracy is presented. As a consequence, the error can be assumed to be less than 5 cm s^{-1} and is therefore negligible.

Additionally, a variable offset, or bias, can be observed in the wind data (on the order of $20\text{--}40 \text{ cm s}^{-1}$). This is mainly caused by an observable frequency chirp in the transmitted laser pulse and its impact on the frequency estimation of the returned lidar signal. In Subsection 4.2.4 a method to determine the chirp is applied. Experience shows that this bias is constant over measurement periods of several hours and is thus removed by the calculation of the fluctuation w'_n . Hence it can be stated that the remaining error ($< 5 \text{ cm s}^{-1}$) is negligible for the determination of vertical fluxes.

3.5.2.3 Errors of optical lidar data

Several parameters need to be assumed for the calculation of the particle backscatter and extinction coefficients (see Subsection 3.1.3). For the Raman method Mattis et al.

(2004, p. 4) found that ‘the relative error of the backscatter coefficient, the extinction coefficient, the lidar ratio, and the Ångström exponent caused by signal noise and atmospheric input parameters are about 5%–10%, 10%–25%, 15%–30%, and 15%–30%, respectively.’ Discussions on error sources and uncertainties in the derived optical properties can be found in Ansmann et al. (1992); Ansmann et al. (2002); Ferrare et al. (1998); Whiteman (2003a,b).

The signal-noise errors are clearly random, whereas the errors caused by wrong assumptions of the input parameters for the Klett method are more difficult to classify. If the true parameters of all profiles fluctuate around given mean values of $S_{\lambda_0}^p$ and $\beta_{\lambda_0}^p(z_0)$, the errors of the single profiles are random. But for the data-processing scheme (see Section 3.4 the lidar ratio and the reference value are derived from a Raman lidar measurement in the evening for the solution of the daytime backscatter coefficient. Thus a bias can arise from mesoscale variations between the two measurements. In this context, the uncertainties are treated as systematic errors.

3.5.2.4 Errors of microphysical properties

Error treatment with the inversion scheme is not fully understood yet and still subject of investigation (Veselovskii et al., 2002). Since averaging the solutions which remain after the regularization is the accepted method at the moment (see Section 3.2), the standard deviation of the single solutions from the mean is presumed to be the error of the inversion result. Müller (2007, p. 42) summarized the errors of his investigations. For the effective radius r_{eff} , the surface-area concentration S_d , and the volume concentration V_d he found errors of the order of 10%–50%, depending on the complexity of the predominant particle size distribution.

Additionally, the particle density ρ_p which is used to determine the particle mass concentration was estimated from empirical values. Depending on the assessment of the particle composition, an error on the order of $\Delta\rho_p/\rho_p \approx 20\%$ can be estimated.

Atmospheric changes between the time period of the flux measurement and the determination of the microphysical properties can occur, too. Although special care is taken to identify these events, it must be kept in mind that wind direction change, modified photochemistry, varying relative humidity, and entrainment can influence the optical-to-microphysical conversion. Under appropriate conditions this error is estimated to be on the order of 25% or less.

3.6 Measurement requirements

In the following the requirements for the experimental setup which follow from the remarks above are summarized.

3.6.1 Length of the time series

The dominating uncertainty in flux measurements was found to be the sampling error (Kiemle et al., 2007; Giez et al., 1999; Senff et al., 1994). As a first guess, let us assume parameters for a common CBL, as it is typically observed in Leipzig. With a CBL height of 1500 m and Eq. (2.21) the flux integral scale is estimated to 190 m in the center of the CBL. With a horizontal wind speed of $5\text{--}8\text{ ms}^{-1}$ $\Lambda_{w,\beta}$ is on the order of 30 s. A typical correlation coefficient between the vertical wind and a scalar variable is on the order of 0.2–0.3 (in case of water vapor, see Stull, 1997, p. 44). Following Eq. (3.26) and using these initial guesses, we obtain the sampling error as:

$$\frac{\sigma_{F,\text{samp}}}{F_\beta} = \frac{(33 \pm 6)}{T^{1/2}} [\text{s}]^{1/2}. \quad (3.33)$$

We see that it is virtually impossible to reduce the sampling error to 10% because of the square root of the length of the measurement interval T in the denominator. It would require averaging times of 30 h under these conditions. The maximum length of the measurements is of the order of 1.5 h in the CBL, because of diurnal variations. Using that length results in a sampling error on the order of 45%.

The systematic error of *incomplete* sampling for flux measurements after Eq. (3.31) and (3.32) for the assumed CBL is about 1%–7%. Therefore, it is negligible compared to the sampling error for measurement periods of one hour or more in the CBL.

3.6.2 Temporal resolution

For local isotropy of turbulence, all correlations between velocity components and any scalars vanish for frequencies of the inertial subrange of turbulence and above (Kaimal and Finnigan, 1994, p. 36). The integral scale marks the transit from the energy-containing part of the turbulent spectrum to the inertial subrange. Consequently, the temporal spacing in the measured time series Δt must be less than $\Lambda_{w,\beta}$ to cover the high-frequency part in the spectrum of turbulent transport. Assuming a

flux integral scale of 30 s on average, a measurement resolution Δt of the order of 10 s or less has to be chosen. However, Δt cannot be decreased arbitrarily because the increased signal noise will result in higher uncertainties of the derived time series. The minimum feasible Δt is restricted by the instrument noise for the determination of the backscatter coefficient with the Klett method. Usually, I used $\Delta t = 5$ s.

3.6.3 Measurement accuracy of the vertical wind and the optical lidar data

For the estimation of the required measurement accuracy let us approximate the variances of the vertical wind and the particle backscatter coefficient by $1.5 \text{ m}^2 \text{ s}^{-2}$ and $0.1 \text{ Mm}^{-2} \text{ sr}^{-2}$, respectively. With the correlation coefficient $r_{w,\beta} = 0.25$ the covariance $R_{w,\beta} = F_\beta = \overline{w'\beta'} \approx 0.1 \text{ Mm}^{-1} \text{ sr}^{-1} \text{ m s}^{-1}$. With $T = 5400$ s, $\Delta t = 5$ s, and a maximum instrumental random error $\sigma_{F,\text{instr}}/F_\beta$ of 5%, we derive from Eq. (3.30):

$$1.5 [\text{m}^2 \text{ s}^{-2}] \sigma_{\beta,\text{instr}}^2 + 0.1 [\text{Mm}^{-2} \text{ sr}^{-2}] \sigma_{w,\text{instr}}^2 < 0.03 [\text{Mm}^{-2} \text{ sr}^{-2} \text{ m}^2 \text{ s}^{-2}]. \quad (3.34)$$

If we balance both terms, the random errors $\sigma_{\beta,\text{instr}}$ and $\sigma_{w,\text{instr}}$ need to be smaller than $0.1 \text{ Mm}^{-1} \text{ sr}^{-1}$ and 0.4 m s^{-1} , respectively.

On the other hand, for the inversion with regularization the measurement accuracy of the three particle backscatter coefficients and the two extinction coefficients need to be on the order of 10%. Especially the determination of the extinction coefficients demand long averaging periods because of the weak Raman signals. Up to now, the data evaluation is a manual task and requires a lot of experience. As a consequence, a singular measurement (about 1 h) for the determination of the microphysical particle properties has to be used.

3.6.4 Displacement of the sensors

The eddy correlation method requires the measurement of both investigated quantities in the same volume. Two different lidar systems are usually separated by several meters. The influence of horizontal sensor displacement on eddy flux measurements was investigated by Lee and Black (1994). Later Kristensen et al. (1997) derived a more ‘practical’ equation for the determination of the *flux losses* due to sensor

displacement. Then they verified their findings by experiments. For an idealized cospectrum at the height z and with the horizontal displacement D they derived:

$$F^D \approx F^0 \left[1 - 3.0B \left(\frac{|D|}{z} \right)^{4/3} \right], \quad (3.35)$$

where F^D is the flux measured with a sensor displacement in contrast to the flux F^0 measured with no displacement. B is a stability parameter. The authors do not specify B , but for a range of $0.2 < B < 1.5$ their experimental findings can be re-evaluated. Using a $|D|/z$ ratio of 0.025 (10 m sensor displacement and a height of 400 m), *flux losses* from 0.5%–3% are found. From this examination we see that the displacement of the lidar systems can be several meters without affecting the flux measurement significantly. However, both lidar beams must be vertically aligned—the wind lidar for exact *vertical* wind measurements and the Raman lidar to measure the particle backscatter coefficient in the *same* volume.

3.6.5 Relative humidity

The method which was proposed in Section 3.4 requires the absence of hygroscopic growth. During the ascent of air in the CBL the temperature usually decreases and thus the relative humidity increases. Therefore, the relative humidity at the top of the CBL should not exceed a certain maximum.

The effect of water vapor on the optical aerosol properties has been studied by different authors (e.g., MacKinnon, 1969; Hänel, 1976; Wulfmeyer and Feingold, 2000). A diversity of results arises mainly from different aerosol types (ammonium sulfate, dust, sea salt, and various mixtures). With water uptake the mixing state, and thus the complex refractive index, the morphology, the chemistry, and the surface tension of the aerosol can vary significantly.

Hänel (1976) studied the humidity dependence of the particle extinction coefficient of six different aerosol types (given on p. 114) in detail. For the aerosol particles measured at 1000 m height above sea level on top of Hohenpeißenberg, Germany, 1970, he found (Table XIII) a ratio of $\alpha_{70\%r.h.}^p / \alpha_{dry}^p = 1.10$ at 550 nm wavelength. For urban aerosol at Mainz, Germany, 1970, the same increase of the extinction coefficient of 10% was reached for 60% r.h. already.

More recently, Wulfmeyer and Feingold (2000) investigated the increase of the backscatter coefficient due to hygroscopic particle growth from measurements with DIAL below boundary-layer cumulus clouds. They found significant increases of β^P only above 75% r.h. at a wavelength of 720 nm. In comparison with model calculations the authors suggest that they primarily observed a mixture of ammonium sulfate and dust.

Let the allowable systematic error of the backscatter coefficient because of hygroscopic growth be about 10%. It can be concluded from the above findings that the r.h. must not exceed 60%–70% within the measurement regime. Radiosoundings are used to find whether the entire CBL is dry enough. If this is not the case, the measurements have to be limited to altitudes with the appropriate humidity.

4 Instrumentation—Two co-located lidars

The Raman and the Doppler lidar systems, which were used for the aerosol flux measurements, are introduced in this chapter. The aerosol Raman lidar MARTHA (Multiwavelength Atmospheric Raman lidar for Temperature, Humidity, and Aerosol profiling) of the IfT is one of the most powerful lidars of EARLINET (Mattis et al., 2004; Mattis et al., 2008). It is described in Section 4.1. An analog detection channel at 532 nm was required and implemented within this work. This extra channel allows the determination of the backscatter coefficient with a temporal resolution of 5 s which is needed for turbulent-flux measurements.

The coherent Doppler wind lidar (WiLi) has been designed in the scope of a PhD work at IfT (Žeromskis et al., 2004). Further developments were needed for aerosol flux measurements. The apparatus and the improvements are presented in Section 4.2.

The final part of this chapter deals with the experimental setup of both systems for eddy-correlation measurements. This application requires a synchronous dataset of two variables that are measured within the same volume and at the same time grid.

4.1 Aerosol Raman lidar MARTHA

4.1.1 System summary

The aerosol properties used in this work, i.e., the highly temporally resolved profiles of the backscatter coefficients and the multiwavelength optical aerosol information, were measured with the IfT's three-wavelength Raman lidar MARTHA. The Raman lidar contains a Nd:YAG laser which emits radiation at 355, 532, and 1064 nm. Besides the three elastic-backscatter signals (at 532 nm additionally with polarization discrimination), vibration-rotation Raman signals of nitrogen at 387 and 607 nm and

of water vapor at 408 nm and two rotational Raman signals at 532 nm are observed. From these nine return signals, profiles of particle backscatter coefficients at 355, 532, and 1064 nm, of particle extinction coefficients at 355 and 532 nm, of the particle depolarization ratio, of the water-vapor mixing ratio, and of the temperature are determined. Details of the Raman lidar setup can be found in Mattis et al. (2002); Ansmann and Müller (2005). In recent years, several measurement capabilities have been added to the system. Especially useful for the studies of the PBL is a 0.1-m near-range telescope, which is used alternately to the 1-m far-range telescope for observations between 0.1 and 1.5 km height. With the large telescope, the measurement range starts at about 800 m. Figure 4.1 and Table 4.1 summarize the system setup and the parameters.

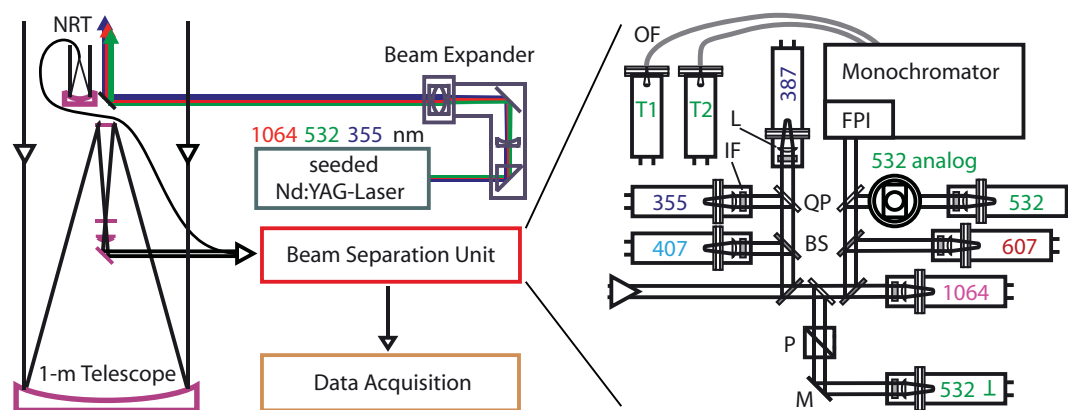


Figure 4.1: Raman lidar setup. Left: schematic representation of the components. Right: enlargement of the beam-separation unit with all receiver channels. The 532-nm analog channel points vertically off the optical table. BS - beam splitter, FPI - Fabry-Pérot interferometer, IF - interference filter, L - lens, M - mirror, NRT - near-range telescope, OF - optical fiber, P - polarizing BS, QP - quartz plate.

4.1.2 Implementation of the analog channel

The signals of the Raman lidar MARTHA were exclusively detected with PMTs (photomultiplier tubes) which are operated in single-photon-counting mode. It has been shown in the past that photon-counting is the best choice for lidar signal detection due to its linear behavior over up to six orders of magnitude of signal dynamics after an adequate time of integration. However, a major disadvantage for turbulent aerosol

Table 4.1: Fundamental system parameters of the Raman lidar MARTHA. Details of the system can be found in Mattis (2002). FR - far range, NR - near range.

Transmitter	
Laser	Quanta Ray GCR 290-30 Hz
Wavelengths (energy)	1064 nm (500 mJ), 532 nm (400 mJ), 355 nm (200 mJ)
Beam expansion	to 15 cm with an achromatic refractive telescope
Beam divergence	0.1 mrad
Receiver	
Telescopes	1-m Cassegrain (FR), effective focal length = 10 m 10-cm parabolic mirror with fiber at focal point (NR), focal length = 0.3 m
Field of view	0.4 mrad (FR), 3.3 mrad (NR)
Detection channels	355, 387, 408, 607, and 1064 nm: total 532 nm: total, cross-polarized, 2 × rotational, analog
Data acquisition	
9 × photon counting	height resolution 15–60 m
1 × analog	height resolution 7.5 m

flux measurements is the low temporal resolution. At the cost of the linearity an analog detection channel at 532 nm has been added, which is operated in parallel to the nine photon-counting detection channels and provides aerosol backscatter data with higher spatial and temporal resolution. Special care is needed when evaluating data from this channel. The main problem was the background correction of the signal because the dynamic range of the data acquisition does not cover the background and the signal maximum adequately. Additionally, oscillations in the data acquisition line that drop the signal below the background in the far-range bins could be observed. For these reasons data-product comparison with the photon-counting channels are needed.

Since in the 532-nm photon-counting channel of MARTHA neutral-density (ND) filters with an optical depth (OD) of 4 were utilized for signal reduction to the single-photon regime, most of the collected light could be used for the implementation of an analog channel. Thus the major portion of light is reflected out of the path with a beamsplitter (reflecting ND filter of OD = 2). As in the 532-nm photon-counting channel an interference filter at 532.075 nm with a bandwidth of 1.0 nm (Barr Associates) is used for out-of-band background suppression in the analog channel. A planoconvex lens with 100 mm focal length is used to focus the light onto a PMT

module (Hamamatsu H6780-01). The current generated by this PMT module is fed into a transimpedance amplifier (HCA-20M-100K-C, FEMTO Messtechnik GmbH, Berlin) which converts the signal by 10^5 V A^{-1} with a 3-dB bandwidth of 20 MHz.

Data acquisition is done with a 12-bit analog-to-digital conversion card (NuDAQ, PCI-9812, ADLINK Technology Inc.). The card performs $20 \text{ MSamples s}^{-1}$ which results in a height resolution of 7.5 m. An acquisition software has been developed within this work in order to accumulate the analog lidar return transients from several laser shots. The time resolution of the data acquisition was set to 5 s (see Section 3.6). A major attribute of this software is the possibility of temporal synchronization with other instruments. This requirement was realized by a main time loop which has been implemented within the software. It interrupts the accumulation routine on a 5-s time grid fixed to the system clock, e.g., at :00 s, :05 s, :10 s, etc. For easy post-processing purposes the acquired dataset is directly written into a NetCDF file (Rew and Davis, 1990).

4.1.3 Error determination from an example measurement

Data from a measurement with the analog channel and the near-range telescope are shown in Fig. 4.2 and are compared to the results of the respective photon-counting channel at 532 nm. The measurement was taken on 12 September 2006, 1930–2000 UTC. The data of the analog channel (7.5 m height resolution) were linearly interpolated to the heights of the data points of the photon-counting channel, which had a height resolution of 15 m. The background-corrected signal from the analog channel was scaled to the photon-counting signal at around 2 km height. Both signals agree remarkably well for this case even in the background region at 13–15 km height. The deviation of the two signals is shown as $(\text{signal}_{\text{pc}} - \text{signal}_{\text{analog}})/\text{signal}_{\text{pc}}$ in the center of Fig. 4.2. The deviation remains on average within $\pm 5\%$. However, this small difference affects the Klett solution of the backscatter coefficient, which was derived with the assumption of a constant aerosol lidar ratio of 70 sr. For comparison the Raman solution from the photon-counting signal is also shown. The profile derived from the analog signal tends to be skewed around the vertical resulting in too small values within the PBL. However, the systematic error of the backscatter coefficient for these cases is estimated to be about 5%.

The noise error can be determined from the measured data itself. Figure 4.3 shows

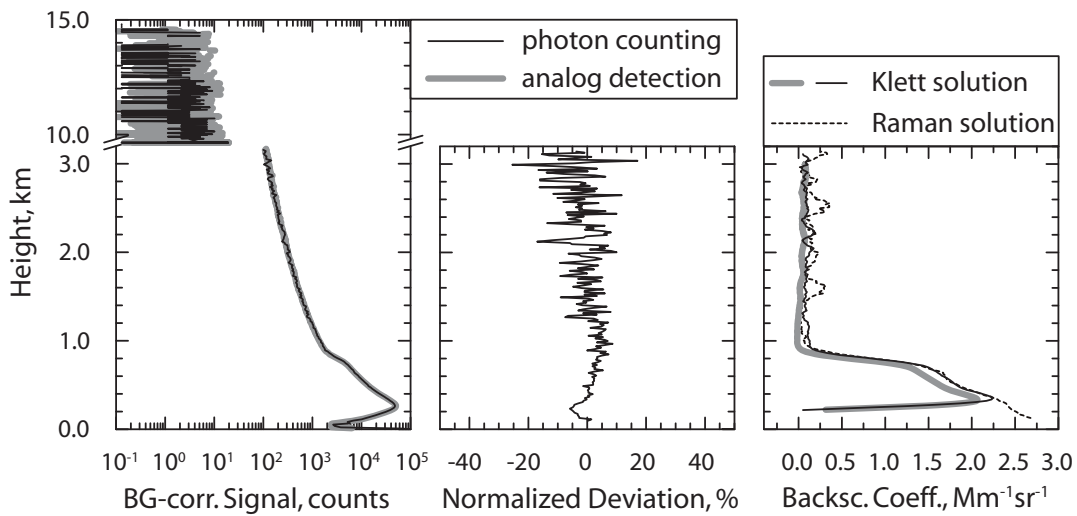


Figure 4.2: Comparison of the analog with the photon-counting channel at 532 nm. The measurement was taken with the near-range telescope on 12 September 2006, 1930–2000 UTC. Left: averaged background-corrected signals. Middle: normalized deviation of both signals. Right: corresponding backscatter coefficient at 532 nm.

a time series of the backscatter coefficient (Klett method) measured with the 532-nm analog channel. The fluctuations between clean free-tropospheric air and polluted boundary-layer air range from 0.2 to $2.3 \text{ Mm}^{-1}\text{sr}^{-1}$. Additionally, the variance spectrum was calculated from the time series. It shows the $\nu^{-5/3}$ slope that is expected from the turbulence theory. At high frequencies the instrumental noise becomes visible as a constant noise level. Since the total area of ESD is normalized to the variance of the time series itself the area under the noise level equals the random error variance. From this figure we see that the expected random error of the backscatter coefficient time series is of the order of $\sigma_{\text{instr},\beta} = 0.12 \text{ Mm}^{-1}\text{sr}^{-1}$.

4.2 Doppler lidar WiLi

The current system setup of IfT’s coherent Doppler wind lidar (WiLi) is discussed in the following. Early system developments of the lasers, the transceiving optics, and the data processing scheme were part of a previous PhD work and two diploma theses (Žeromskis, 2009; Engelmann, 2003; Rhone, 2004).

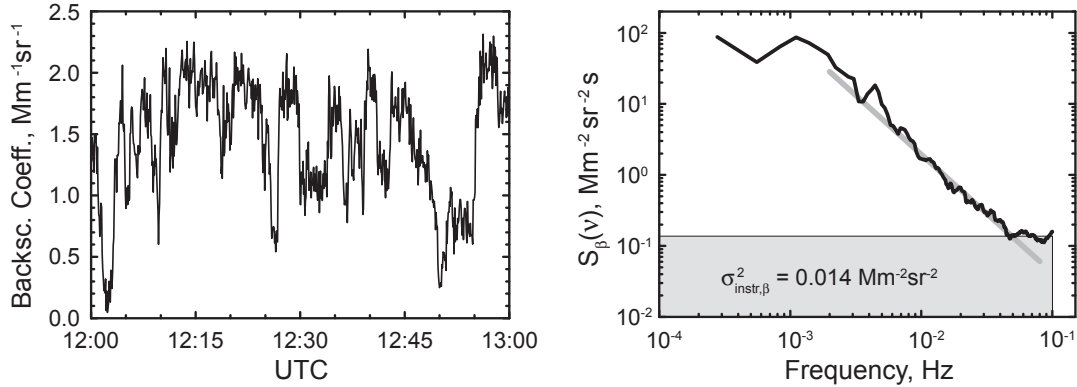


Figure 4.3: Random error determination for the measurements of the backscatter coefficient. Left: time series of β from 13 September 2006 at 900 m height. Right: the normalized ESD shows the expected $-5/3$ rd slope and the transition to constant values at high frequencies. The shaded area is the noise floor variance.

At the beginning of this work the system was set up in a 20-foot sea container equipped with an air condition that keeps the temperature stable to ± 1 K. In this way, easy operation during several measurement campaigns could be achieved (SAMUM-2, COPS, AVEC, LAUNCH-2005¹). Additionally, a full-hemispherical scanner (developed at the National Center for Atmospheric Research, Boulder, USA) with a free aperture of 160 mm was mounted on the container roof and is used for three-dimensional wind measurements. In this beam-steering unit (BSU) two mirrors are used to turn the beam around the azimuth and the elevation axis, respectively. Conical scans allow the determination of the horizontal wind speed using the Vertical Azimuth Display (VAD) technique (Henderson et al., 2005).

In the first part of this section the current optical setup is described. Then it is shown, how the characteristics of the laser pulse from the power oscillator have been determined. Furthermore, a redesign of the data acquisition software was necessary in order to perform wind and aerosol flux measurements. Thus the design of the newly developed software is illustrated. This is followed by explanations of the data post-processing procedure and eventually the wind-speed determination.

¹International Lindenberg campaign for assessment of humidity and cloud profiling systems and its impact on high-resolution modeling, Germany, August–October, 2005



Figure 4.4: Coherent Doppler lidar system deployed in the SAMUM-2 experiment at Praia Airport, Cap Verde. Top: container with its beam-steering unit on top (photograph by J. Fruntke, 2008). Bottom: setup of the optical benches inside.

4.2.1 Optical system setup

The optical setup of the coherent Doppler wind lidar is shown in Fig. 4.5 (Žeromskis et al., 2003, 2004; Engelmann et al., 2008). It is realized on two optical tables which are put on top of each other within one mechanical frame (see Fig. 4.4, bottom). The laser system is assembled on the lower level. It consists of a continuous-wave (cw) laser referred to as the master oscillator (MO) and a pulsed laser also called the power oscillator (PO). The transceiving and mixing optics are arranged on the upper level.

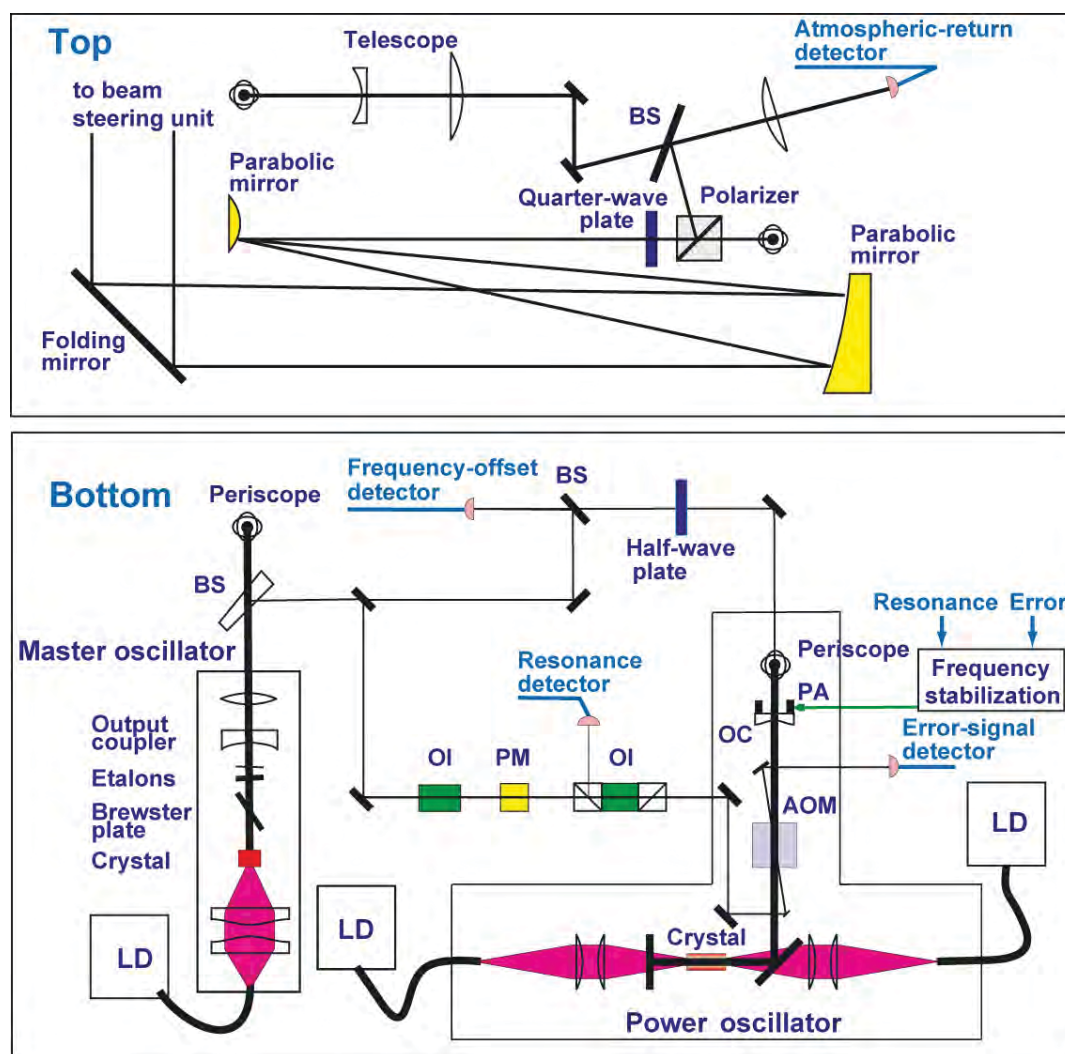


Figure 4.5: Optical setup of the 2- μm coherent Doppler wind lidar. AOM - acousto-optical modulator; BS - beam splitter; LD - laser diode; OC - output coupler; OI - optical isolator; PA - piezo actuator; PM - phase modulator.

The master oscillator is a cw single-frequency near-hemispherical laser. The active medium is a LuAG (lutetium aluminum garnet) crystal of 3 mm length doped with 3% Thulium. One end of the crystal has a high-reflection coating for 2022 nm and serves as a resonator mirror, the other end is anti-reflection coated. The crystal is pumped from one end with 785-nm radiation of a fiber-coupled cw laser diode. This pump diode delivers a maximum power of 2.5 W. Single-mode operation is achieved by the use of two etalons, an uncoated one of 90 μm thickness and a coated one of 250 μm thickness with a reflectivity of 30%. By tilting the etalons, laser operation at 2021.8 or 2022.55 nm is possible. These wavelengths correspond to minima of the atmospheric absorption spectrum in the spectral range of laser operation. The Brewster plate in the MO maintains linearly polarized laser emission. With an output coupling mirror of 99% reflectivity and a curvature radius of 10 cm a laser power of 25 mW in single-mode operation is achieved. The master oscillator is thermally isolated, and the temperature within the housing is stabilized to less than 0.1 K. A single-longitudinal mode drift of about 300 MHz per hour was observed during long-term measurements with a scanning Fabry-Pérot interferometer.

A lens behind the master oscillator is used to collimate the laser beam to a divergence of about 0.7 mrad. The output radiation of the master oscillator is divided into two pathways, one for injection seeding of the power oscillator and the other one for the heterodyne detection unit. Back reflection from the power oscillator to the master oscillator is prevented by the use of two optical isolators within the injection-seeding path.

For the power oscillator a design similar to the High Resolution Doppler Lidar (HRDL) system (Grund et al., 2001; Wulfmeyer et al., 2000) was chosen. The active medium is again a LuAG crystal doped with 3% Tm. The crystal length is 12 mm. The laser is L-shaped to allow longitudinal pumping of the crystal from both sides with two cw fiber-coupled laser diodes. Each diode delivers a maximum output power of 30 W. Two quarter-wave plates near the crystal are inserted to prevent spatial hole burning. Q-switched pulse operation is obtained with an 80-MHz acousto-optical modulator, which is also used for injection seeding with the MO radiation and frequency-offset generation. Usually, the laser runs with a pulse repetition frequency (PRF) of 750 Hz at which a pulse energy of 1.5 mJ is achieved. Longitudinal cavity adjustment and stabilization is based on the Pound-Drever-Hall method (Wulfmeyer et al., 2000). A piezo actuator (PA) at the cavity end mirror, a phase mod-

ulator, which modulates ± 40 MHz side lobe frequencies on the seeding laser beam, and two detectors are therefore required. An electronic circuit, which was originally developed for HRDL, scans the cavity length by the use of the PA until a peak is observed at the resonance detector. An error signal, which has a zero-crossing point at the resonance length of the cavity, is generated with the help of the error-signal detector and a demodulation circuit. After finding the resonance the electronics uses the error signal for exact frequency stabilization of the power oscillator to the master oscillator before each laser pulse. In general, a total frequency stabilization to about ± 1 MHz has been achieved.

In the transceiving optics a Glan-Taylor polarizer and a quarter-wave plate are inserted in order to use an off-axis Mersenne telescope, an afocal system of two parabolic mirrors, for expanding and transmitting the laser beam as well as for receiving the atmospheric backscattered radiation. The received signal is directed to a wavelength-extended 75- μm InGaAs detector (Sensors Unlimited Inc.) and optically heterodyned with the reference radiation from the master oscillator (Engelmann, 2003). A low-noise 200-MHz transimpedance amplifier (HCA-200M-20K-C, FEMTO Messtechnik GmbH, Berlin) behind the photodetector is used to convert the current which is generated in the detector by 20 kV A^{-1} . The amplified signal and a frequency-offset monitor signal are connected to a high-frequency switch to toggle both signals. In this way, the monitor signal is switched into the signal line during laser pulsing and both signals can be measured with one data acquisition system.

4.2.2 Laser pulse characterization

The laser pulse does not always oscillate at the exact intermediate frequency $\nu_0 + \Delta\nu_{\text{int}}$ given by the injection seeding. Vibrations and also the Pound-Drever-Hall frequency stabilization itself always affect the laser cavity. Therefore, it is necessary to have a continuous frequency calibration in the Doppler spectra. The monitor signal in the signal-detection chain allows a pulse-to-pulse characterization of the laser frequency and thus frequency correction for the spectra of the acquired atmospheric signals. Figure 4.6 shows an example of a single heterodyne monitor pulse at the frequency-offset detector (see Fig. 4.5). As suggested by Frehlich et al. (1994) a model $M(t)$ can be used to describe the beating signal from the transmitted laser pulse. Linné et al. (1999, personal communication) added several more parameters

for a better fitting behavior:

$$M(t) = A_0 \exp \left[-\frac{(t-t_0)^2}{2[\tau_L + A_{\text{asym}}(t-t_0)]^2} \right] \cos [2\pi\Delta v_{\text{int}}t + \pi A_{\text{chirp}}(t-t_0)^2 + \phi] \\ + A_{\text{dd}} \exp \left[-\frac{(t-t_0)^2}{[\tau_L + A_{\text{asym}}(t-t_0)]^2} \right] + A_{\text{trend}}(t-t_0) + A_{\text{offset}}, \quad (4.1)$$

where A_0 , t_0 , τ_L , and ϕ are the amplitude, the time origin at the pulse maximum, the pulse width, and the phase of the pulse, respectively. A_{asym} and A_{chirp} are parameters to describe the asymmetry and the chirp (frequency drift within a single pulse) of the Q-switched laser output, respectively. Additional parameters which originate from the electronic behavior of the low-pass filter after the detector and the transimpedance amplifier are described by A_{dd} , A_{trend} , and A_{offset} . These values correspond to an unfiltered direct-detection portion of the signal, a linear trend, and a constant offset level, respectively.

About 500 acquired monitor-pulse laser signals were fitted to the model. The derived key parameters of Δv_{int} , τ_L , and A_{chirp} are given in Tab. 4.2, supplementing the main system parameters of the Doppler wind lidar. The results show a frequency stability of the pulse laser of nearly 1 MHz. The pulse length τ_L results to 450 ± 30 ns, which is half the width at 60% per definition from the model. The asymmetry parameter was found to be 0.16 ± 0.04 . The chirp of the laser is 950 ± 60 kHz μs^{-1} . Thus it must keep in mind that backscattering from the tail of the laser pulse can falsify the retrieved wind data, especially in regions with a strong gradient in the backscatter coefficient, e.g., at cloud bases (e.g., Grund et al., 2001).

4.2.3 Data acquisition software

Data acquisition is performed with an 8-bit digitizer PC card (PDA1000, FAST ComTec GmbH) the sampling rate of which is set to 250 MSamples s^{-1} . A real-time processing software is used to accumulate data from several laser shots to increase the signal-to-noise ratio (SNR). Because of incoherent scattering from atmospheric aerosol the heterodyne beating signals are phase independent and thus cannot be accumulated directly. The idea of single-shot data acquisition was neglected because of the tremendous amount of generated data. Assuming a pulse repetition frequency of 750 Hz and a maximum height range of 15 km, approximately 20 MB of raw

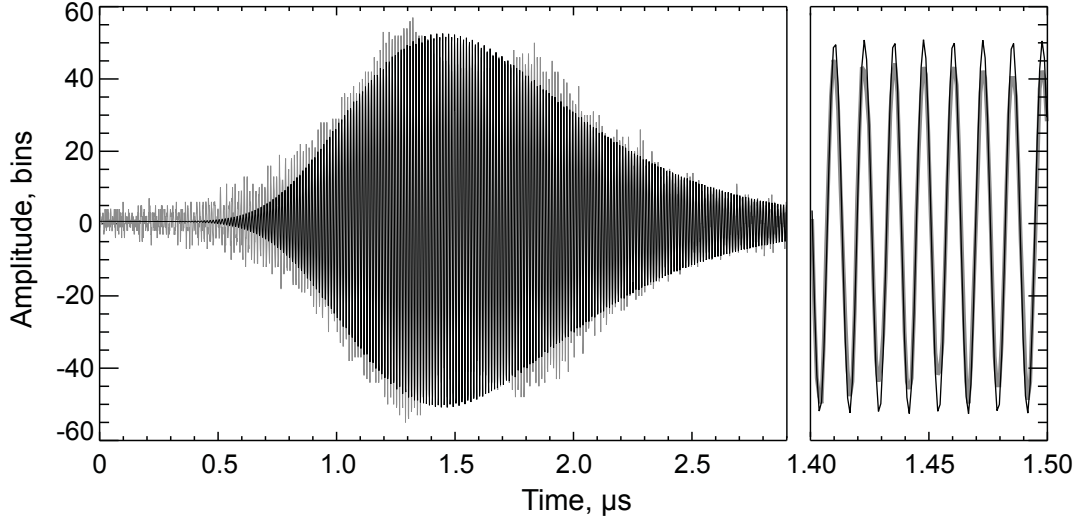


Figure 4.6: Beating signal of the laser monitor pulse (light) and the fit result (dark) from the model Eq. (4.1). Left: complete pulse shape. Right: enlargement of 0.1 μs time scale.

Table 4.2: Specifications of the components of the Doppler wind lidar

Master Oscillator		Transceiver	
Laser crystal	Tm:LuAG	Type	off-axis Mersenne
Design	near-hemispherical	Free aperture	140 mm
Wavelength	2022.5 nm	Photodetector	InGaAs PIN diode
Power	25 mW		75 μm diameter
Power Oscillator		Data Acquisition	
Laser crystal	Tm:LuAG	Preamplifier	20 kV A^{-1} , 200 MHz
Design	L-shaped	Digitizer	8 bit, 250 MSamples s^{-1}
Pulse energy	1.5 mJ		PCI card
PRF	750 Hz	Computer	dual 2.8-GHz CPU
Frequency offset	80 MHz	Data processing	up to 15 km with
Frequency stability	± 1 MHz		1 kHz PRF and
Pulse duration	450 ns		75 m resolution
Chirp	0.95 MHz μs^{-1}		

data would be generated per second. Observations over 24 hours would be almost impossible on this basis. An approach to overcome this problem is the immediate calculation of the power spectra with FFT (Holger Linné, personal communication). This eliminates the phase information from the beating signal and allows direct spectrum averaging. The calculations have to be done separately for every height range to maintain the height resolution in the averaged data. Because of the related high computational costs a fast hardware and a special software design are required.

A double 2.8-GHz processor computer (Intel XEON[®]) which supports the Hyper-Threading technology was selected for this task.² In this configuration the computer virtually uses four Central Processing Units (CPUs). Based on the first software implementations for Windows[®]XP from Rhone (2004) and with helpful suggestions from Linné and Bösenberg (1998) the design was further improved.

A simplified design of the new software sequence is sketched in Fig. 4.7. The main *control loop* starts the data-acquisition (*DAQ*) *thread* and four *FFT threads* that run on the different CPUs. In this way, the computationally intensive FFT calculations from the data of the last laser shot can be performed at the same time as the data acquisition of the current laser shot. A *time-loop-master* thread is used to interrupt the control loop on a fixed time grid whenever one accumulation cycle is over.

The DAQ thread starts a DMA (Direct Memory Access) buffered digitizing sequence which acquires the data directly and without CPU usage to a DMA buffer. Afterwards, the frequency from the laser monitor pulse is determined by a single FFT and the thread is flagged as finished.

The four FFT threads are used to calculate the power spectra from the previous data. Therefore, chunks of 250 points corresponding to 1 μ s are selected. After applying a Blackman–Harris (–74 dB) window used for side-lobe and leakage minimization (Harris, 1978; Nuttall, 1981) and zero padding of six points, a 256-point FFT is performed. FFTW (Frigo and Johnson, 2005) was the library of choice here because it is one of the most efficient libraries available that were designed for calculations on various machines. Thus easy computer replacement is possible in case of a hardware failure. In the following, the resulting power spectra of the acquired data are accumulated with respect to the previously calculated monitor frequency offset. This process is repeated for all height intervals which are approximately 200 interleaved

²This computer was recently replaced by a server computer including a single quad-core Intel XEON[®] processor and a RAID hard-drive solution.

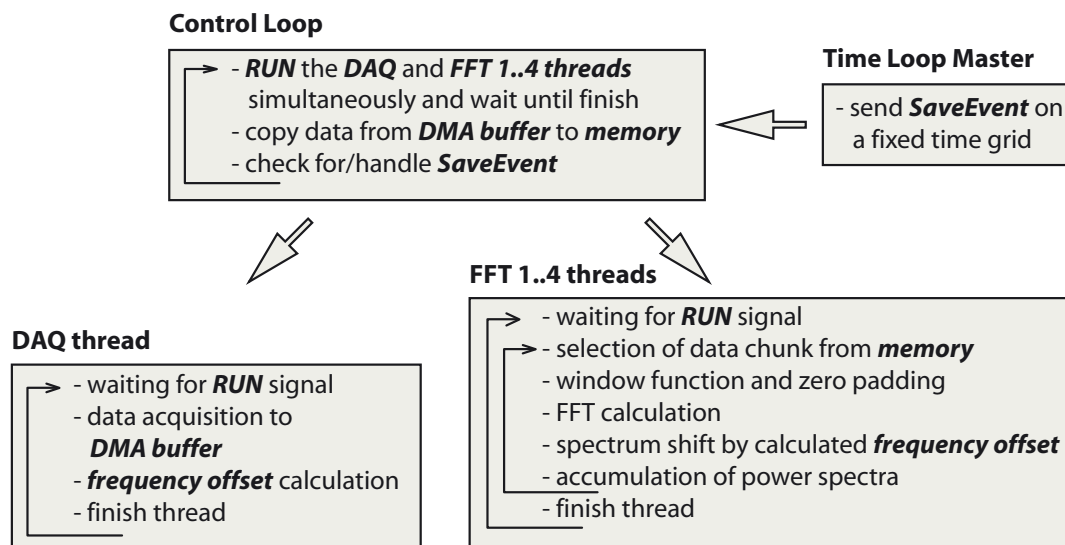


Figure 4.7: Data accumulation scheme of wind lidar acquisition software.

(half-overlapping) bins. Neglecting strong gradients in the backscatter coefficient the spatial resolution is 75 m. This results from the window function that suppresses the signals from the outer range of the particular bin.

After returning from the five started threads, the main control loop copies the acquired and DMA-buffered data to a second data field in the memory for the next calculation loop. If a *SaveEvent* occurs after a certain accumulation time, the power spectra are saved to a NetCDF file. This efficient software design allows laser repetition rates of up to 1000 Hz, while calculating and accumulating about 200 height bins of power spectra per laser shot.

4.2.4 Peak finding and wind determination

It was found that 5-s temporal averaging, which corresponds to about 3500 laser shots, is sufficient to obtain well analyzable spectra for data collection within the PBL and mid-level clouds. The data acquisition software saves power spectra which contain 128 points and represent the frequency range up to 125 MHz, i.e., the frequency bins are spaced by about 1 MHz. With Eq. (3.14) and the laser wavelength of $2\ \mu\text{m}$ the spacing of the frequency bins corresponds to a wind speed of $1\ \text{m s}^{-1}$.

The peak estimation in the spectra and hence line-of-sight wind speed determina-

tion is performed after the respective measurement by a center-of-gravity approach (H. Linné 2005, personal communication; Rhone 2004). First of all, the background of the spectra is removed by subtracting a spectrum measured at large heights where the lidar signal is not affected by atmospheric backscattering. The subsequent peak-finding procedure is illustrated in Fig. 4.8. Starting from the maximum bin $S_0(v_0)$ of the original spectrum $S(v_i)$, the center of gravity v_{cog} is calculated by

$$v_{\text{cog}} = \frac{\sum_{i=-4}^4 v_i S(v_i)}{\sum_{i=-4}^4 S(v_i)}. \quad (4.2)$$

The value v_{cog} is not necessarily the natural center of gravity of $S(v_i)$, especially if the spectrum is not centered to the discontinuous frequency bins v_i . For this reason, a linear interpolation $S'(v'_i)$ of the original spectrum to new values v'_i that are centered around v_{cog} is performed. A repeated calculation of the center of gravity

$$v'_{\text{cog}} = \frac{\sum_{i=-3}^3 v'_i S'(v'_i)}{\sum_{i=-3}^3 S'(v'_i)} \quad (4.3)$$

results in a more precise estimation of the spectral peak at v'_{cog} . Simulations have shown an improvement of 10%–25% compared to the peak estimation v_{cog} [Eq. (4.2)] for spectra with realistic SNR. For such spectral peaks the accuracy (one standard deviation) of the derived frequency is about 60–80 kHz, which results in 6–8 cm s^{-1} wind-speed resolution, respectively. An additional iterative cycle is possible, but it was found that it does not increase the precision in a meaningful manner.

4.3 Experimental setup

4.3.1 Synchronization and coherence of the datasets

For the measurements, WiLi was set up next to the stationary three-wavelength Raman lidar MARTHA at the IfT site in Leipzig. The horizontal distance between the two lidar beams was about 8 m. Hence the bias in the flux measurements introduced

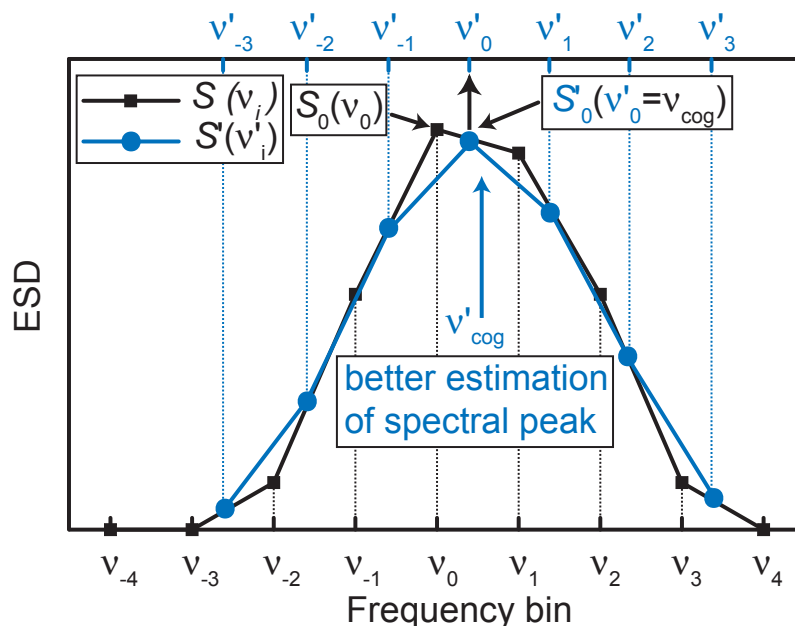


Figure 4.8: Peak estimation from the Doppler lidar spectra $S(v_i)$ by center-of-gravity (cog) calculation. Because of the discontinuous frequency bins in the power spectrum an iterative calculation is applied. The original spectral series is interpolated to a new series $S'(v'_i)$ which is centered at v_{cog} , the center of gravity from $S(v_i)$. The index 0 corresponds to the maximum of the respective series.

by this lateral displacement is negligible for observations in the middle and upper PBL (see Subsection 3.6.4).

Temporal synchronization of both sensors is a major concern for eddy-correlation measurements. Thus the data-acquisition computers of the two systems were synchronized every 15 min via an internet-based time-server software (Dimension 4 v5.0³). Data were stored on a fixed time grid every 5 s. The vertical resolution of the 532-nm analog channel of the Raman lidar was 7.5 m (see p. 50). Depending on the respective measurement setup the photon-counting data acquisition of the three-wavelength Raman lidar was set to 15 m resolution for the near-range telescope and 60 m for the far-range telescope, respectively. The height resolution of the wind lidar was 75 m.

The covered height range starts at about 400 m and typically reaches up to the top of the PBL. The range is limited by the Doppler wind lidar measurements. At lower

³URL: <http://www.thinkman.com/dimension4/index.htm>, 19 August 2008

heights scattered light from the transmitted laser pulse overloads the signal detection. Above the PBL, the aerosol content usually is too low to produce a sufficiently strong backscatter signal for coherent detection.

4.3.2 Vertical beam alignment by use of specular reflections from ice crystals

For measurements of vertical winds in the PBL it is very essential that the laser beam is vertically aligned, because the horizontal wind components are usually much larger. Assuming a horizontal wind speed of 10 m s^{-1} and measuring at 1 degree off-zenith one already obtains systematic errors on the order of 20 cm s^{-1} . The beam direction is adjusted with the folding mirror on the upper level of the Doppler lidar (see Fig. 4.5). For the alignment, a horizontally mounted back-reflecting mirror was installed behind the folding mirror in the laser beam path, which could be accurately aligned in the horizontal plane by a 0.1-mm/m water level. Then the folding mirror was adjusted until the back reflections were co-aligned with the transmitted beam direction. Thus a vertical alignment accuracy before the scanning unit of less than 1 mrad could be easily achieved.

However, the last optical element is the BSU on top of the container. The alignment and the accuracy of the BSU pointing stability in particular could be checked by ROTZ (rocking over the zenith) measurements (e.g., Thomas et al., 1990). I made use of specular reflections from large ice crystals in the virgae of altocumulus and cirrus clouds. These crystals orient themselves remarkably well in the horizontal direction because of their aerodynamic drag. The resulting backscattering from the specular reflections is larger by a factor of 10 or more than regular backscattering from ice crystals. Hence the lidar beam was *rocked* over the zenith with the BSU on the container roof.

During autumn and winter 2006 several of these measurements were carried out to study the angular dependence of specular reflections from cirrus clouds (Seifert et al., 2008). Figure 4.9 shows such an example measurement. On 10 October 2006 continuous zenith scans from $-2 \dots 2^\circ$ in steps of 0.2° were performed. For the forward direction (blue line) the azimuth angle of the scanner was set to 0° whereas it was set to 90° for the backward direction (orange line). The integration time for each angle was 5 s. As expected, the lidar return signal within the PBL ($< 1.1 \text{ km}$ height)

and also in some free-tropospheric aerosol layers (1.5–3 km) is independent of the scanning angle. In contrast, the ice-cloud virgae above 6.5 km show a backscattering which is strongly dependent on the zenith angle. It can be proved with these measurements that the accuracy of vertical alignment of the Doppler lidar beam behind the scanning unit is on the order of 0.2° , which is sufficient for measurements of the vertical turbulent flux.

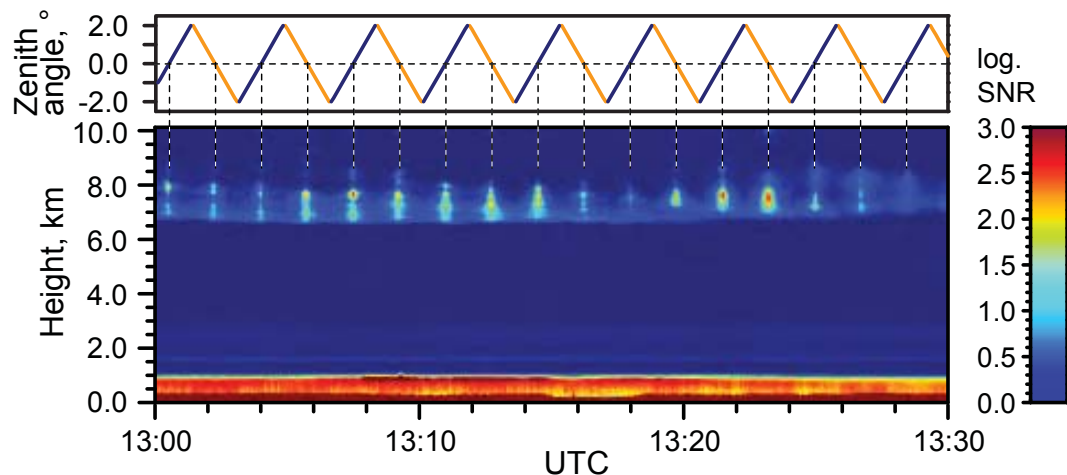


Figure 4.9: Rock-over-the-zenith scan with the Doppler lidar on 10 October 2006 in Leipzig. Top: zenith angle (blue - 0° , orange - 90° azimuth). Bottom: logarithm of the SNR of the spectral peak. A detailed discussion of these measurements is found in Seifert et al. (2008).

5 Measurements and results

The data for my investigations were taken at IfT which is located in the eastern suburbs of Leipzig. The city and its surroundings are affected by flat terrain in the Leipzig basin. About 90 km to the southeast the Erzgebirge (Ore Mountains) and in approximately the same distance to the northwest the Harz Mountains are located.

In 2006 and early 2007 intensive measurements with the wind lidar were performed at IfT whenever permitted by the weather conditions. Sixty-five measurements with the wind lidar were taken in 2006 and seven more observations in 2007. Sixty of them were exclusively measurements of vertical winds with high temporal resolution. These measurements were conducted to characterize the convective behavior of the PBL during the main seasons (spring, summer) of thermally driven turbulence. This dataset has been analyzed in a diploma work (Fruntker, 2009). Combined measurements with the Raman lidar MARTHA were performed less frequently, because they require much higher operating expenses. However, 16 combined datasets could be collected. A summary of all measurements is given in Fig. 5.1. Further measurements (indicated by grey color) mainly deal with ROTZ cirrus observations.

In the following sections, the golden days (yellow in Fig. 5.1) are discussed in detail. I selected two dry PBL developments, which were dominated by convection, to study the vertical exchange of aerosol mass in detail. Afterwards, five further measurement cases of vertical flux measurements are presented and compared. In the conclusion of this chapter the measured profiles of the aerosol mass fluxes are summarized by a standardized representation. Lastly, a discussion of the method is given.

5.1 Case study of 12 September 2006

The first data set that was investigated extensively by the application of the eddy correlation method for aerosol flux measurements was taken on 12 September 2006.

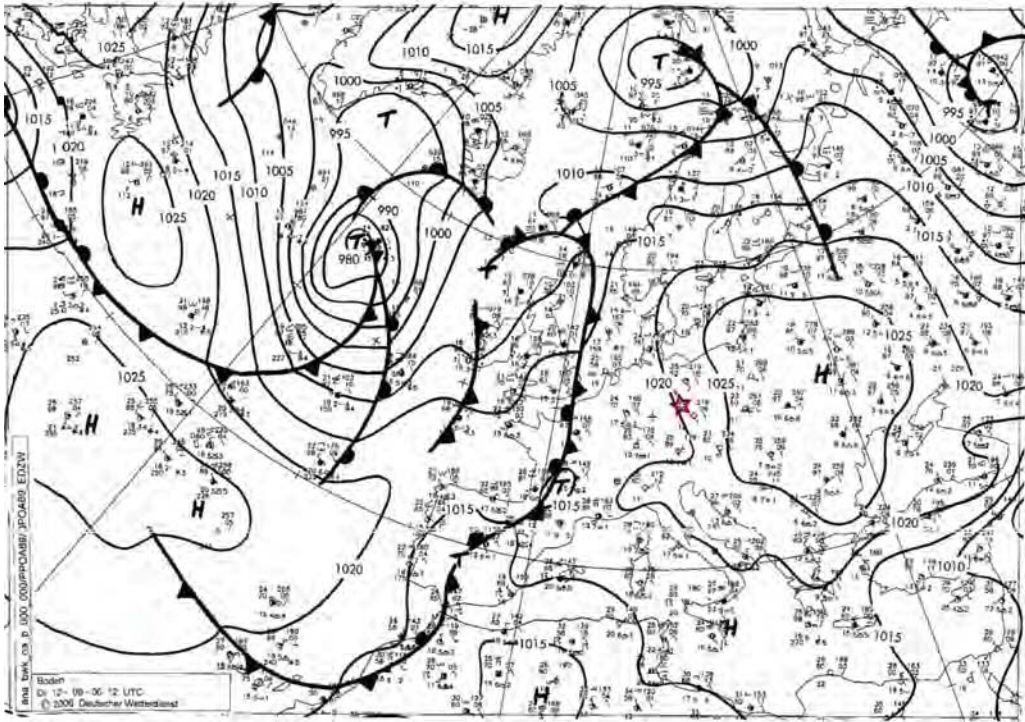


Figure 5.2: Surface (sea level) weather map of 12 September 2006, 12 UTC analysis, provided by Deutscher Wetterdienst and www.wetter3.de (download 6 Sep 2008). The lidar site is marked.

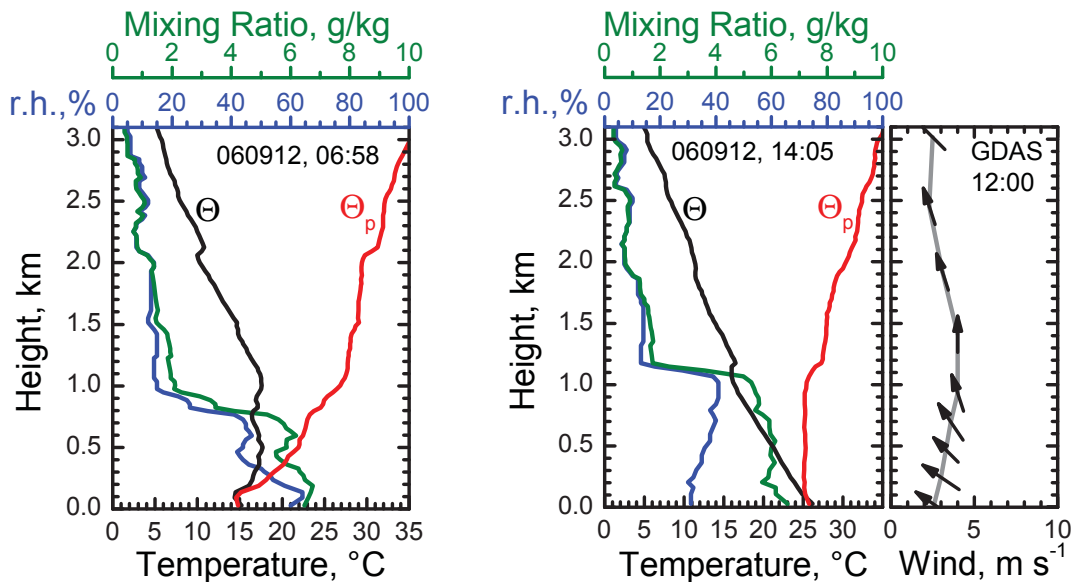


Figure 5.3: 12 September 2006: temperature (Θ), potential temperature (Θ_p), relative humidity (r.h.), and water-vapor mixing ratio obtained with collocated radiosondes launched at the lidar site at 0700 and 1400 UTC. The 1200-UTC GDAS reanalysis of the horizontal wind is shown, too (<http://www.arl.noaa.gov/READYamet.php>).

to the entrainment zone. The relative humidity was less than 40% throughout the entire PBL in the afternoon. Therefore, hygroscopic particle growth can be neglected in the further investigations. Additionally, a GDAS (Global Data Assimilation System) model reanalysis for the horizontal wind at 1200 UTC shows that southeasterly winds of $3\text{--}5\text{ m s}^{-1}$ dominated in the PBL.

Backward ensemble trajectories for 72 hours were computed with the Hybrid Single Particle Lagrangian Integrated Trajectory Model (HYSPLIT) and are presented in Fig. 5.4 (Draxler and Hess, 1998). They show that the air masses within the PBL originated mainly from the southeast, i.e. the Czech Republic, Austria, and Hungary.

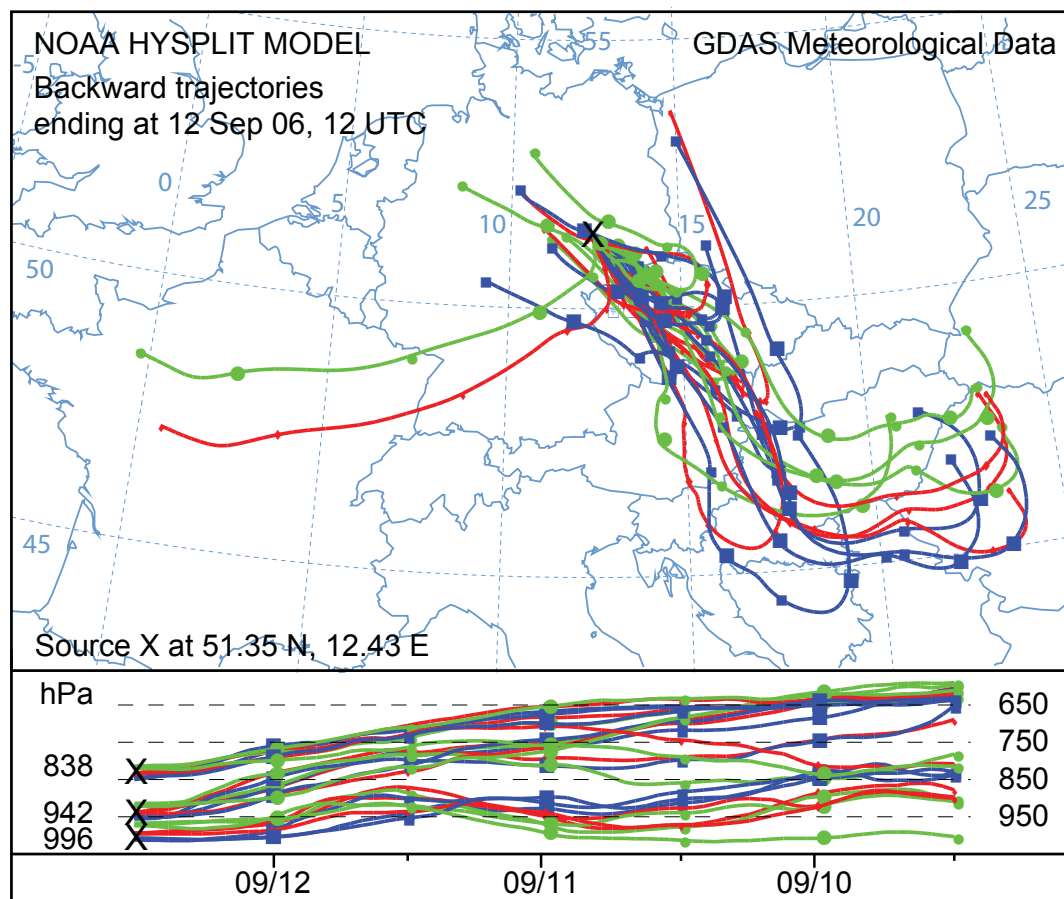


Figure 5.4: 72-h backward ensemble trajectories for Leipzig calculated with HYSPLIT. The heights of arrival are surface, 500, and 1500 m agl (pressure levels: 996, 942, and 838 hPa).

5.1.2 Lidar measurements

The IfT Raman lidar MARTHA and the Doppler wind lidar were used to measure coherent datasets of aerosol backscatter and vertical wind speed during daytime. Measurements from MARTHA were taken with the near-range telescope. The measurement with the Raman lidar was extended until nighttime to obtain accurate data for the characterization of microphysical aerosol properties. The far-range telescope was also used at nighttime to obtain reasonable reference values needed for near-range data calibration.

Figure 5.5 presents the PBL development during daytime between 0930 and 1730 UTC (1030 and 1830 local time, Central European Time). Additionally, the 1-hour averaged Raman solutions for the particle backscatter coefficient at 532 nm are plotted. In the morning the highest aerosol concentration is below 400 m. The turbulent mixing-layer height grows during the day to about 1200 m at 1600 UTC. Within the mixing layer the backscatter coefficient remains virtually constant. Calm conditions in the morning and evening hours can be observed in the vertical wind speeds, as well as the development of convective plumes during daytime. Thermal updraft regions (yellow and red) can be clearly distinguished from downward mixing processes (dark green). The highest velocities of thermals occur between 1230 and 1430 UTC. Additionally, the range-corrected signal of the 532-nm analog channel in the Raman lidar and the vertical wind speed show very good correlations indicating positive aerosol flux values.

From the evening measurements taken on 12 September 2006 profiles of particle backscatter coefficients at three wavelengths and of particle extinction coefficients at two wavelengths were derived with the Raman method. The backscatter coefficient at 1064 nm was calculated with the Raman method using the 607-nm nitrogen channel as reference since no Raman-shifted signal from 1064 nm is available. Equation (3.9) was adopted for this situation with three involved wavelengths (532, 607, and 1064 nm) accordingly. The signals from the far-range measurements were calibrated at a height level from 13–16 km within the stratosphere where the particle concentration is usually close to zero. A constant reference value of $0.01 \text{ Mm}^{-1} \text{ sr}^{-1}$ was used for the determination of the particle backscatter coefficients at 355, 532, and 1064 nm, respectively. With far-range measurements the average reference values between 2 and 4 km for the near-range calculations were derived.

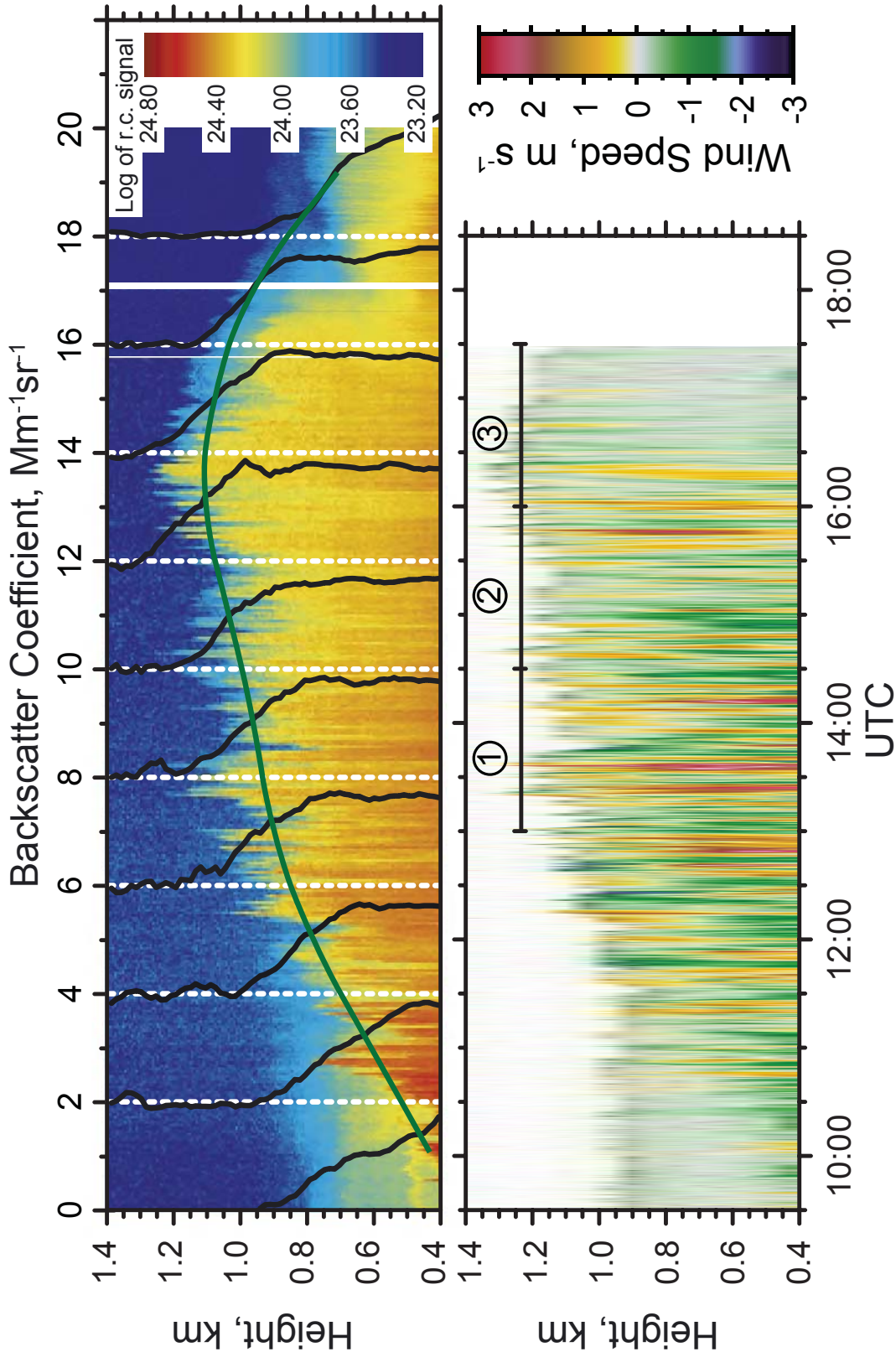


Figure 5.5: PBL development observed with Raman lidar and Doppler wind lidar on 12 September 2006. Top: range-corrected 532-nm signal (resolution 7.5 m, 5 s) and one-hour-averaged profiles of the backscatter coefficient at 532 nm. The profiles of β_{532}^p are shifted by $2 \text{ Mm}^{-1} \text{ sr}^{-1}$ per hour. The green line represents the averaged CBL height (where β_{532}^p drops to one half). Bottom: vertical wind speed (resolution 75 m, 5 s). The labeled time intervals 1–3 are subject of further investigation.

The data for the time period from 1900–2000 UTC are shown in Fig. 5.6. The resulting lidar ratios of 72 ± 5 sr for 355 and 532 nm indicate relatively small, absorbing particles which are typical for anthropogenic pollution from eastern Europe. The data at 670 m height were used as input for the inversion scheme to determine microphysical particle properties. Due to the well-mixed conditions during daytime the aerosol properties in this height level were representative for the ensemble of particles obtained in the PBL during the whole day. In addition, systematic retrieval errors resulting, e.g., from the incomplete overlap of laser beam and receiver field of view, can be neglected at this height level.

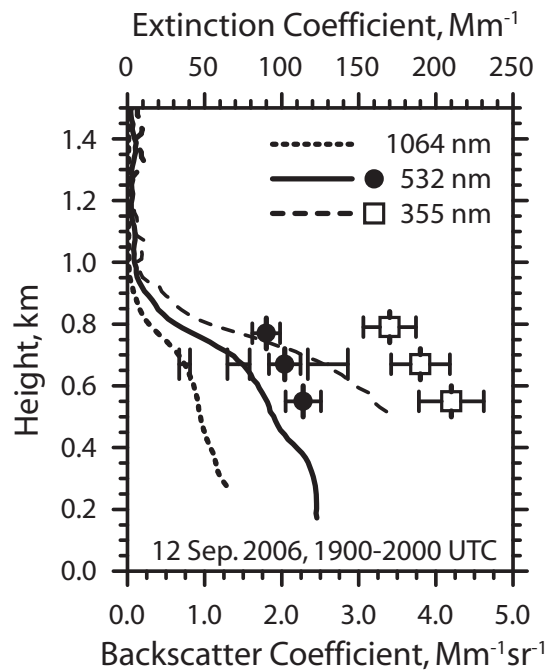


Figure 5.6: Profiles of the particle backscatter coefficient at 355, 532, and 1064 nm (lines) and of the particle extinction coefficient at 355 and 532 nm (symbols) obtained between 1900 and 2000 UTC on 12 September 2006. The values and uncertainties at 670 m height were used as input for the lidar data inversion scheme.

5.1.3 Microphysical parameters of aerosol particles

Microphysical aerosol properties were obtained from the derived optical data with the inversion scheme. The input parameters and the inversion results for this case

are shown in Tab. 5.1. The uncertainties given for the input data are the standard deviations within the averaged height interval.

The derived particle volume concentration was found to be $19 \pm 8 \mu\text{m}^3\text{cm}^{-3}$ from the lidar data and agrees very well with data obtained from regular *in situ* measurements with a differential-mobility particle sizer (DMPS) at IfT (inlet at 16 m above the ground). From the DMPS measurements the mean and the standard deviations of two selected time periods of six hours each were considered for comparison with the lidar data. The effective, i.e. the area-weighted mean, particle radius retrieved from the lidar data of 180 ± 41 nm compares well to the value of 151 nm from the *in situ* data at ground. The differences in the effective radius and the number and surface concentrations result from the different size regimes which the methods are sensitive to. The DMPS can observe particles from >3 nm in diameter, i.e., it covers the nucleation ($D_p < 10$ nm), the Aitken ($10 < D_p < 100$ nm), and the accumulation ($0.1 < D_p < 1 \mu\text{m}$) modes. The DMPS large cut-off diameter is 800 nm, whereas the inversion is sensitive to coarse-mode particles ($>1 \mu\text{m}$), too. In addition, the lidar data inversion results are insensitive for particles smaller than about 160 nm in diameter. Therefore, particles measured with DMPS having a diameter smaller than 160 nm were neglected for the comparison with the inversion results. Neglecting the small particles results in a truncated volume concentration of 87% of the total volume concentration for this case. However, for the surface-area and the number concentrations this reduction is much stronger, so that only 66% and 9%, respectively, are covered.

Figure 5.7 additionally shows the comparison of the derived volume distributions from the inversion and averaged results from IfT's *in situ* DMPS observations over two 6-h time intervals. The error bars indicate the standard deviations from 18 single DMPS measurements in this time interval and the maximum and minimum solutions from the inversion, respectively. Good agreement of both methods is found for the accumulation-mode particles although the data are derived from a lidar measurement at the PBL top and from measurements at the ground. The shown coarse mode at $D_p = 1.5 \mu\text{m}$ is not significant as indicated by the error bars. Unfortunately, *in situ* observations are not available at this size range for the time of measurement.

Profiles of the backscatter-related Ångström exponents \hat{a}^β for four time intervals are presented in Figure 5.8. The long-wavelength exponent shows nearly constant values of 0.9 for all heights and all time intervals. The short-wavelength Ångström

Table 5.1: Input data and inversion results for 12 September 2006. For the compared DMPS data only particle diameters >160 nm were considered. The M_d/β_{532}^p factor was derived with a mean particle density of 1.6 g cm^{-3} .

Inversion input data	355 nm	532 nm	1064 nm
Backscatter coef., $\text{Mm}^{-1}\text{sr}^{-1}$	2.60 ± 0.26	1.44 ± 0.14	0.74 ± 0.07
Extinction coef., Mm^{-1}	190 ± 20	102 ± 10	
Lidar ratio, sr	73 ± 5	71 ± 5	
Ångström exp. \hat{a} (355, 532 nm)	1.54 ± 0.36		
Microphysical parameters	Lidar	DMPS 12–18 UTC	DMPS 18–24 UTC
Effective radius, nm	180 ± 41	152 ± 13	151 ± 19
Number concentration, cm^{-3}	1300 ± 460	1375 ± 101	1750 ± 218
Surface-area conc., $\mu\text{m}^2\text{cm}^{-3}$	320 ± 81	268 ± 22	339 ± 42
Volume conc., $\mu\text{m}^3\text{cm}^{-3}$	19 ± 8	13.6 ± 1.2	17.1 ± 2.2
Mass-to-backscatter ratio			
M_d/β_{532}^p , $\mu\text{g m}^{-3} \text{Mm sr}$	21.1 ± 8.9		

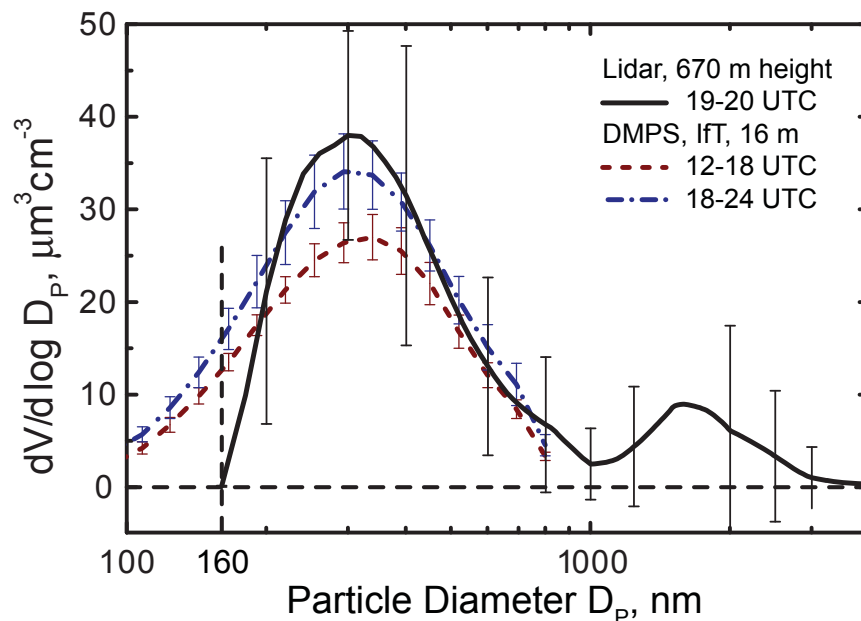


Figure 5.7: Aerosol volume distributions derived from lidar data inversion and from in situ measurements with DMPS on 12 September 2006.

exponent remains at values around 1.4. This behavior of the Ångström exponents, which are rather sensitive to any small changes in the aerosol characteristics, again indicates very stationary aerosol properties and the absence of hygroscopic growth during the entire day.

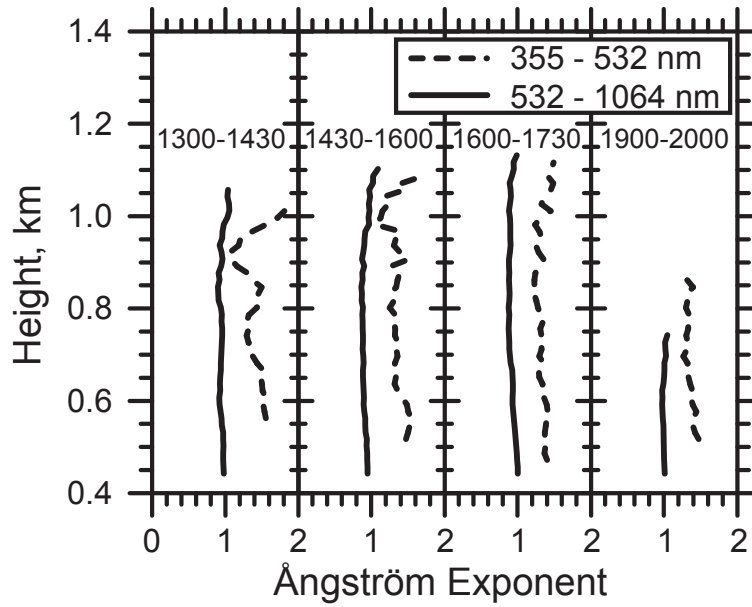


Figure 5.8: Backscatter-related Ångström exponents for the time periods 1300–1430, 1430–1600, 1600–1730, and 1900–2000 UTC for two wavelength intervals.

Figure 5.9 shows the time series of the AOD in the PBL at 532 and 1064 nm. The AOD was calculated from the height-integrated backscatter-coefficient profiles with an extinction-to-backscatter ratio of 75 sr (cf. Fig. 5.6). The backscatter coefficients were assumed to be constant in the region of incomplete overlap between laser beam and receiver field of view below 300 m where no trustworthy data can be obtained. This assumption may lead to a bias in the AOD in the morning and evening hours when the aerosol is not well mixed. Nevertheless, only a slight variation around the mean PBL AOD values of 0.11 and 0.06 at 532 and 1064 nm, respectively, was found over the whole day. Unfortunately, the AERONET (Aerosol Robotic Network) Sun photometer at IfT was not available for comparison of optical depths during 2006. It was used in Morocco during the SAMUM 2006 field campaign and had to be sent for recalibration to Greenbelt, Maryland, in August–October 2006.

In summary, it can be stated that information obtained from radiosoundings, lidar

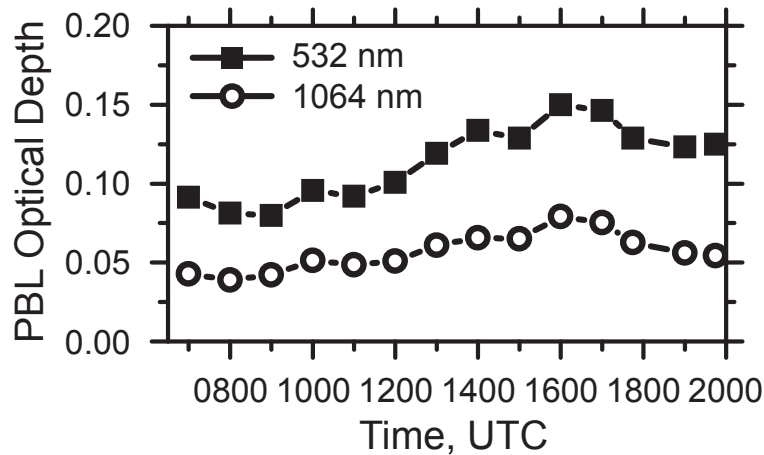


Figure 5.9: Time series of the AOD in the PBL on 12 September 2006. The AOD was calculated from the integrated backscatter coefficients multiplied with a lidar ratio of 75 sr.

measurements, and *in situ* observations clearly indicates stationary aerosol conditions and low relative humidity throughout the PBL during the entire measurement period on 12 September 2006. There is no indication of a change of air mass, aerosol composition, and size distribution and no indication of particle growth because of water uptake. Therefore, temporal and spatial variations of the particle backscatter coefficient can explicitly be attributed to turbulent mixing and vertical transport. The eddy-correlation method is applicable without restrictions, and particle mass fluxes can be calculated according to Eq. (3.16)–(3.19). A conversion factor M_d/β_{532}^p of $21.1 \pm 9 \mu\text{g m}^{-3} \text{Mm sr}$ was derived for this specific day. It results from the volume concentration of $19 \pm 8 \mu\text{m}^3 \text{cm}^{-3}$ obtained for $\beta_{532}^p = 1.44 \text{Mm}^{-1} \text{sr}^{-1}$ (cf. Tab. 5.1) and a particle density of 1.6g cm^{-3} which is typical for continental, ammonium-sulfate-like particles with a volume water content of 20% (Van Dingenen et al., 2004).

5.1.4 Spectral analysis

Figure 5.10 (top and middle) presents the variance spectra of the time series of vertical wind speed and backscatter coefficient at 800 m height for the three time intervals from 1300–1430, 1430–1600, 1600–1730 UTC. The spectra were smoothed in the logarithmic frequency space. The total variance of the backscatter coefficient decreased with time, because the aerosol particles approached well-mixed conditions

as a result of vertical exchange processes. The variance of the vertical wind speed decreased in the third time interval, because the convection slowed down.

At high frequencies the spectra cover at least some part of the inertial subrange ($\nu^{-5/3}$ roll-off), where the TKE of large eddies is successively subdivided and re-distributed among smaller eddies. The energy-containing (and flux-covering) part of the spectrum, where the slope of the spectrum transients to constant values (in this $\log S(\nu)$ vs. $\log \nu$ representation), is also covered. Noise on the time series, which gives a constant contribution to the spectra at high frequencies, is found for the backscatter coefficient only. Assuming a mean horizontal wind velocity of 5 m s^{-1} , it can be estimated that eddy sizes of $>50 \text{ m}$ are covered by the measurement.

By calculating the cospectrum of vertical-wind and particle-backscatter fluctuations, we can find out which frequencies mainly contribute to the turbulent flux. Figure 5.10 (bottom) shows the cospectra for the measurement height of 800 m and the three time intervals. The presentation of $\nu C(\nu)$ vs. $\log \nu$ preserves the area and gives realistic weight to high frequencies. The cospectrum indicates contributions to the vertical flux in the frequency range of 2×10^{-2} to $2 \times 10^{-4} \text{ Hz}$. With a horizontal wind velocity of 5 m s^{-1} this range corresponds to horizontal sizes of 250 m to 25 km. The maximum occurs at $\nu = (2.5\text{--}4) \times 10^{-3} \text{ Hz}$ corresponding to eddy sizes of 1.2–2.0 km. This value agrees very well with the dominant frequency ν_{max} from Eq. (2.27) of $3.12 \times 10^{-3} \text{ Hz}$ predicted from the horizontal flux integral scale $\Lambda_{w,\beta}$ of 51 s (1.6 km). The flux integral scale was estimated as the minimum of the vertical-wind and backscatter integral scales after Eq. (2.19). For frequencies lower than $2.5 \times 10^{-3} \text{ Hz}$ the cospectrum becomes rather unpredictable. As often found in the CBL, eddies and other turbulent structures at very different scales are responsible for the overall turbulent flux (e.g., Kaimal et al., 1976). The negative values at $\nu = 1.5 \times 10^{-3} \text{ Hz}$ in the cospectrum (3.3 km) cannot be fully explained. However, this effect reduces the vertical flux significantly to approximately 80% of the value without this contribution. It can be discussed that the effect results from organized turbulence features like roll structures.

The vertical-wind and backscatter integral scales were 51 and 55 s, respectively, at 700–800 m height and increased to values of 60 and 90 s, respectively, in the height region of 900–1000 m. The fact that no significant contributions are found in the cospectrum at frequencies higher than 2×10^{-2} and lower than $3 \times 10^{-4} \text{ Hz}$ supports the strategy of taking measurements with a resolution of 5–10 s and a minimum length

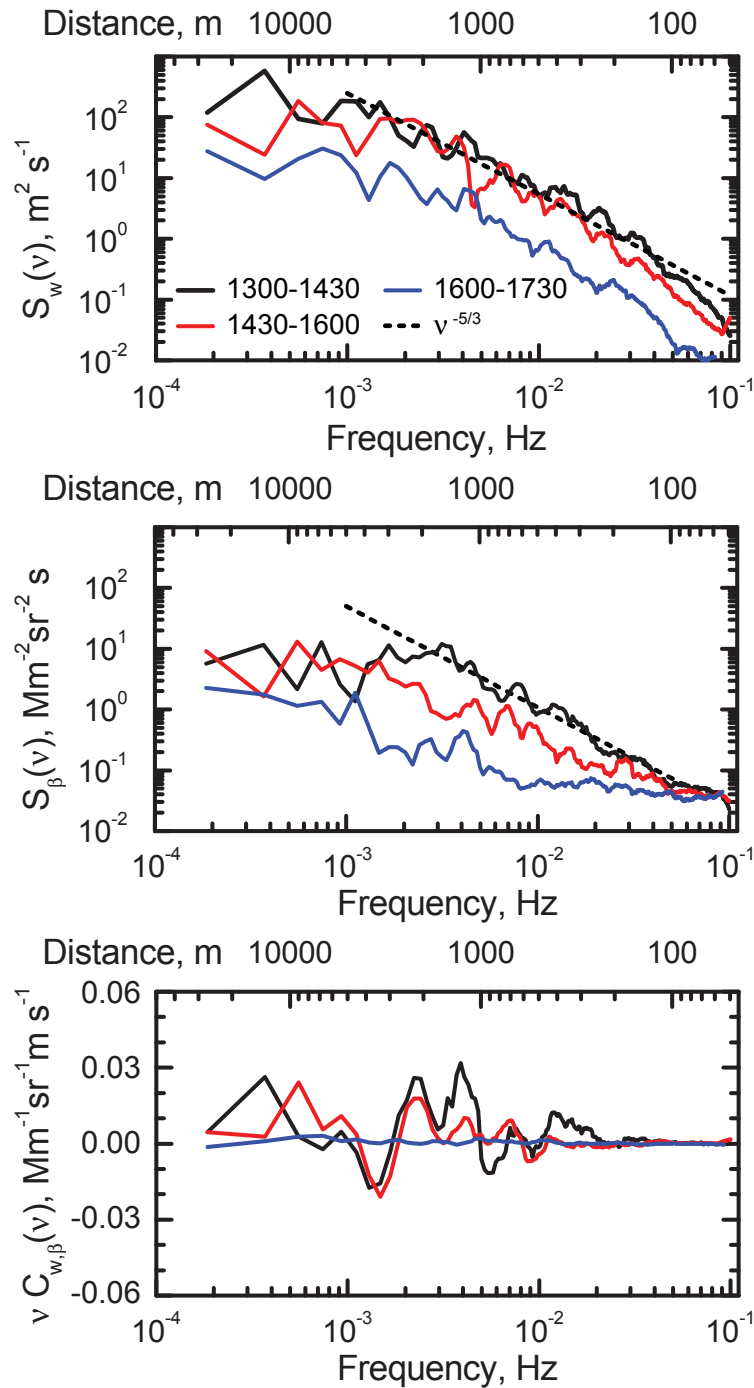


Figure 5.10: Top and middle: power spectral density functions of the vertical wind speed and the backscatter coefficient at 800 m height level for three time intervals between 1300 and 1730 UTC. The expected $v^{-5/3}$ roll-off for the inertial sub-range of turbulence is indicated. Bottom: cospectrum of vertical-wind and particle-backscatter fluctuations for the same height and time intervals. The top axes have been converted with a wind speed of 5 m s^{-1} .

of the time series of 60–90 min for the flux computation. The latter values are also in agreement with the findings of Lenschow et al. (1994) who showed that systematic errors due to *flux losses* are $<5\%$ if the length of the measurement period is $\geq 100 \Lambda_{w,\beta}$, i.e. 80–100 min in this case. Therefore, I chose time series of 90 min length for the investigations below.

The findings on the relevant time scales and eddy sizes are in good agreement with the results from ground-based remote-sensing measurements of water-vapor (Senff et al., 1994; Giez et al., 1999) and ozone fluxes (Senff et al., 1996). Horizontal integral scales of the vertical wind speed between 50 and 200 s were reported for different measurement cases by Giez et al. (1999). Dominant eddy sizes for the upward transport of water vapor of 1–2.5 km (Senff et al., 1994; Giez et al., 1999) and for the downward mixing of ozone of approximately 1.5–3 km (time scale of 10 min, horizontal wind speed not given in the paper) were obtained.

5.1.5 Vertical profiles of aerosol mass flux

Figure 5.11 shows profiles of the aerosol mass flux for three selected time periods (cf. Fig. 5.5). The conversion factor of $21.1 \mu\text{g m}^{-3} \text{Mm sr}$ has been applied to convert the measured values of $\overline{\beta'w'}$ (upper axis) to the aerosol mass flux $\overline{m'w'}$.

The linear flux profile observed from 1430–1600 UTC is consistent with a source- and sink-free CBL and no or constant advection of aerosol. The flux profile is then completely defined by the surface flux and the entrainment flux. During the CBL development (time period 1300–1430 UTC), the strongest turbulent flux is observed in the entrainment zone where the growing CBL mixes with the cleaner air from the residual layer. Above that region, the flux decreases to zero. In the time period from 1600–1730 UTC, the turbulent aerosol flux profile is close to zero throughout the PBL because the atmospheric convection slowed down in the late afternoon.

The obtained values of the aerosol mass flux of $0.5\text{--}2 \mu\text{g m}^{-2}\text{s}^{-1}$ in the active upper CBL are reasonable. This can be proved with a simplified budget estimate, which may give an idea on the magnitude of the entrainment flux. From Fig. 5.5 it can be seen that the backscatter coefficient between 800 and 1000 m increased from values close to 0 in the morning to values around $1.8 \text{Mm}^{-1}\text{sr}^{-1}$ in the afternoon. With the M_d/β_{532}^p conversion factor this corresponds to an increase of the mass concentration of $38 \mu\text{g m}^{-3}$. Let us assume that this change is only caused by convective mixing of

particle-rich air from the lower CBL with clean air from the free troposphere, where the aerosol flux is zero. Then a mass flux in the entrainment zone of $2 \mu\text{g m}^{-2}\text{s}^{-1}$ would fill an atmospheric column of 200 m depth with the respective amount of particles within one hour. This corresponds very well with the observed CBL growth rate of about 150–200 m per hour before 1300 UTC. Later (1430–1600 UTC) the mass flux in the upper PBL was of the order of $0.5\text{--}1 \mu\text{g m}^{-2}\text{s}^{-1}$ which again is consistent with the observed increase of the PBL height of 50–75 m per hour after 1400 UTC (cf. Fig. 5.5). As mentioned, such a budget determination is a very simplified approach and not valid in general. It neglects sources and sinks of particles in the PBL as well as horizontal and vertical advection. However, because of the lack of validation methods, it is used as a consistency check here.

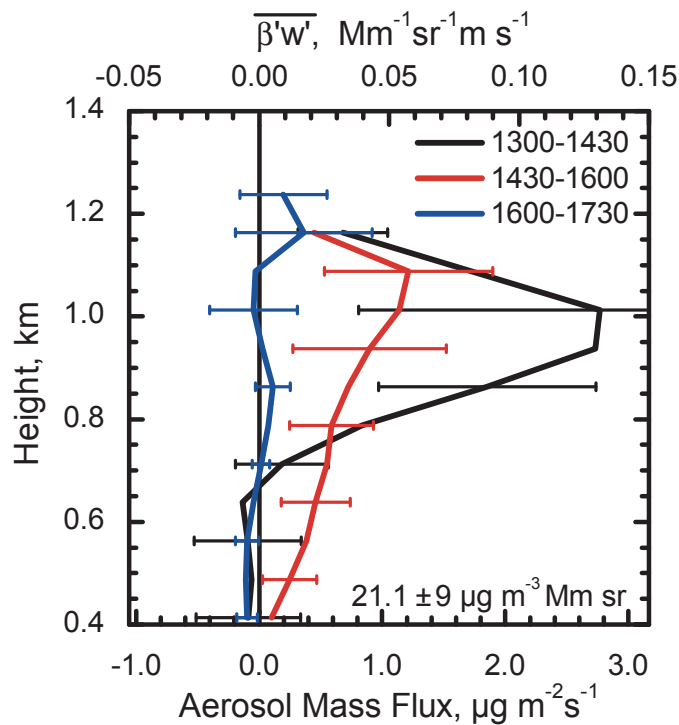


Figure 5.11: Profiles of aerosol mass flux for three time periods between 1300 and 1730 UTC on 12 September 2006. The upper axis shows the covariance of the backscatter coefficient and the vertical wind speed. The error bars indicate the sampling error.

5.1.6 Errors

In Tab. 5.2 the relative errors of the aerosol mass flux for three height levels for the time period 1430–1600 UTC are summarized. The dominating error of the determined aerosol mass flux is the sampling (random) error $\sigma_{F,\text{samp}}$ which was calculated after Eq. (3.26). It is proportional to the horizontal flux integral scale divided by the sampling time. As mentioned in Subsection 2.4.2, the flux integral scale is estimated from the vertical-wind and backscatter integral scales with Eq. (2.19). The systematic deviation from the ensemble mean, which results from the finite length of the time series, is found to be of the order of 2% [after Eq. (3.32)] and can therefore be neglected.

Table 5.2: Relative errors of the aerosol mass flux for different heights and sources for 1430–1600 UTC. The sampling error $\sigma_{F,\text{samp}}$, the instrumental noise error $\sigma_{F,\text{instr}}$, the error due to horizontal and vertical incoherences of the datasets $\sigma_{F,h}$ and $\sigma_{F,v}$, respectively, and the microphysical uncertainty $\sigma_{F,\text{micro}}$ are given.

Height	$\sigma_{F,\text{samp}}$	$\sigma_{F,\text{instr}}$	$\sigma_{F,h}$	$\sigma_{F,v}$	$\sigma_{F,\text{micro}}$
487 m	88%	10%	<11%	<21%	50%
787 m	58%	4%	<2%	<23%	50%
1012 m	51%	2%	<6%	<30%	50%

The flux error due to instrumental noise $\sigma_{F,\text{instr}}$ is calculated with Eq. (3.30). In this case, the error is small compared to the sampling error. An upper limit for the instrumental noise of the backscatter and vertical-wind measurements is estimated from the noise level of the power spectral density functions in Fig. 5.10 to $\sigma_{\beta',\text{instr}} = 0.06 \text{ Mm}^{-1} \text{ sr}^{-1}$ and $\sigma_{w',\text{instr}} < 0.04 \text{ m s}^{-1}$, respectively (see Fig. 4.3).

Errors because of possible incoherences of the datasets in horizontal and vertical direction $\sigma_{F,h}$ and $\sigma_{F,v}$, respectively, were estimated by shifting the datasets by one bin (5 s and 75 m) in either direction, followed by a recalculation of the flux profile and a comparison to the original one. The maximum discrepancy found in this way was 30%. However, it can be assumed that the respective errors are much smaller because the measurements were synchronized in time and the coherence of the height profiles has been checked on several occasions, e.g., in the presence of sharp gradients in the signals at cloud bases.

The error of the conversion factor from backscatter coefficient to aerosol volume and mass concentrations follows from the uncertainties of the inversion procedure.

For this dataset, the standard deviation of the total volume concentration derived from the single solutions of the size distribution was found to be 43%. If an additional uncertainty of the particle density ρ_p and a stability of the conversion factor M_d/β_{532}^p during the day of 20% each is assumed, the flux error because of the uncertain microphysical parameters $\sigma_{F,\text{micro}}$ is 50%.

5.2 Case study of 26 April 2007

5.2.1 Synoptic situation

On 26 April 2007 the meteorological conditions were similar to 12 September 2006. Leipzig was influenced by a high-pressure system over eastern Europe. Figure 5.12 illustrates the situation by the surface weather plot from DWD.

Ensemble backward trajectories for 72 hours were calculated with the HYSPLIT model for 12 UTC and are shown in Fig. 5.13. The plot indicates that the air masses within the PBL (surface to 1.5 km height) arrived from easterly and southeasterly directions, mainly crossing Poland, Slovakia, and the Czech Republic.

Results from the respective radiosoundings at Lindenberg¹ (6 UTC, 150 km north-east of IfT) and at IfT (12 UTC) are presented in Fig. 5.14. A strong inversion at 200 m occurred in the morning hours. Hence a high aerosol mass concentration at the ground could be expected which had accumulated during the night. Therefore, a strong vertical gradient was formed and a high vertical aerosol flux in the early hours of the CBL development was expected. The relative humidity was a little higher during daytime compared to the first case study but remained below 60% at the PBL top at 1.5 km. At 1200 UTC well-mixed conditions were found for water vapor throughout the CBL. Wind speeds in the CBL were around 4–5 m s^{-1} from easterly directions as the GDAS model reanalysis for Leipzig at 1200 UTC showed.²

5.2.2 Lidar measurements

The combined lidar measurements on 26 April 2007 were taken from 0745–1700 UTC (0845–1800 local time) and are shown in Fig. 5.15. In contrast to 12 September 2006,

¹<http://weather.uwyo.edu/upperair/sounding.html>, download 17 March 2008

²<http://www.arl.noaa.gov/READYamet.php>

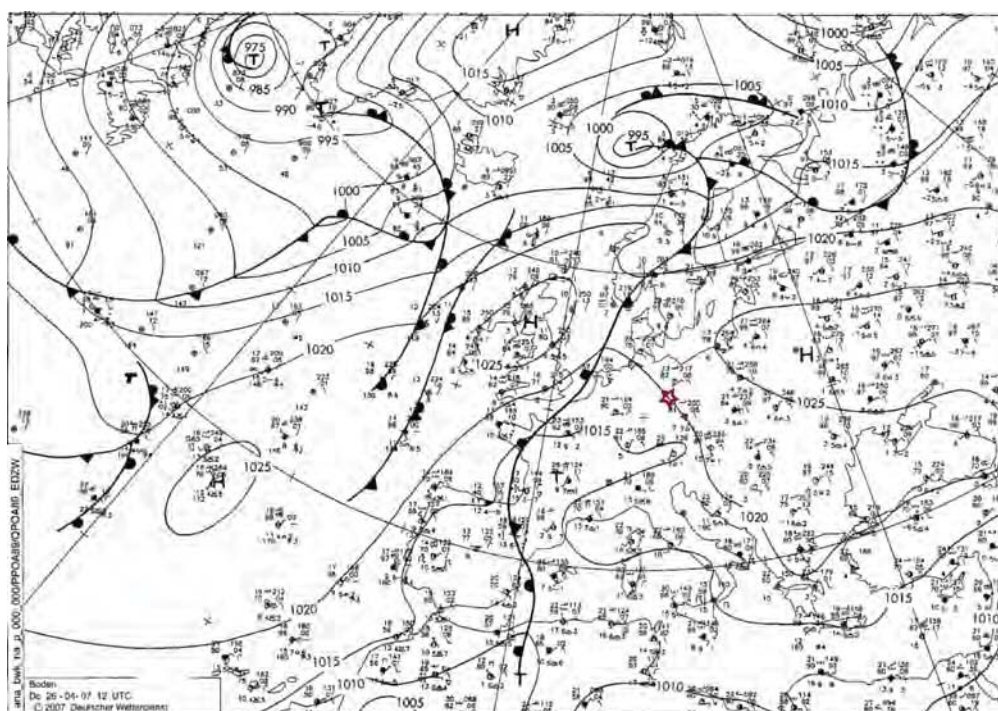


Figure 5.12: DWD surface (sea level) weather map from 26 April 2007, 12 UTC analysis. The lidar site is marked.

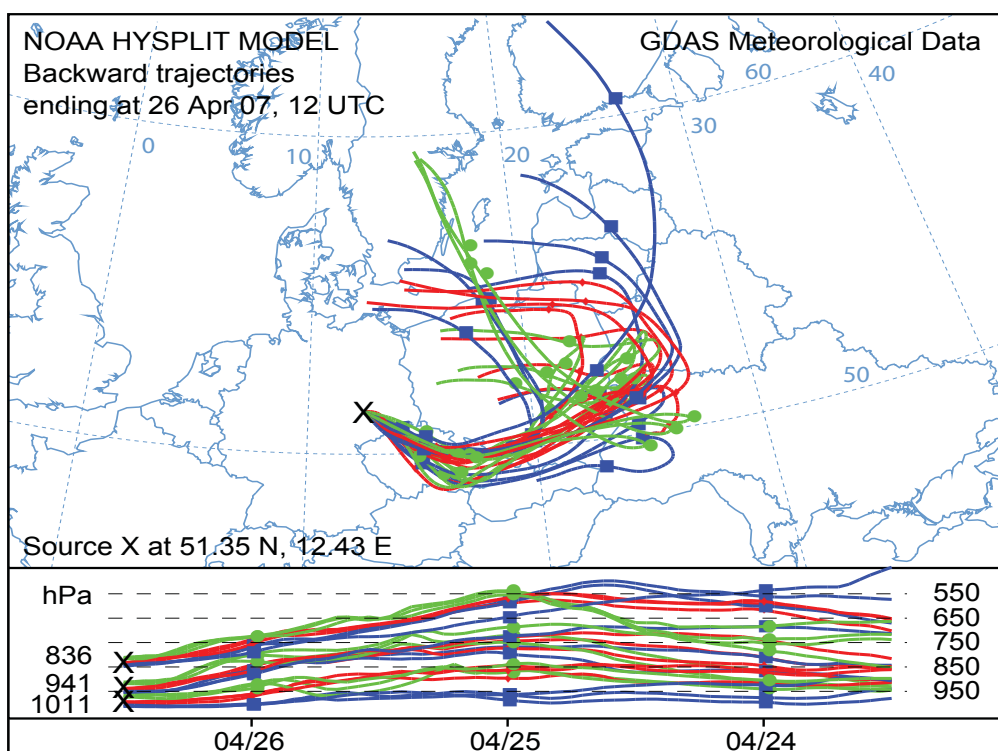


Figure 5.13: 72-h backward ensemble trajectories for Leipzig calculated with HYSPLIT. The heights of arrival are surface, 500, and 1500 m agl (pressure levels: 1011, 941, and 836 hPa).

the measurement with the Raman lidar was performed by use of the far-range telescope. The apparent drop of the range-corrected signal below 700–800 m height is caused by the incomplete lidar overlap for the far-range receiver. This limits the observation of the particle backscatter coefficient, which was derived with the Klett method, to heights greater than 800 m. However, it results in more accurate data at the top of the PBL because of the higher signal-to-noise ratio. Additionally, the backscatter coefficient derived with the Raman method is shown for 1-hour intervals. The bottom graph shows the vertical wind speed which was simultaneously measured with the Doppler lidar.

The experimental setup was equal to the previous case (except the use of the Raman lidar far-range telescope), i.e., a temporal resolution of 5 s for both systems and a vertical resolution of 75 m and 7.5 m for the Doppler lidar and the Raman lidar analog channel were chosen, respectively. The Raman lidar measurement was stopped at 1700 UTC when the convection slowed down. At nighttime, far-range and near-range measurements were taken from 1935–2110 UTC and from 2115–2148 UTC for a comprehensive aerosol analysis, respectively.

Until 0900 UTC a residual layer was present up to a height of 1.5 km where no vertical motion was observed. The largest growth rates of the CBL were obtained in the two hours between 0900 and 1100 UTC. The mixing-layer height increased from 400 to 1400 m, i.e. with a growth rate of about 500 m per hour. A much smaller growth rate was observed afterwards until 1530 UTC when the maximum height of the CBL reached 1650 m. At this time, the vertical motion slowed down and no further growth occurred.

Figure 5.16 gives a closer look at the turbulent mixing during that day. The four most convective hourly periods are shown in detail. Respective updraft velocities up to 5 ms^{-1} were found. Wind speeds in the strongest downdrafts were around -2 ms^{-1} . Heavily particle-loaded plumes were rising until 1045 UTC and were mixed upwards into the residual layer. Some updrafts around 1025 and 1050 UTC were followed by strong downdrafts (see in the backscatter-coefficient plot, blue areas just before 1030 and 1055 UTC). These intrusions, labeled with [0] and [2], mixed the clean air from the free troposphere remarkably deep into the CBL. This clearly indicates an upward (positive) turbulent aerosol flux in the CBL for heights greater than 800 m.

At around 1100 UTC the situation changed. While before the updrafts were found

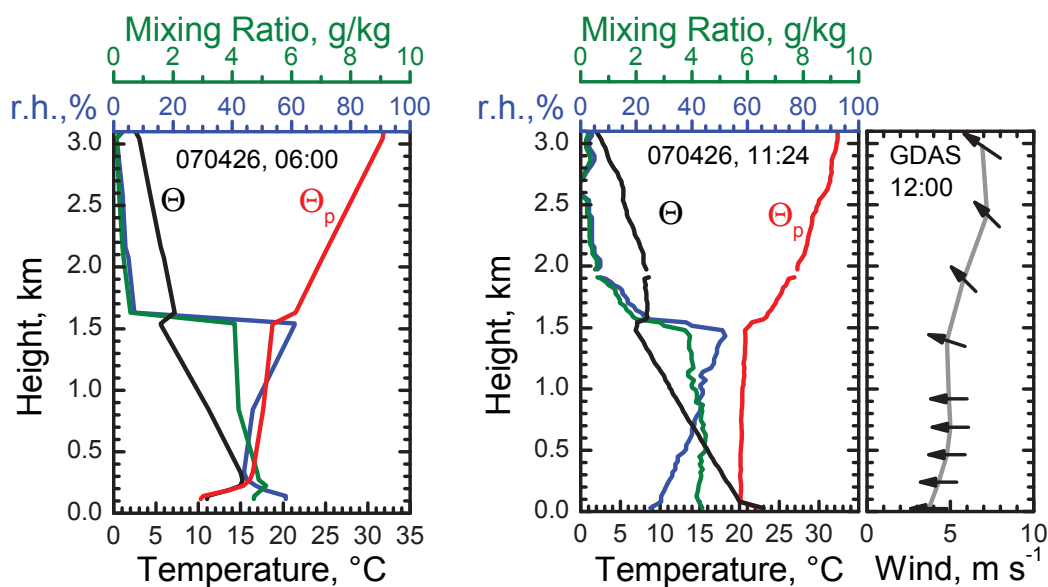


Figure 5.14: Vertical profiles of temperature, potential temperature, relative humidity, and water-vapor mixing ratio from radio soundings on 26 April 2007. Left: 0600 UTC sounding at Lindenberg. Right: sounding at IfT at 1124 UTC and horizontal wind from the 1200 UTC GDAS model reanalysis.

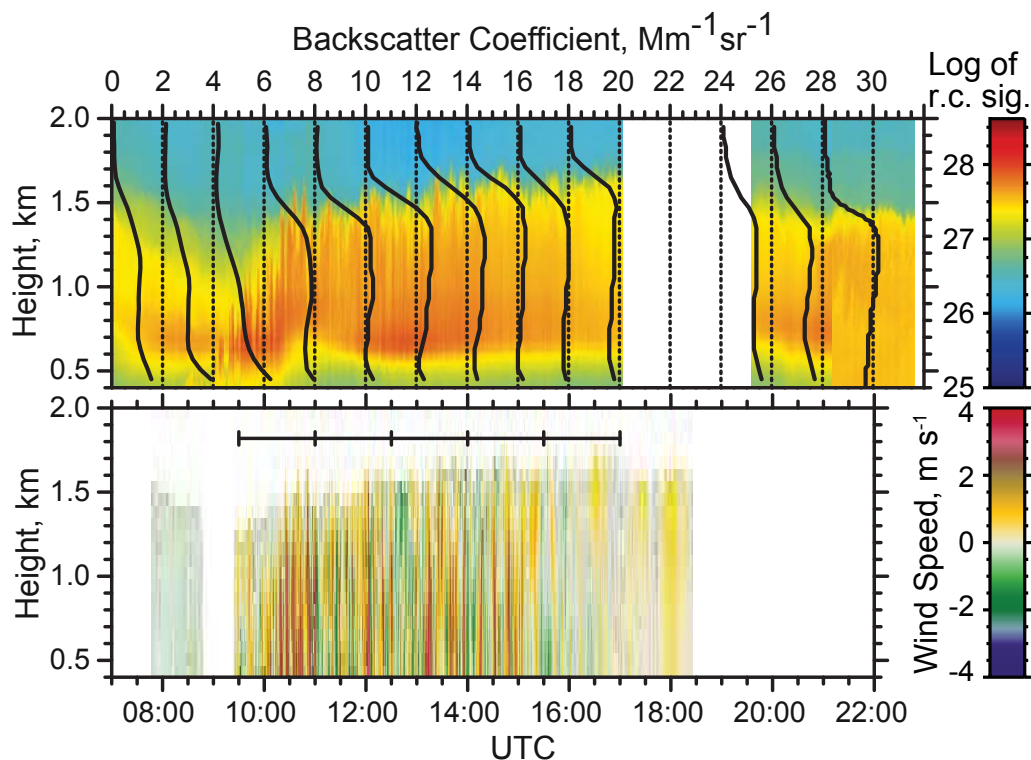


Figure 5.15: PBL development observed with MARTHA and WiLi on 26 April 2007. Top: range-corrected signal and one-hour-averaged profiles of the backscatter coefficient at 532 nm. The profiles of β_{532}^p are shifted by $2 \text{ Mm}^{-1} \text{ sr}^{-1}$ per hour. Bottom: vertical wind speed. The time intervals for the flux calculation are shown.

in conjunction with increased backscatter coefficients, e.g., [1] and others, after 1100 UTC updrafts were found simultaneously with decreased backscatter coefficients. Some of these events are labeled with [3]–[7]. At 1145 UTC [4] it is also indicated that a downdraft coincided with increased backscatter coefficients. Consequently, this anticorrelation results in a negative aerosol flux from the upper region of the CBL downwards as will be discussed later.

At 1200 and 1220 UTC, [5] and [6], it was observed that the aerosol flux changed its sign with height. Up to 1.3–1.4 km height anticorrelation in w' and β' —and thus downward mixing—was found. Above that height, both values correlated which indicates a positive flux in the entrainment zone. In the course of time, the vertical aerosol gradient was reduced by turbulent downward mixing, as indicated by the two lines in Fig. 5.16, 1200–1300 UTC.

Although much smaller, between 1300 and 1400 UTC there was still downward mixing present for heights up to 1.0–1.1 km. In regions [8] and [9] in Fig. 5.16 we see that this process almost removed the gradient of the backscatter coefficient. Above, the upward mixing process in the entrainment zone was still active.

The origin of the increased mean backscatter coefficient (see also top of Fig. 5.15) in the upper third of the PBL remains unclear. However, four possibilities seem to be reasonable:

- advection of aerosol from the southeast or from local sources,
- entrainment of large parcels of air prior to the arrival at the lidar site,
- increased relative humidity at the CBL top and hygroscopic growth of particles,
- new formation of particles at the top of the CBL.

The first item is the most plausible. About 70 and 100 km to the southeast of Leipzig are the cities of Chemnitz and Dresden. The southeast of Leipzig is also affected by agriculture which could be a source of local aerosol particles, too. Unfortunately, further information about advection processes was not available on such short time scales. Several lidar stations in the line of advection or airborne measurements would have been necessary in order to obtain such data.

Entrainment of aerosol into higher regions could have happened during the first strong convective events. This mechanism might have transported large amounts of

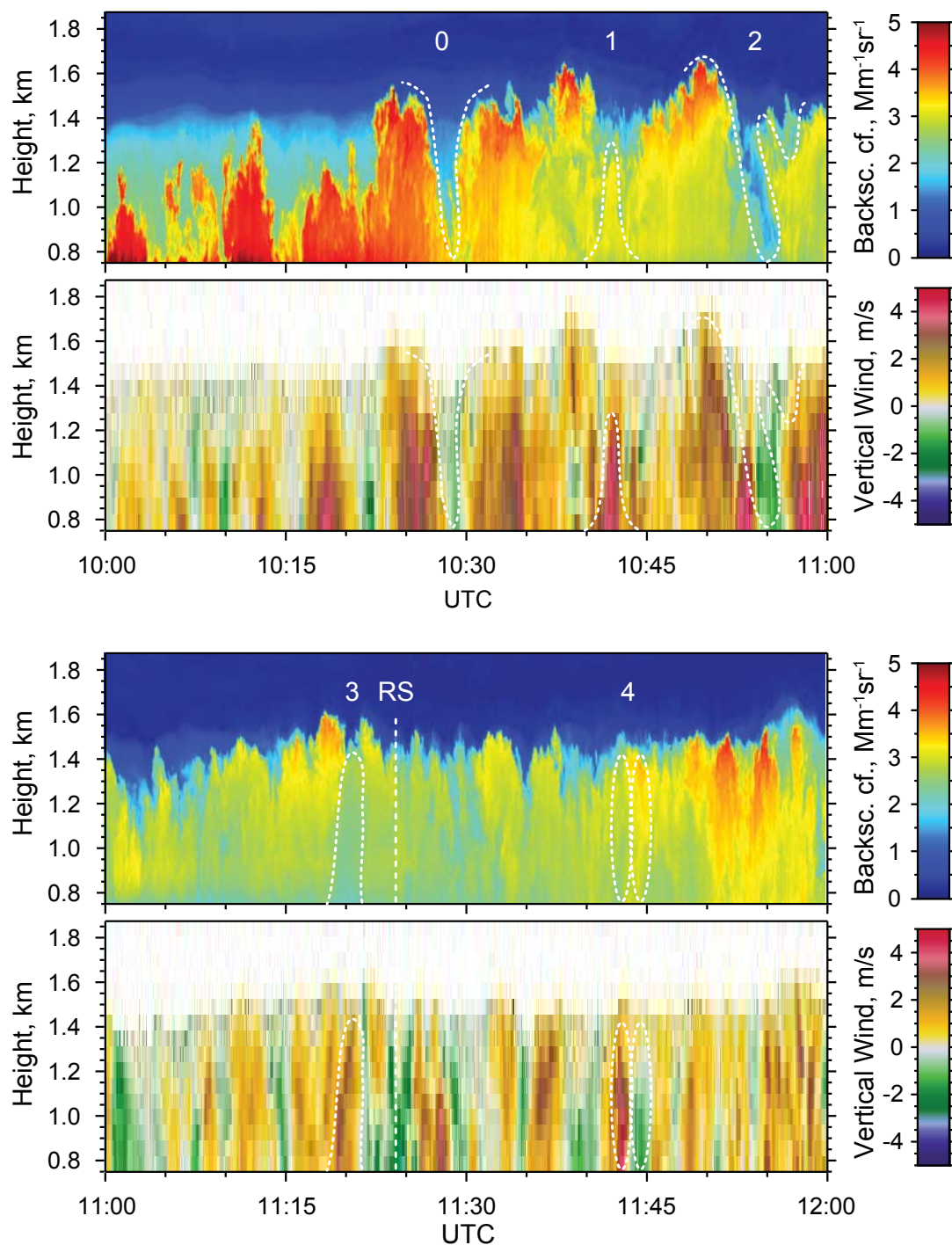


Figure 5.16: Hourly displays of the CBL development at Leipzig between 1000 and 1400 UTC on 26 April 2007 (continued on next page). The top graphs show the profiles of the backscatter coefficient (Klett method), whereas the bottom graphs display the corresponding vertical motion. The vertical resolution is 7.5 m for the Raman lidar and 75 m for the Doppler wind lidar. The time resolution is 5 s for both systems. The marked features are explained in the text. RS—launch of the radiosonde.

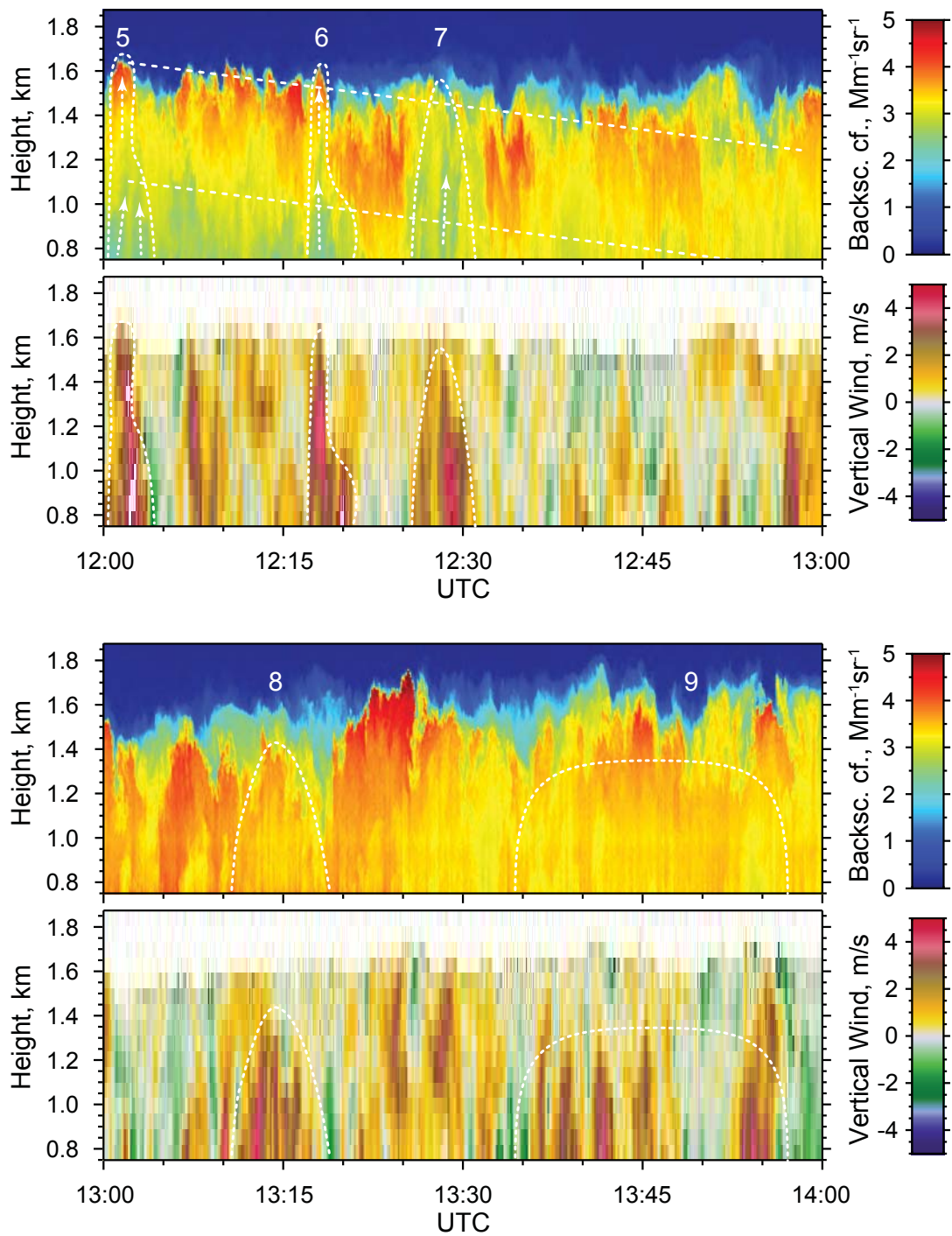


Fig. 5.16: continued.

particles (possibly even from local sources in the southeast) to the upper part of the CBL before the air masses arrived at the lidar site. Thus the CBL would not have been well mixed and what was observed is a *homogenization* process. However, the fact that the anticorrelation between w' and β' was found for several hours (several tens of kilometers) would suggest that stationary flow distortions (orography, buildings, and other surface features) are responsible for this kind of aerosol lifting.

No formation of boundary-layer cumulus clouds could be observed on that day and the relative humidity in the CBL was below 60% during the measurement of the radiosonde. But a slow increase of the relative humidity at the top of the CBL during the afternoon would have been unobserved and cannot be ruled out.

Stratmann et al. (2003) reported events of new particle formation in the entrainment zone during the SATURN experiment ('Strahlung, vertikaler Austausch, Turbulenz und Partikel-Neubildung'; 'radiation, vertical exchange, turbulence and new-particle formation'). They found these events mainly inside the residual layer just before the break-up process of the nocturnal inversion and later also in the entire CBL. These particles grew up and were mixed down during the break-up process of the nocturnal inversion. Also Nilsson et al. (2001) found large downward aerosol number fluxes ($D_p > 14$ nm), which reached maximum levels from noon until the evening, at a boreal forest station (23.3 m above ground) in Hyytiälä in southern Finland during BIOFOR 3 (Biogenic Aerosol Formation Over the Boreal Forest, 1999). They state (Nilsson et al., 2001, p. 455) that 'the large downward flux during the nucleation event is typical for the nucleation days [...], which support the concept of an elevated source, above the canopy and the surface layer, for the new particles.' For this case, local DMPS measurements at the ground showed that formation of new particles occurred from 1200–1300 UTC. These small particles ($D_p < 10$ nm) showed a slow growth until 1600 UTC ($D_p < 100$ nm). But the total volume concentration and the backscatter coefficient at 532 nm at ground level were not affected by this additional amount of small particles. However, the growth rate of the particles in the upper CBL is not known and thus it cannot be ruled out that these additional particles contributed to the observed negative aerosol mass fluxes.

From the evening observations I derived profiles of aerosol backscatter and extinction coefficients. Figure 5.17 shows the analysis of the respective measurement. The profiles of the backscatter coefficients measured with the large telescope were calibrated in the stratosphere where the reference values can be assumed to be very small,

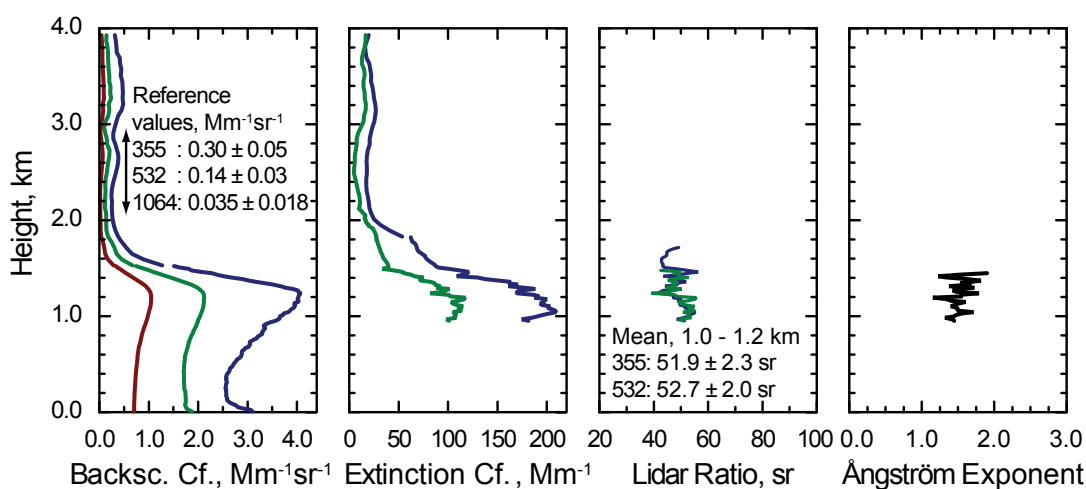


Figure 5.17: Multiwavelength Raman lidar observation of three backscatter and two extinction coefficients on 26 April 2007. The results from the far-range measurement (1935–2109 UTC) are merged at 1.5 km height with the near-range results (2116–2147 UTC). Respective profiles of lidar ratios and the Ångström exponent α are also given.

on the order of $0.01 \text{ Mm}^{-1} \text{ sr}^{-1}$. In the height range between 2 and 3 km the retrieved values from the far-range results were used to calibrate the near-range data. With the known overlap function, the extinction coefficients could be calculated down to 1.5 km from the far-range observations. Below, down to 970 m, values for α^p could be retrieved from the near-range data. The profiles of β^p and α^p were merged at the height of 1.5 km. The lidar ratios were found to be around 52 sr for this case.

The optical data obtained in the upper part of the PBL are summarized in Tab. 5.3. They are in very good agreement with the climatological mean values found by Mattis et al. (2004) for multi-year aerosol lidar observations at Leipzig. The values of the lidar ratio and the Ångström exponent are typical for anthropogenic aerosol particles in central Europe. The lower lidar ratios indicate less absorbing particles than on 12 September 2006 (70–75 sr). It can be assumed that the particle sources in spring are mainly dominated by agricultural or rural activities.

5.2.3 Microphysical parameters of aerosol particles

The mean values of the three backscatter coefficients and the two extinction coefficients from a height interval at the top of the PBL (1.0–1.2 km) were selected for the lidar data inversion. The input data for the inversion as well as the results are sum-

Table 5.3: Input data and inversion results for 26 April 2007. The optical data are the averaged values at the height range from 1.0–1.2 km. For the DMPS data only particle diameters >160 nm were considered. The M_d/β_{532}^p factor was derived with a mean particle density of 1.6 g cm^{-3} .

Inversion input data	355 nm	532 nm	1064 nm
Backscatter coef., $\text{Mm}^{-1} \text{sr}^{-1}$	3.87 ± 0.39	2.08 ± 0.21	1.03 ± 0.20
Extinction coef., Mm^{-1}	200.7 ± 20.0	109.6 ± 11.0	
Lidar ratio, sr	51.9 ± 7.3	52.7 ± 7.4	
Ångström exponent \mathring{a} (355, 532 nm)	1.5 ± 0.2		
Microphysical parameters	Lidar	DMPS 12–18 UTC	DMPS 18–24 UTC
Effective radius, nm	180 ± 40	144 ± 13	145 ± 17
Number concentration, cm^{-3}	1300 ± 280	2329 ± 174	2109 ± 176
Surface-area concentration, $\mu\text{m}^2 \text{cm}^{-3}$	300 ± 65	424 ± 35	386 ± 39
Volume concentration, $\mu\text{m}^3 \text{cm}^{-3}$	18 ± 8	20.4 ± 1.8	18.6 ± 2.1
Mass-to-backscatter ratio			
M_d/β_{532}^p , $\mu\text{g m}^{-3} \text{Mm sr}$	13.8 ± 6.1		

marized in Tab. 5.3. The results from the inversion are in good agreement with the surface-based observation with DMPS. As before, particles with a diameter smaller than 160 nm were neglected from the DMPS data for comparison purposes. The truncated results of the DMPS data are 87%, 68%, and 10% of the volume, the surface-area, and the number concentration, respectively, compared to the total size distributions. The standard deviations from the single DMPS scans within the two time intervals 12–18 and 18–24 UTC are also given.

Figure 5.18 shows the comparison of the derived size distribution of the volume concentration from the inversion and averaged results from IFT’s *in situ* DMPS observations for 26 April 2007. Good agreement of the derived accumulation mode with both methods applied at the PBL top and at the ground, respectively, was found. Hence I used the lidar derived volume concentration of $18 \pm 8 \mu\text{m}^3 \text{cm}^{-3}$ for the further treatment of the aerosol mass flux. With a particle density of 1.6 g cm^{-3} a backscatter-to-mass conversion factor of $13.8 \pm 6.1 \mu\text{g m}^{-3} \text{Mm sr}$ was derived from the nighttime measurements of 26 April 2007.

The mean Ångström exponent \mathring{a} which was derived for the height level 1.0–1.2 km was found to be 1.5 ± 0.2 (see Fig. 5.17). In contrast to the prior case, during 2007

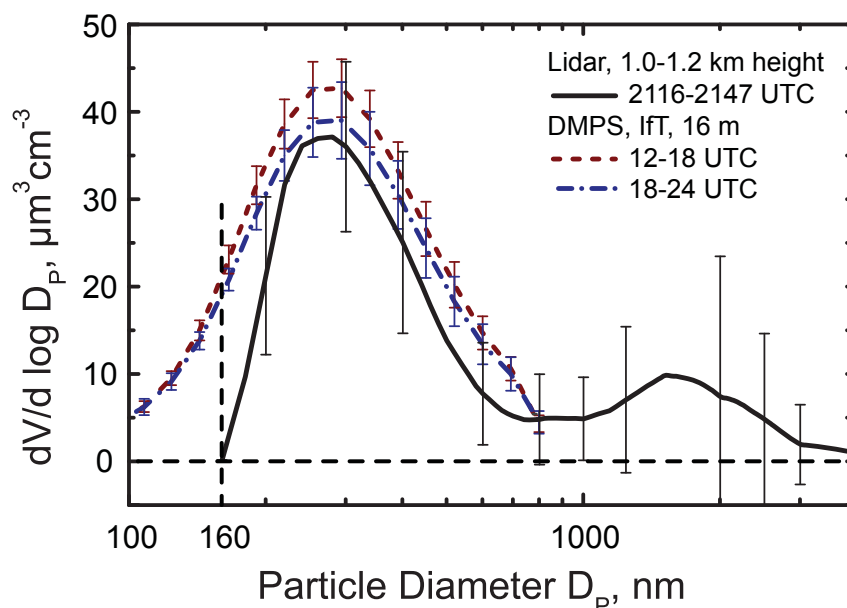


Figure 5.18: Size distributions of the particle volume concentration derived from the lidar data and from ground-based DMPS measurements on 26 April 2007.

the AERONET Sun photometer data were available and could be compared to lidar-derived values. Figure 5.19 shows the time series of the aerosol optical depth for the wavelengths 340, 500, and 1020 nm, which are close to the lidar wavelengths. In the morning hours until 0830 UTC the values remain rather constant at about 0.17 for 500 nm. At around 1100–1200 UTC an increase of about 50% is observed. This increase coincides with the enhanced aerosol backscatter coefficients at the top of the CBL (cf. Fig. 5.16).

The AERONET-derived Ångström exponents between 380–500 nm were found to be 1.4–1.6. These values remain constant during the entire day, especially during the period of increased values of the optical depth. They also compare well with the lidar-derived value from the nighttime measurement. From this finding it can be assumed—once again—that the aerosol composition in the PBL did not vary significantly during the entire day. Therefore, the microphysical particle properties, which were derived from the nighttime measurements for the conversion of $\overline{w'\beta'}$ to aerosol mass fluxes with Eq. (3.19), can be used.

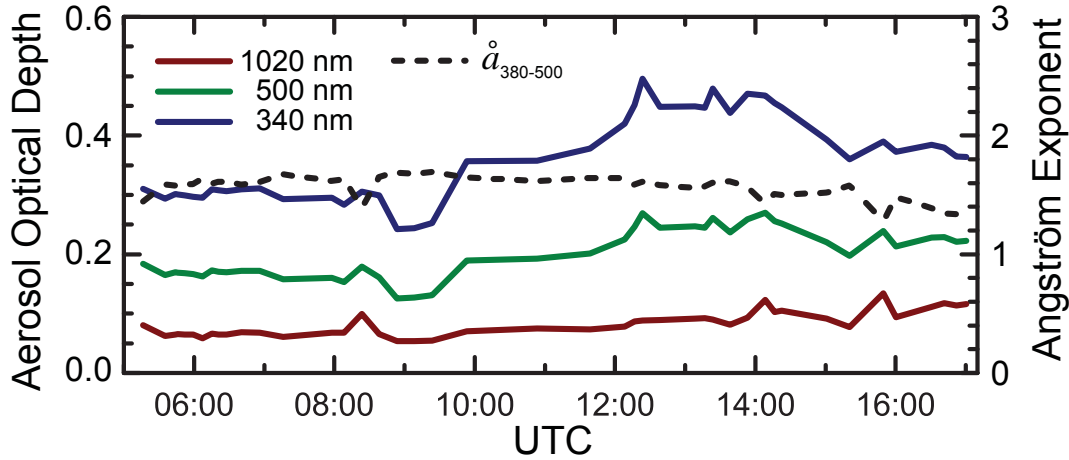


Figure 5.19: Time series of aerosol optical depth and Angström exponent measured with IFT's AERONET Sun photometer on 26 April 2007.

5.2.4 Spectral analysis

In Fig. 5.20 the variance spectra of the backscatter-coefficient and vertical-wind fluctuations at a height of 975 m for five time intervals of 1.5 h each between 0930 and 1700 UTC are shown. The top axes have been derived with a wind speed of 5 m s^{-1} . The spectra show that the inertial subrange ($-5/3$ rd slope) is covered by the measurement and thus the sampling rate is fast enough for flux calculations. In the course of time (0930–1530 UTC), the mixing of air parcels with low and with high particle concentrations, respectively, evolved and became more complete. This is indicated by the reduced fluctuations β' and thus the decrease of the variance spectrum S_{β} . At the same time the variance spectra of the vertical wind remain constant.

Additionally, the cospectra of the respective time series are shown. From 0930–1100 UTC an upward flux can be observed within a frequency range of 10^{-2} – 10^{-3} Hz. This corresponds to eddy sizes of 400–5000 m. The largest particle flux components stem from horizontal eddy dimensions of 2.1 km. Thus the dominant eddies are deformed by a factor of 1.5 in the horizontal direction, because the CBL height for this time interval is about 1.4 km.

Later during the day, we see—as already discussed in the context of Fig. 5.16—that a downward flux is present in this height level. The transporting eddy sizes are 500–4000 m. The strongest peak for the time interval 1100–1230 UTC is found at 3 km. It remains unclear whether this length corresponds to heavily deformed eddies (factor

2) or is caused by the ordered structure of turbulence in the CBL and large-scale features which are often found in atmospheric flows. In addition, we find that 90-min averaging intervals for the flux calculations are reasonable for the atmospheric situation because the cospectra approach zero values at both ends of the frequency range.

5.2.5 Vertical profiles of aerosol mass flux

In addition to the spectral verification, the appropriate averaging length for flux observations was derived by several flux calculations with different lengths (45, 60, 75, 90, 105 min). At a certain length T of the averaging interval the influence of *flux losses* becomes small (systematic error) and the flux values remain rather constant with changing T . Then the major error source is the (random) sampling error. With this method I also derived a useful averaging length of 90 min.

Hence the profiles of the vertical particle fluxes on 26 April 2007 were derived for intervals of $T = 90$ min and are shown in Fig. 5.21. The abscissa axis was derived from the $\overline{\beta'w'}$ covariances by the factor given in Tab. 5.3. The maximum heights of the flux profiles were defined by the point at which the number of invalid data points in the wind time series, because of weak signals in clean air, reached 1/3 of the total number of data points. The error bars represent the dominant sampling error $\sigma_{F,\text{samp}}$ [see Eq. (3.26) and the discussion in Subsection 5.1.6].

Between 0930 and 1100 UTC the highest flux values were found at the quickly mixing CBL top. These maximum values of $2.5\text{--}3.0 \mu\text{g m}^{-2}\text{s}^{-1}$ remained rather constant in the entrainment zone during the most active convection period between 0930 and 1400 UTC. After 1400 UTC the convection slowed down and the vertical exchange processes settled, resulting in nearly zero flux values from 1530–1700 UTC.

It was found that from 1100–1230 and 1230–1400 UTC the sign of the vertical flux changed at a height of about 1200 m. While upward fluxes were still observed at the CBL top (entrainment zone), there was turbulent downward mixing below because of the higher aerosol content that occurred in the upper CBL at that time. This downward flux of about $-(1.5\text{--}1.0) \mu\text{g m}^{-2}\text{s}^{-1}$ almost reached half the magnitude of the upward entrainment flux.

From 1400–1530 UTC the entrainment at the top of the PBL decreased. However, the downward mixing was still ongoing. The respective flux profile is not constant with height. Moreover, the downward mixing was more efficient for lower heights.

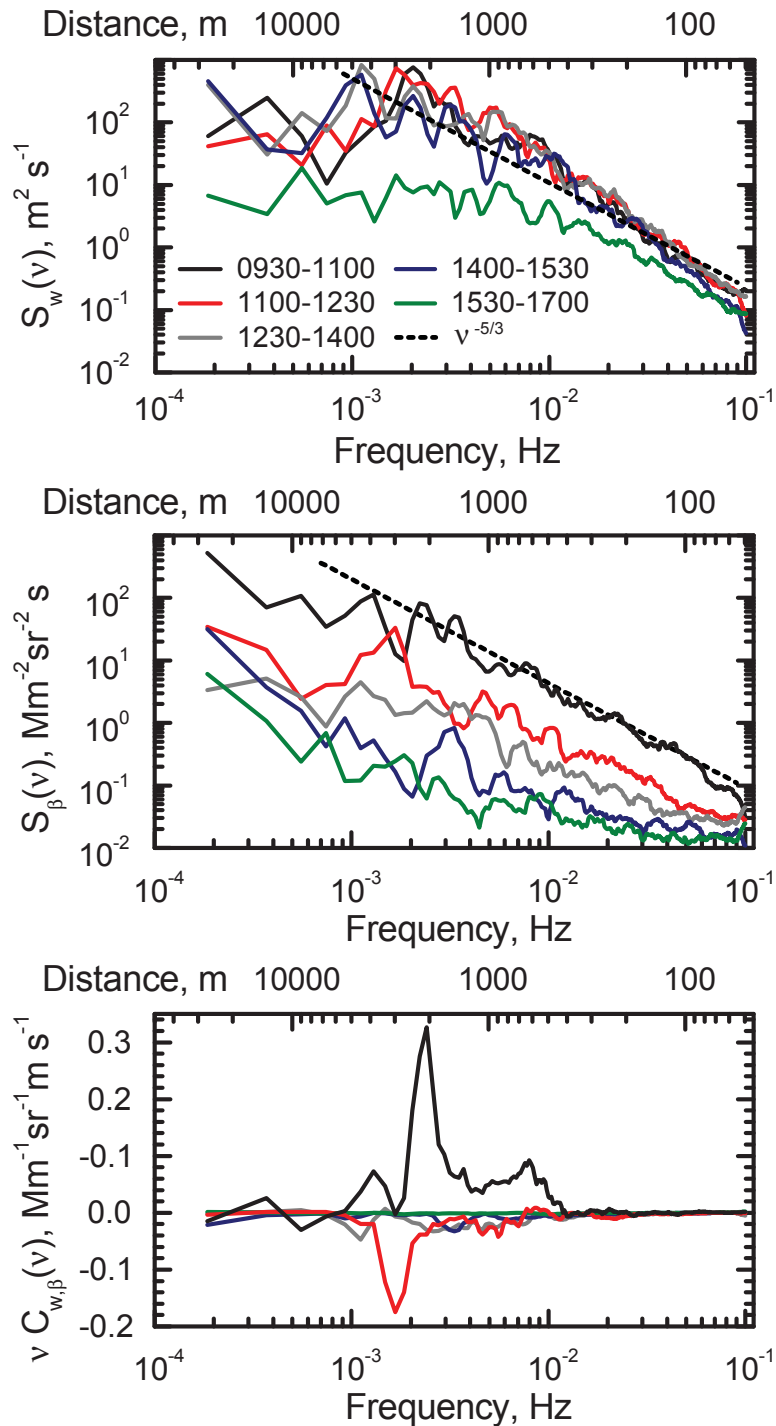


Figure 5.20: Top and middle: power spectral density functions of the vertical wind speed and the backscatter coefficient at a height of 975 m for five time intervals between 0930–1700 UTC on 26 April 2007. The $v^{-5/3}$ slope for the inertial sub-range of turbulence is shown. Bottom: cospectrum of the vertical-wind and particle-backscatter fluctuations for the same height and time intervals. The top axes have been converted with an estimated wind speed of 5 m s^{-1} .

This can be explained by the suppressed convection because of the decreased incoming solar radiation in the afternoon. In this context the vertical extent of the eddy dimensions decreased (cf. Fig. 5.15). Hence the absolute aerosol transport by convective turbulence was greater at lower altitudes in the late afternoon. Between 1530 and 1700 UTC the convection slowed down and therefore turbulent particle fluxes approached values close to zero.

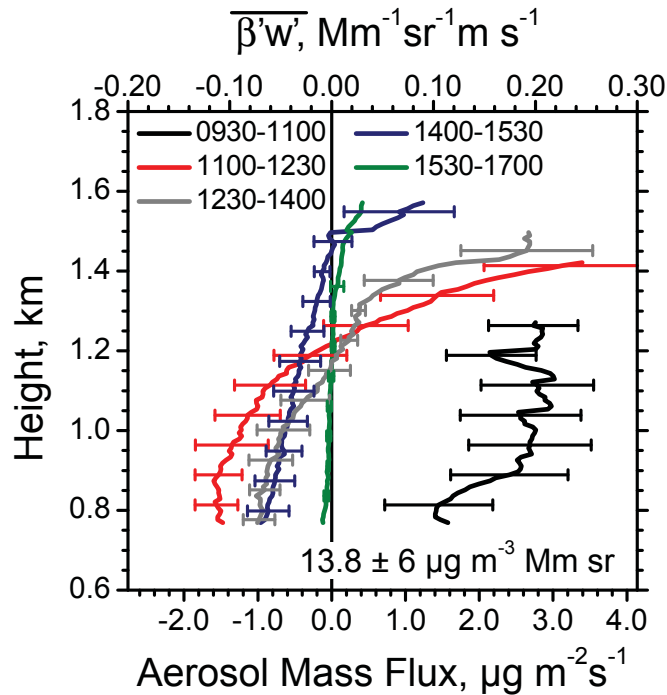


Figure 5.21: Aerosol mass flux profiles for 90-min intervals (c.f. Fig. 5.15) from 0930–1700 UTC on 26 April 2008. The error bars indicate the sampling error.

5.3 Further observations of dry CBL

This section presents five further observations of dry CBL which were performed during the intensive measurement period in 2006. Three days in spring (5 and 11 May 2006 and 26 April 2007) and four days in summer (3 July and 11–13 September 2006) are summarized, including the two case studies already presented before. Certainly this amount of data is not enough for a general statistics of the vertical particle flux within unstable boundary layers. Instead, the vertical particle flux profiles are compared to the prior cases of 12 September 2006 and 26 April 2007.

5.3.1 Synoptic situations

The days were selected because of dry conditions, i.e., the maximum relative humidity throughout the CBL was below 60%. No boundary-layer clouds were observed during these periods. As a consequence, the cases are limited to incoming flow from north-northeasterly to south-southeasterly directions in Central Europe. The region of Leipzig was always influenced by high-pressure systems at the time of the measurements.

The mean horizontal wind, the maximum surface temperature, and the maximum relative humidity within the CBL are summarized for each day in Tab. 5.4. The respective profiles from RS80 radiosoundings are found in the summary plots of these days in Fig. 5.22 to 5.26 (for 12 September 2006 and 26 April 2007 see Fig. 5.3 and 5.14). On 5 and 11 May 2006 no radiosoundings were performed at Leipzig. Hence GDAS reanalysis data for Leipzig are given. The horizontal wind speed and direction were taken from these model data for all cases.

The maximum horizontal wind speed within the CBL of about 10 ms^{-1} from southeasterly directions was observed on 5 May 2006. Thus the generation of turbulence by mechanical (wind shear) processes was highest for this day compared to all observed cases. In contrast, on 11 May the wind speed was $1\text{--}2 \text{ ms}^{-1}$ within the CBL and the turbulence was generated by convection almost exclusively. On the other observed days the horizontal wind speed was between 2 and 8 ms^{-1} .

5.3.2 Lidar measurements

The particle backscatter coefficients at 532 nm and vertical wind speeds from the measurements with the Raman lidar and the Doppler lidar, respectively, are shown at the top of Fig. 5.22 to 5.26. The measurements in May 2006 were done with a temporal resolution of 10 s. Starting from July 2006 all measurements were performed with 5 s time resolution. The majority of measurements with the Raman lidar were taken with the near-range telescope for good coverage of the CBL. From the presented cases only on 3 July 2006 in the afternoon and on 26 April 2007 the far-range telescope was used. Due to thermal stress in the structure of the far-range telescope an instability of the overlap function at the time of highest Sun elevation and maximum solar radiation was observed on 3 July 2006. Therefore, the respective time-height

range was rejected for the data analysis.

The maximum height of the CBL and the time of the convective period was estimated from the Raman lidar measurements and is given in Tab. 5.4. The CBL height was defined as the height where β_{532}^p dropped to 50% of its value within the mixed CBL.

A maximum extent of the CBL of 2.3 km was observed on 5 May 2006 in the late afternoon. From the Raman lidar plot we see a CBL growth which is proportional to the square root of time. This is in agreement with mechanically induced turbulence in a dry CBL (e.g., Stevens, 2007). The particle backscatter coefficient in the CBL was of the order of $2.8 \text{ Mm}^{-1} \text{ sr}^{-1}$ and thus higher than on average. During the dry period in the beginning of May 2006, a large number of fires in eastern Europe was observed by MODIS (Moderate Resolution Imaging Spectroradiometer) from space. A large smoke plume was present over Poland, Belarus, Ukraine, and western Russia. The maximum AOD in Minsk, Belarus, reported by AERONET was about 1.4 and 0.9 at 500 nm on 4 and 5 May, respectively. The Ångström exponent was found to be 1.7–1.8, which is typical for small particles that originated from biomass burning. For Belsk, Poland, the maximum AOD at 500 nm and the Ångström exponent were found to be 1.2 and 1.8, respectively, on 5 May. Leipzig was on the western edge of this smoke plume. The optical depth at 500 nm was found to be 0.3–0.4 from MODIS and from the nearest AERONET measurements at Mainz and Hamburg.

In the late morning of 11 May 2006, until 1040 UTC, a shallow CBL with a height of 700 m was present. Above that, a decoupled aerosol layer was found from 900–1700 m height. Certainly, this was the residual layer from the CBL of the previous day. However, several updrafts in the CBL excited motion throughout the upper layer. Because of the stable layering above the CBL these vertical motions indicate internal gravity waves which were induced by the convection below (*convection waves*, Stull, 1997, p. 477). Unfortunately, from 1040–1120 UTC the lidar measurement with the analog channel was interrupted. The range-corrected signal at 1064 nm is shown instead. In this 40-min interval the CBL grew about 600 m and reached a height of 1300 m. At this point, the updrafts penetrated the residual-layer base and the lower inversion at 700 m height was *burned off*. Thereupon, the thermals continued to rise up to the second inversion at the top of the residual layer. After 1120 UTC the residual layer was already entrained into the CBL. A similar process occurred again from 1400–1430 UTC when another aerosol layer (>1.8 km height) was mixed into

the CBL. At 1430 UTC remarkably strong updrafts with 4 ms^{-1} vertical wind speed were found at heights up to 2.2 km.

On 3 July 2006 moderate wind speeds were observed. Hence the turbulence was mechanically influenced, too. The function of the square root of time is indicated for the CBL growth rate in Fig. 5.24. But in contrast to 5 May 2006, several strong and isolated convective updrafts of 4 ms^{-1} were observed (0900, 1340, 1410, 1515, and 1630 UTC).

The period from 11–13 September 2006 was characterized by stationary atmospheric conditions (see Subsection 5.1.1). The maximum CBL heights were 1000–1100 m, because of reduced incoming solar radiation in late summer. On 11 September maximum velocities of only 2 ms^{-1} and 1.5 ms^{-1} were observed for updrafts and downdrafts, respectively. On 13 September, a Saharan dust layer was observed in the free troposphere between 1200 and 2500 m. With the additional scatterers above the CBL, profiles of the vertical wind could be observed in the free troposphere, too. Similar to 11 May 2006, convection waves were observed within the dust layer.

Table 5.4: Wind speed (w.s.), wind direction (w.d.), maximum surface temperature (Θ_s^{\max}), relative humidity at the CBL top (r.h.^{max}), maximum CBL height (z_i^{\max}), and time of the convective period (c.p.) for the investigated case studies.

Date	w.s. ms^{-1}	w.d.	Θ_s^{\max} °C	r.h. ^{max} %	z_i^{\max} m	c.p. UTC
05 May 06	8–11 ¹	E–SE ¹	22.2 ³	60 ¹	2300	0700–1600 ⁴
11 May 06	1–2 ¹	N–NE ¹	22.2 ³	55 ¹	1500	0800–1630 ⁴
03 July 06	7–8 ¹	E ¹	28.8 ³	35 ²	1500	0700–1700 ⁴
11 Sep. 06	5–6 ¹	SE ¹	26.3 ³	40 ²	1000	1000–1545 ⁴
12 Sep. 06	4–5 ¹	SE ¹	26.8 ³	40 ²	1100	1000–1630 ⁴
13 Sep. 06	2–3 ¹	SE–S ¹	27.1 ³	40 ²	1100	1000–1615 ⁴
26 Apr. 07	4–5 ¹	E ¹	23.1 ³	55 ²	1650	0800–1530 ⁴

¹ from GDAS reanalysis

² from radiosounding at IfT

³ Leipzig Schkeuditz (<http://www.dwd.de>, download 16 Dec. 2008)

⁴ from the respective Raman-lidar plot

5.3.3 Particle mass concentrations

For some of the additional cases, nighttime measurements were not available and thus the complex determination of the microphysical parameters from multiwavelength lidar data was omitted. Instead, I used the continuous DMPS measurements at IfT for the determination of the particle volume concentrations and therewith of the ratios M_d/β_{532}^p . The prior case studies showed that the volume concentrations of the accumulation mode, which were derived at higher altitudes from lidar and at ground from DMPS measurements, respectively, are in good agreement for a well-mixed CBL, i.e. during and shortly after the convective period of the diurnal cycle. However, it is possible (see 26 April 2007) that different particle concentrations at different heights may have occurred for limited periods of time. Therefore, the averaged DMPS data from the 1200–1800 UTC time period was derived and combined with the average particle backscatter coefficient at 532 nm within the CBL during that time. Table 5.5 shows the results for the different conversion factors. Obviously, for 13 September 2006 the factor is only valid within the CBL and not for the dust layer above.

The maximum particle diameter measured with the DMPS is 800 nm, whereas the backscatter coefficient is sensitive to larger particles, as well. Since larger particles can have a significant contribution to the volume and mass concentration the conversion factors are most likely lower compared to values derived from multiwavelength lidar measurements. This trend—although within the uncertainty range—is indicated for 12 September where the factors are $21.1 \pm 8.9 \mu\text{g m}^{-3} \text{ Mm sr}$ and $13.7 \pm 3.2 \mu\text{g m}^{-3} \text{ Mm sr}$ derived from multiwavelength lidar and DMPS measurements, respectively.

5.3.4 Vertical profiles of the aerosol mass flux

The derived turbulent vertical aerosol flux profiles for the additional observations are shown at the bottom of Fig. 5.22 to 5.26. From the previous studies it was found that 90-min intervals are required for the flux determination in order to minimize the sampling error and to cover the major contributions from different frequency regimes. This interval was maintained for all further observations. During periods of strong CBL growth the maximum height for the derived flux profiles was given by the CBL height at the beginning of this interval, because near-stationary time series

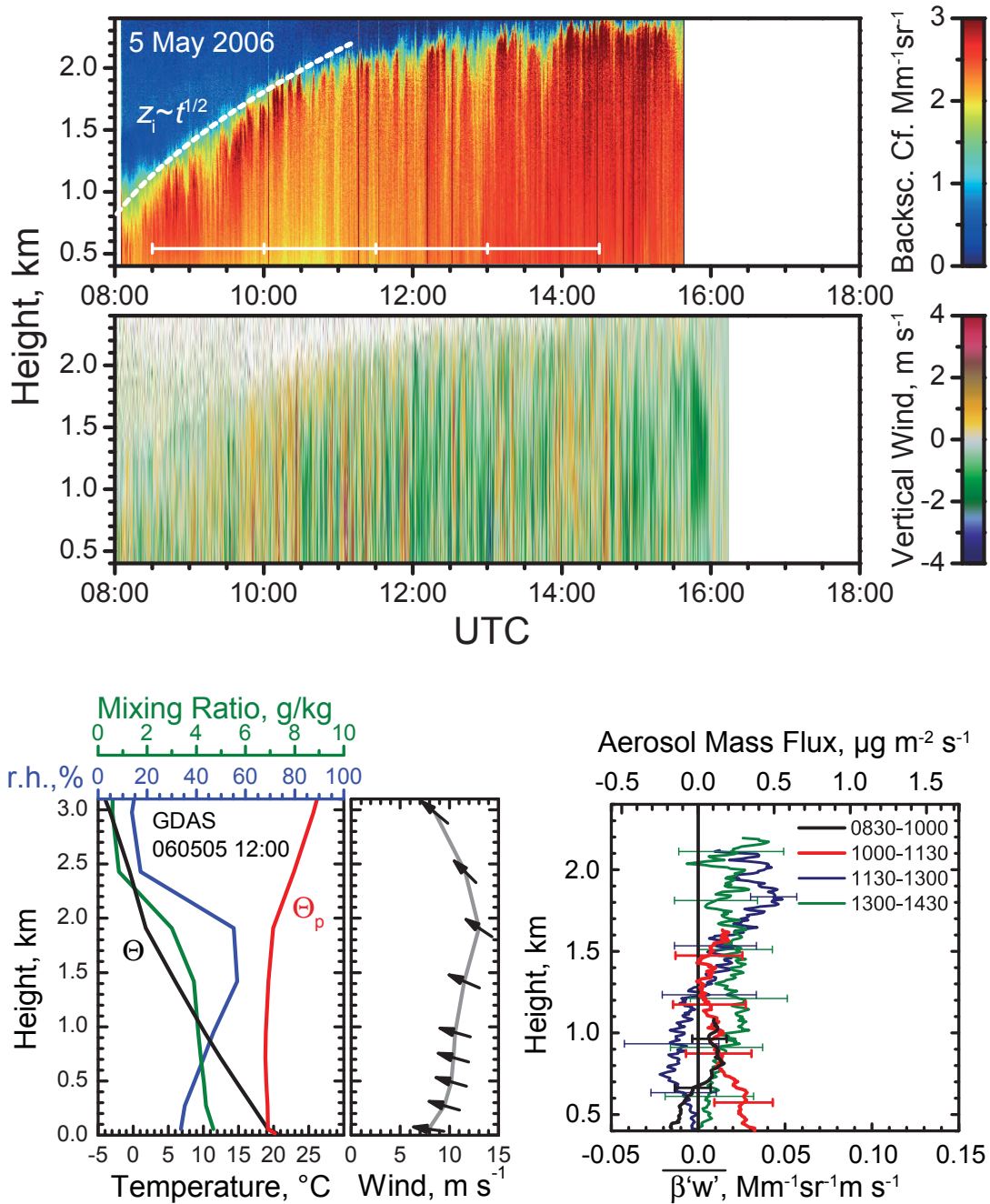


Figure 5.22: 5 May 2006. Top: temporal development of the CBL. The particle backscatter coefficient at 532 nm (Klett method) and the vertical wind speed are shown. The intervals of flux calculation are marked. Bottom: 1200 UTC GDAS model reanalysis for Leipzig (left, <http://www.arl.noaa.gov/READYamet.php>) and derived profiles of the covariances $\beta'w'$ (right). The sampling error is given.

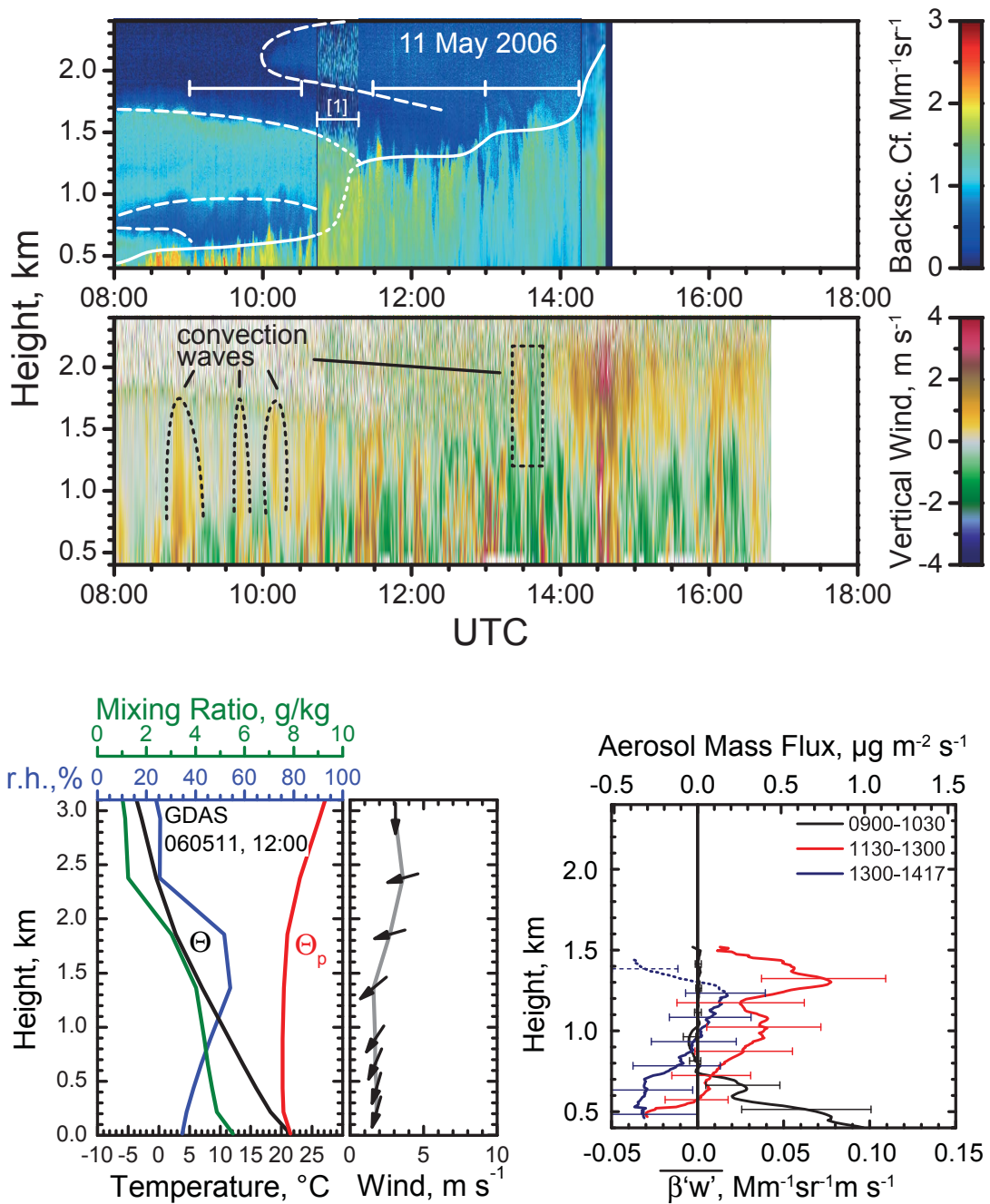


Figure 5.23: Same as Fig. 5.22 but for 11 May 2006. [1]: during the time period 1040–1120 UTC no data from the analog channel are available. Instead, the range-corrected lidar signal from the 1064 nm photon-counting channel is shown.

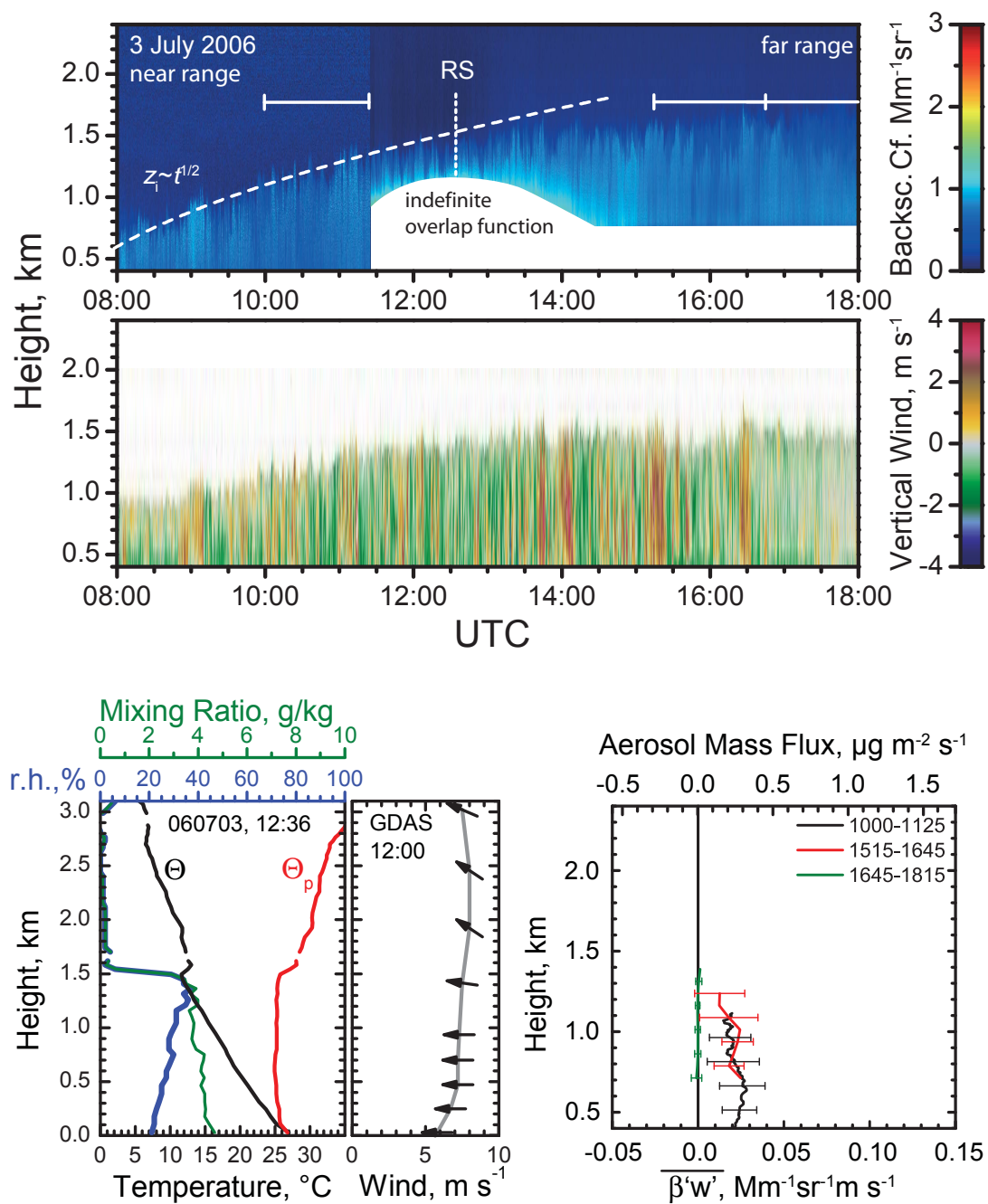


Figure 5.24: Same as Fig. 5.22 but for 3 July 2006 and with radiosounding data (RS) (Θ , Θ_p , r.h. and water-vapor mixing ratio) from measurement at Leipzig.

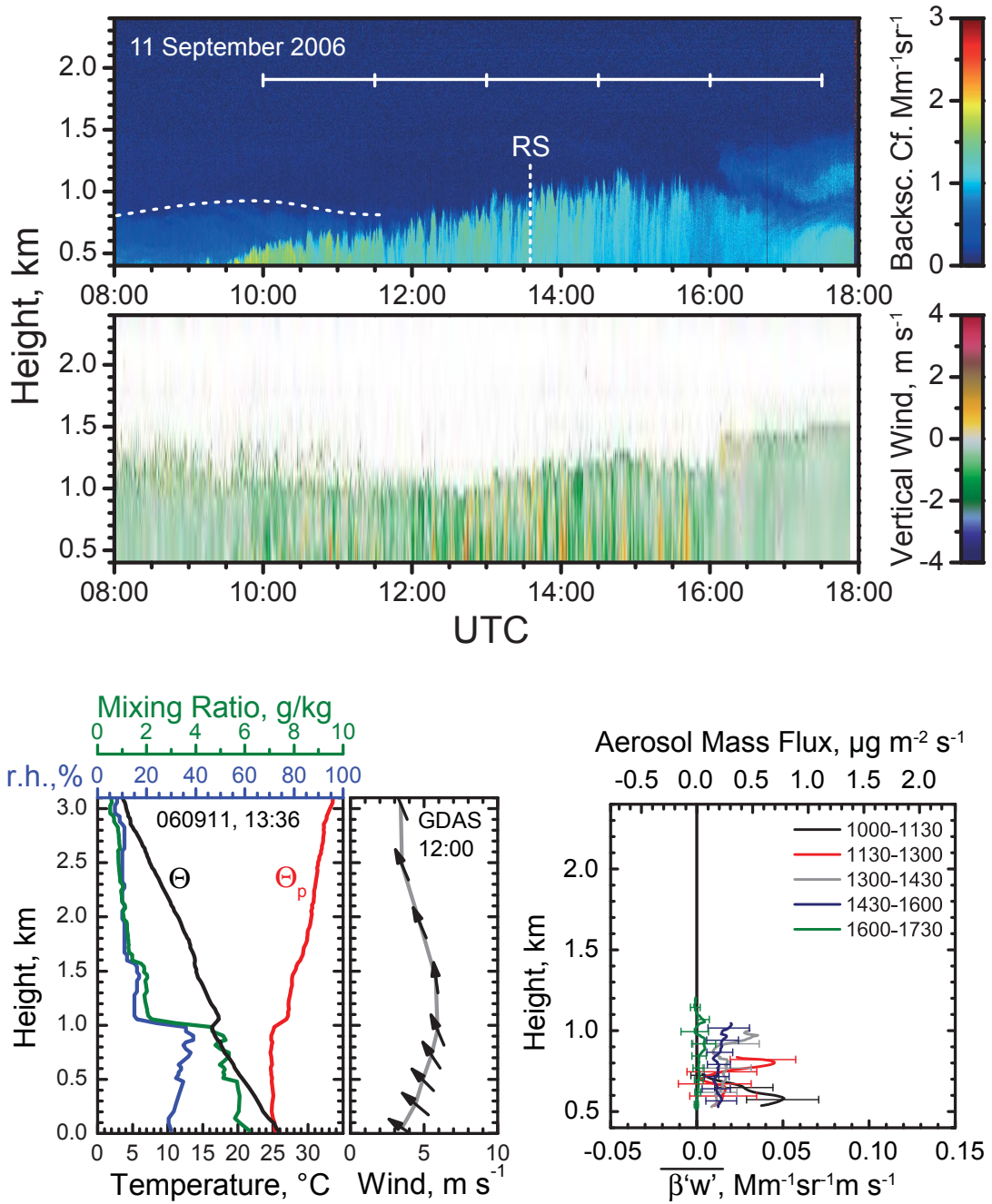


Figure 5.25: Same as Fig. 5.24 but for 11 September 2006.

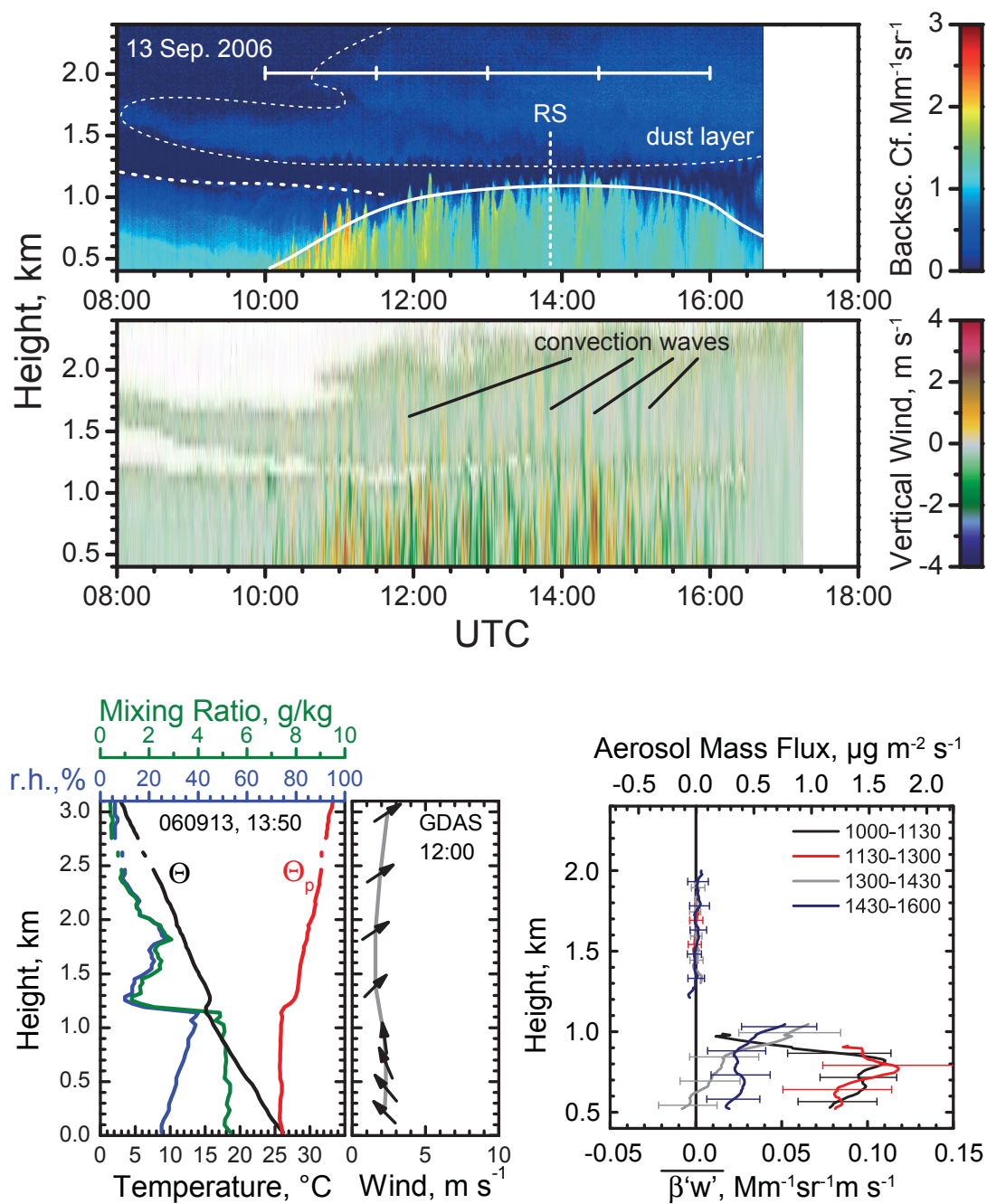


Figure 5.26: Same as Fig. 5.24 but for 13 September 2006.

Table 5.5: Particle volume concentration measured with DMPS ($D_p = 3\text{--}800\text{ nm}$), aerosol mass concentrations ($\rho_p = 1.6\text{ g cm}^{-3}$), mean particle backscatter coefficient in the well-mixed CBL, and derived M_d/β_{532}^p ratio for the time periods 1200–1800 UTC.

Date	V_d $\mu\text{m}^3\text{ cm}^{-3}$	M_d $\mu\text{g m}^{-3}$	β_{532}^p $\text{Mm}^{-1}\text{ sr}^{-1}$	M_d/β_{532}^p $\mu\text{g m}^{-3}\text{ Mm sr}$
05 May 06	20.0 ± 2.4	32.0 ± 7.5	2.8 ± 0.2	11.4 ± 2.8
11 May 06	9.7 ± 1.5	15.5 ± 3.9	1.5 ± 0.2	10.3 ± 3.0
03 July 06	5.0 ± 0.7	8.0 ± 2.0	0.7 ± 0.2	11.4 ± 4.3
11 Sep. 06	8.7 ± 1.0	13.9 ± 3.2	0.9 ± 0.1	15.5 ± 4.0
12 Sep. 06	15.4 ± 1.6	24.6 ± 5.6	1.8 ± 0.1	13.7 ± 3.2
13 Sep. 06	13.0 ± 2.3	20.8 ± 5.6	1.4 ± 0.1	14.9 ± 4.1
26 Apr. 07	23.3 ± 2.3	37.3 ± 8.3	2.2 ± 0.2	16.9 ± 4.1

are required for the eddy correlation method.

The flux profiles which were derived for 5 May 2006 are significantly different from the values of the previous case studies. The values were found to be close to zero, even during the time of largest CBL growth of 460 m h^{-1} between 0830 and 1000 UTC. Because moderate wind speeds were predominant and data with 10 s resolution was used, a spectral analysis (see Subsection 5.1.4 and 5.2.4) has been performed. However, no indications for flux losses were found, i.e., the cospectra of vertical wind and backscatter coefficient approach zero at both frequency ends.

Two explanations for the low flux values are possible. On the one hand, mechanically-induced turbulence, which is more effective for the mixing of aerosol on small scales than buoyantly-generated turbulence, occurred because of the wind shear between the surface and the CBL. Thus scalar fluxes follow the local-closure scheme [see Eq. (2.9)] and higher-order moments in the vertical wind speed, i.e. non-local fluxes, can be neglected. In fact, Fruntke (2009) revealed for 5 May that the skewness of the vertical velocity is smaller and the variance is higher compared to days with lower wind speeds. Subsequently, for a vanishing gradient of the aerosol mass concentration, the turbulent vertical aerosol fluxes become negligible.

On the other hand, aerosol sources at the ground might be negligible compared to the advected biomass-burning aerosol. It can be assumed that the *homogenization* of the mass concentrations within the CBL had already been already completed beforehand, during the time of advection. In such a case, the turbulent motion does not

transport any mass concentration, which is in agreement with the observation.

On 11 May 2006 entrainment fluxes of $0.7 \mu\text{g m}^{-2}\text{s}^{-1}$ for the time intervals from 9000–1030 and 1130–1300 UTC were observed. After the mixing of the residual layer with the CBL was completed around 1100 UTC negative aerosol mass fluxes of $-0.3 \mu\text{g m}^{-2}\text{s}^{-1}$ were found in the lower part of the CBL from 1130–1417 UTC, similar to 26 April 2007. The absolute values of the mass fluxes were lower than for the two case studies because the total aerosol concentration, i.e. the concentration difference of the CBL and of the free troposphere, was significantly lower (see Tab. 5.5). It should be noted that negative flux values were calculated at the top of the CBL above 1300 m for the time interval 1300–1417 UTC. These values are most likely artifacts from a convection wave (dotted box in Fig. 5.23) over the lidar site between 1200 and 2200 m height around 1330 UTC. The alternating vertical wind speed within the stable layer (increasing potential temperature) is an indicator for such gravity waves. Removing these wave-like structures in the vertical wind is possible by applying an appropriate filter on the time series. However, this filtering was not performed because separating the wave motion from the turbulent motion is not a straightforward task. Hence the flux values above 1200 m were treated as non-valid.

On 3 July 2006 two flux profiles could be derived during the convective period and one profile thereafter. During the periods 1000–1125 and 1515–1645 UTC the CBL growth rate was less than 50 m h^{-1} . Nearly constant flux values of $0.3 \mu\text{g m}^{-2}\text{s}^{-1}$ were found between 400 and 1200 m height. The flux profiles derived from the near-range and far-range Raman lidar measurements are in good agreement because the turbulence was close to stationary during the entire period.

On 11 September 2006 the entrainment fluxes were found to be $0.5\text{--}0.7 \mu\text{g m}^{-2}\text{s}^{-1}$ between 1000–1430 UTC. In contrast, on 13 September the entrainment fluxes were $0.9\text{--}1.7 \mu\text{g m}^{-2}\text{s}^{-1}$ during the same time of the day. These differences can be explained by the different aerosol mass concentrations of 13.9 and $20.8 \mu\text{g m}^{-3}$ within the CBL for 11 and 13 September, respectively. It is consistent to the observations on 12 September where the aerosol mass concentration was even higher of the order of $25 \mu\text{g m}^{-3}$ and the entrainment flux reached values of $2\text{--}3 \mu\text{g m}^{-2}\text{s}^{-1}$. Furthermore, it is evident from Fig. 5.26 that the turbulent vertical flux within the dust layer was negligible compared to the fluxes within the CBL on 13 September because of the stable layering of the dust layer.

5.4 Summary of results

In the previous sections seven days of observations of vertical aerosol mass fluxes have been discussed. A summary of all observed flux profiles during the diurnal convective periods is given in Fig. 5.27. All heights were normalized by the actual boundary-layer depth z_i . Additionally, the absolute flux values were scaled by the difference of the aerosol mass concentration within the mixed layer and within the free troposphere. For the presented cases this difference was equal to M_d , even for 13 September 2006 because the dust layer which occurred on that day was separated from the CBL by a layer of almost particle-free air.

Maximum flux values were generally found at the top of the CBL during the active period of convection during each day. The absolute flux maxima of $2.5\text{--}3.0\ \mu\text{g m}^{-2}\text{s}^{-1}$ were found during rapid CBL growth on 12 September 2006 and 26 April 2007. On average, the aerosol mass flux in the entrainment zone was

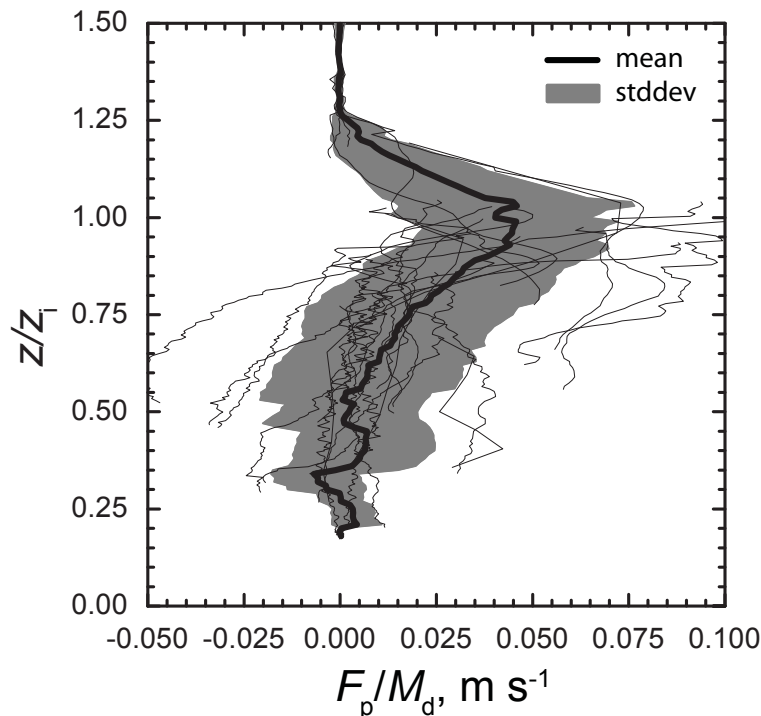


Figure 5.27: Normalized profiles of all obtained aerosol mass flux profiles during the convective measurement periods. Shown are the single profiles (thin lines), the mean profile, and the standard deviation.

$(0.045 \pm 0.025) \text{ ms}^{-1} \times M_d$. It was also found that, on average, the vertical mass flux approaches zero at $0.5 z_i$ and at $1.25 z_i$. However, turbulent downward transport of particle mass was observed, too. The vertical fluxes were of the order of -0.3 and $-1.6 \mu\text{g m}^{-2}\text{s}^{-1}$ on 11 May 2006 and 26 April 2007, respectively, which for the normalized description corresponds to $-0.05 \text{ ms}^{-1} \times M_d$ and $-0.02 \text{ ms}^{-1} \times M_d$, respectively. Observations within the lower height range, i.e. below 400 m or $0.25 z_i$ for some cases, were not possible because of the range restrictions of both lidar systems.

The entrainment flux $F_{p,\text{entr}}$ has been used to compare the observed growth rates of the CBL with the predicted growth rates for stationary, horizontally homogeneous, and source and sink-free conditions. According to the simplified budget formulation from Subsection 5.1.5, Eq. (2.6) at the height z_i can be rewritten to a bulk formulation of the growth rates of the CBL:

$$\frac{\Delta z_i}{\Delta t} = -\frac{\Delta F_p}{\Delta M_d} = \frac{F_{p,\text{entr}}}{M_d}. \quad (5.1)$$

For such an idealized situation the vertical flux and the aerosol mass concentration in the free troposphere need to be negligible compared to the values within the CBL. Then the entrainment flux equals the flux change $-\Delta F_p$ between the CBL and the free troposphere. Additionally, within a given time Δt the aerosol mass concentration M_d within the CBL equals the change ΔM_d .

Figure 5.28 shows a correlation plot for all observed growth rates and for the predicted ones from Eq. (5.1). The actual growth rates were obtained from the differences of the CBL heights z_i at the beginning and at the end of each investigated time interval. Similar to Subsection 5.3.2, each value of z_i was obtained from the height where the particle backscatter coefficient dropped to 50% of its maximum. Temporal averaging of ± 10 min was used in order to calculate β_{532}^p at the times of interest.

A linear fit was performed for which the outlier from 0830–1000 UTC on 5 May was neglected. A correlation coefficient of $r = 0.7$ ($r^2 = 0.5$) was found, i.e., 50% of the variance is explained by the linear fit after Eq. (5.1). The remaining scatter may be caused by horizontal advection, particle sources or sinks, and by measurement errors.

The predicted slope of one was found within the error limit (0.9 ± 0.2). The vertical offset of $-41 \pm 29 \text{ m h}^{-1} = -1.1 \pm 0.8 \text{ cm s}^{-1}$ is distinctly different from zero. It can be explained by a particle sink at the surface or in the mixed layer, most prob-

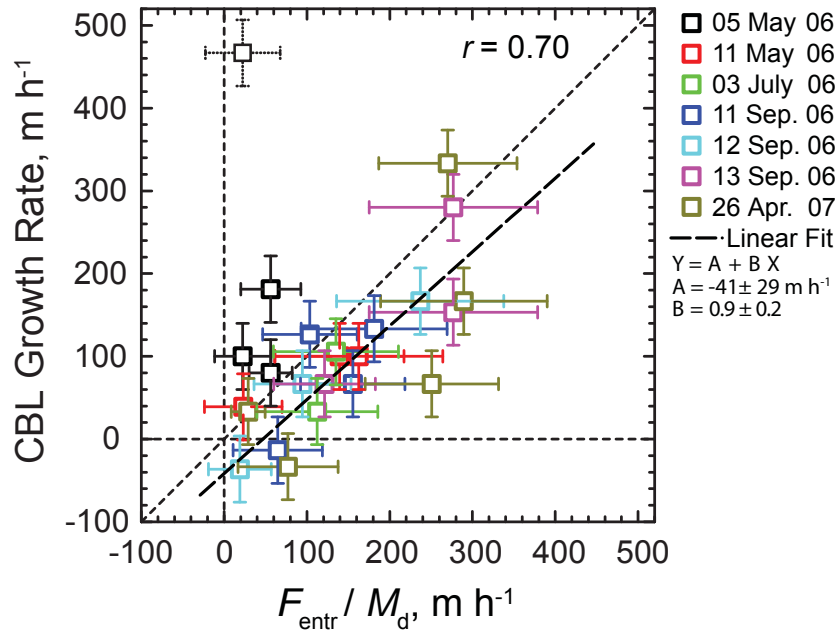


Figure 5.28: Growth rates versus F_{entr}/M_d for the cases of dry-boundary-layer observations. The outlier on 5 May (top left) was removed for the linear fit.

ably by dry deposition of particle mass at the planet's surface. In the cloud-free atmosphere dry deposition is an important loss process for airborne particles (e.g., Sehmel, 1980; Businger, 1986). The deposition velocity is defined by the deposition flux (sedimentation + eddy flux) divided by the airborne concentration. Many factors such as meteorological conditions, surface roughness, particle properties and their size distribution influence the deposition velocity. Unfortunately, no additional ground measurements were available to obtain information on this process for my observations. However, dry deposition velocities of the order of $-(0.2-1.0) \text{ cm s}^{-1}$ for accumulation and coarse mode particles have often been published (e.g., Gallagher et al., 1997; Horváth, 2003; Meyers et al., 2006; Schmidt and Klemm, 2008; Pryor et al., 2008) and agree well with the offset value of $-1.1 \pm 0.8 \text{ cm s}^{-1}$.

5.5 Conclusions

Previous work on vertical exchange of particles was only capable of deriving particle fluxes (Schmidt and Klemm, 2008; Buzorius et al., 2006; Dorsey et al., 2002) with *in situ* techniques. These methods deliver only valuable results for describing local

fluxes from specific sources on relatively small scales. In contrast, the unique method developed in this work is capable of deriving vertical fluxes of particles which are representative of a much larger scale. The remote-sensing technique allows to obtain measurements throughout the entire PBL, up to the entrainment zone. Especially the entrainment flux, which is a determining factor for aerosol transport into the FT, can be studied. Comparing my data to ground-based measurements (e.g., Schmidt and Klemm, 2008), I found that the entrainment process in the upper half of the CBL transports about one order of magnitude more particles with respect to mass than the turbulence at the ground. This strong transport is primarily caused by the intense up-drafts and downdrafts which are found in the Ekman layer during convective periods.

While the *in situ* technique is capable of measuring the number density of particles on time scales of one second, measurements of particle number-size distributions or total volume concentration takes a longer averaging time. For this reason mainly number fluxes have been presented before. In this work it was shown that the turbulent flux of the particle volume can be obtained. The volume flux can then be translated into a mass flux with an assumption of the *volume-mean* particle density.

Lidar is sensitive to optically active particles with radii larger than 50–80 nm, only, which excludes the nucleation- and Aitken-mode particles from the observations. However, the accumulation- and coarse-mode particles significantly contain most of the aerosol volume and mass. Additionally, lidar helps to determine the ambient aerosol mass which is not necessarily a conservative quantity. More sophisticated treatment is required especially if hygroscopic growth plays a role. For this reason, I restricted the application of the presented method for flux measurements with lidar, as a first step, to dry CBL developments.

The eddy-correlation method was found to work well for convective situations. Because the large eddies contribute mostly to the turbulent transport, I have found that the temporal resolution of several seconds of the lidar systems is high enough to cover the major part of the flux spectrum. Of course, this finding is in contrast to ground measurements where small scale turbulence caused by mechanical processes is the primary factor for the vertical exchange. Therefore, this method is limited to measurements above the surface layer.

The eddy-correlation method itself has its downsides, too. Gravity waves, roll vorticities, and strong isolated thermals can have significant influence on the derived result, because the assumption of stationarity of the time series is violated. Therefore,

it was a manual task to check the applicability of the method to each single time series.

Several error sources were investigated. I have found the sampling error to be the major error source for the measurements from a fixed-point ground-based flux measurements. For certain situations this error can reach values of up to 90% even for averaging intervals of 90 min.

It has been shown that the microphysical parameters which were obtained by optical and *in situ* methods at IfT are consistent. However, this finding cannot be generalized, especially if the inversion algorithm is applied several hours after the flux measurement. Hence the second major source of errors was found to be the conversion of optical to microphysical parameters by inversion. Uncertainties of the absolute values of the aerosol mass flux of up to 50% have to be considered here. Even though the investigated scenarios show very good agreement with *in situ* methods it must be kept in mind that further developments on multiwavelength lidar systems (e.g., daytime capabilities) and on the inversion scheme are needed to minimize these errors (Müller, 2008, personal communication). Thus both methods (*in situ* and lidar) should be operated simultaneously in future to get a direct link between the optical and microphysical parameters.

I found the instrumental (noise) errors of the measured time series of particle backscatter and wind to be almost negligible against the two uncertainties discussed above. They are on the order of 5%. In contrast to earlier remote sensing measurements of turbulent fluxes that have been done by Senff et al. (1994), Wulfmeyer (1999) and Giez (1996), the random error was dramatically reduced by use of the appropriate remote sensing technique. While the former two publications have revealed limitations on the determination of vertical wind by the Radar-RASS technique, the latter work shows significant noise contribution from the high-resolution water-vapor measurements from DIAL.

6 Summary and outlook

This work focussed on the derivation of turbulent particle fluxes and thus the investigation of vertical exchange by large eddies in the convective boundary layer (CBL). I combined synchronous measurements with the coherent Doppler lidar WiLi and the aerosol Raman lidar MARTHA in the suburbs of Leipzig at the Leibniz Institute for Tropospheric Research (IfT).

In a first step, the systems were set up to obtain combined measurements. The data acquisition software of WiLi was redesigned and the system was installed in a container, which was operated close to the Raman lidar. Then MARTHA was equipped with an additional analog channel for high-resolution measurements of the profiles of the particle backscatter coefficient at 532 nm, $\beta_{532}^p(z)$. Additionally, the data acquisition software for this channel was developed which also has a special design for synchronization of both instruments. In this configuration, the wind lidar and the Raman lidar were able to measure profiles of the vertical wind velocity $w(z)$ and of the particle backscatter coefficient $\beta_{532}^p(z)$ with accuracies of $0.05\text{--}0.1\text{ m s}^{-1}$ and $0.05\text{--}0.1\text{ Mm}^{-1}\text{sr}^{-1}$, respectively, within the planetary boundary layer (PBL) and aerosol layers above. The temporal resolution of the measurements was 5 s.

Secondly, a method to determine vertical profiles of turbulent particle mass fluxes exclusively determined from lidar observations was successfully developed and applied. The eddy-correlation technique was used and hence the covariance of the fluctuations $\overline{w'\beta'}$ was determined. Special care was taken in order to select the investigated time periods with respect to error minimization. By use of a lidar data inversion algorithm, the covariances were translated into aerosol mass fluxes. It was confirmed that the microphysical aerosol parameters, especially the mass-to-backscatter ratio were invariant during the observed periods which is an essential assumption for the application of the method.

The data used for this work were obtained during 2006 and 2007. At all, 27 aerosol flux profiles could be derived for seven selected days of measurements. Two of these

observational days were selected for detailed case studies. At first, aerosol mass fluxes within a dry CBL were derived for 12 September 2006. The results from this study are very consistent with the observed PBL growth rates. Maximum vertical fluxes of $2.6 \pm 1.0 \mu\text{g m}^{-2}\text{s}^{-1}$ were found in the entrainment zone between the upper part of the PBL and the free troposphere during the time of strongest convective mixing. Later, when the CBL almost reached its full extent, the maximum fluxes were about $1.2 \pm 0.8 \mu\text{g m}^{-2}\text{s}^{-1}$. The major transport was found to be caused by large eddies of 1.2–2.0 km size which is consistent with the observed CBL height z_i . However, the whole spectrum of transport reached from eddy sizes of 250 m to larger scales of up to 25 km.

For the second case study a maximum entrainment flux of $2.5 \pm 0.9 \mu\text{g m}^{-2}\text{s}^{-1}$ was found after 0930 UTC, which is similar to the maximum flux found in the prior case. Additionally, an interesting situation developed during the day, when an increased ambient aerosol mass was observed at the upper part of the CBL. This aerosol-mass gradient decreased to zero in about 3–4 hours because of the ongoing convective processes. Thus downward fluxes could be observed below heights of 1.2 km. The largest downward flux was about $-1.5 \pm 0.5 \mu\text{g m}^{-2}\text{s}^{-1}$. At the same time, the entrainment flux remained almost constant until 1400 UTC. The involved eddy sizes were about 400 to 5 km.

In the following, the remaining days with dry CBL developments during the measurement period 2006 and 2007 were evaluated and the profiles of the vertical aerosol mass fluxes could be determined. Entrainment fluxes of $(0.045 \pm 0.025) \text{m s}^{-1} \times M_d$ were found on average. The correlation coefficient between the observed growth rates of the CBL and the measured entrainment fluxes was found to be 0.7.

Future plans are that this unique technique will be used to study the vertical aerosol transport in highly polluted regions of the world with special emphasis on Asian megacities. For these studies, usually the Doppler lidar WiLi is operated together with the transportable six-wavelength lidar of the IfT. It is planned to add an additional direct-detection lidar using the wavelength of 532 nm to the WiLi system in order to measure the particle backscatter coefficient with high-resolution from this system, as well. The multiwavelength observations would then be performed by the colocated six-wavelength lidar.

Correlated measurements of (particle) fluxes by ground-based *in situ* or airborne instruments and the introduced lidar method, however, would complement each other

very well. The measured flux profiles showed strong variations for different heights. Therefore, the method of lidar observations of vertical particle fluxes is indispensable when observing aerosol fluxes in the PBL.

With this work I developed a method and began to characterize the comprehensive life cycle of atmospheric aerosol particles within the PBL with special emphasis on vertical transport. The future work includes special characterization of these processes with respect to humidity growth of aerosol. Many open questions still remain on how non-conservative scalars (like the ambient aerosol mass in humid environments) should be treated. Additionally, the process of vertical transport of aerosols into clouds is of high interest.

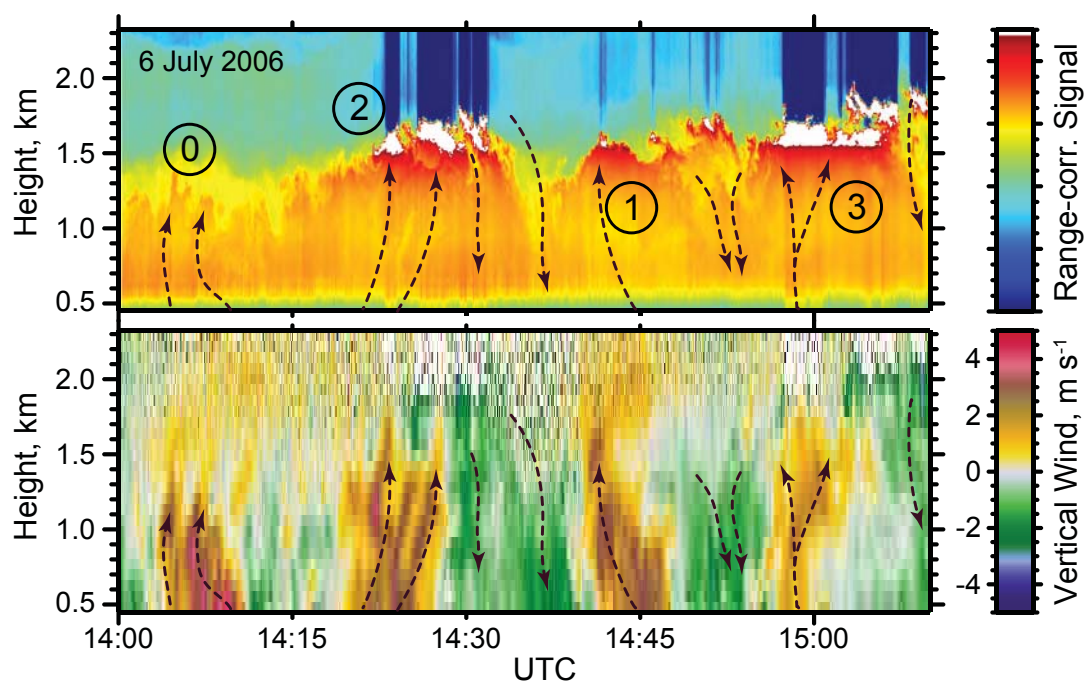


Figure 6.1: Boundary-layer cumulus clouds on 6 July 2006. Top: temporal evolution of the range-corrected signal at 532 nm. Bottom: vertical wind for the same time interval.

An example measurement is given in Fig. 6.1. The temporal development of boundary-layer clouds is shown as they advected over the lidar site on 6 July 2006. The top graph shows the range-corrected signal from the analog channel. Below, the vertical wind speed is given. Four different updraft regions are found between 1400 and 1515 UTC [0–3]. Air parcels in the updraft [0] at 1407 UTC rose with $3\text{--}4\text{ m s}^{-1}$

up to a height of 1300 m. The condensation level was not reached at that time and hygroscopic particle growth is not apparent. In contrast, the updraft [1] at 1645 UTC just reached the condensation level at 1550 m height. The signal drop above indicates the newly formed cloud. Below, from 1400–1550 m particle growth by water uptake increased the lidar signal. At 1425 UTC [2] turbulent boundary-layer clouds were observed. Apparently, they could not be penetrated by the laser beam and no backscattered radiation is detected from above. Shortly after the cloud, a strong downdraft (2 ms^{-1}) transported clean and dry air from the free troposphere downwards into the CBL. The cloud at 1500 UTC [3] is characterized by less vertical motion below (1 ms^{-1}). Additionally, the cloud base is not ragged anymore compared to the cloud [2]. This suggests that the turbulence within the cloud slowed down, already.

This example shows clearly that experiments with combined measurements of temperature and water-vapor concentrations are necessary. These two parameters play an important role for the alteration of aerosol particles. Thus humidity and temperature have to be measured simultaneously if further studies are performed. Nowadays, these data can be determined from lidar measurements with the appropriate systems on the time scale of 30–60 s, which is appropriate for flux measurements, too.

A new development at the IfT offers the possibility to derive microphysical properties of cloud droplets by use of multi-field-of-view lidar measurements (Schmidt, 2009). The combination of my work together with this new approach would allow to study the influence of aerosol transport into clouds on the cloud droplet size and thus the indirect aerosol effect directly and under atmospheric conditions.

Bibliography

- Althausen, D., D. Müller, A. Ansmann, U. Wandinger, H. Hube, E. Clauer, and S. Zörner, 2000: Scanning 6-wavelength 11-channel aerosol lidar. *J. Atmos. Oceanic Technol.*, **17**, 1469–1482.
- Anderson, T. L., R. J. Charlson, S. E. Schwartz, R. Knutti, O. Boucher, H. Rodhe, and J. Heintzenberg, 2003: Climate forcing by aerosols: a hazy picture. *Science*, **300**, 1103–1104.
- Ansmann, A. and D. Müller, 2005: Lidar and atmospheric aerosol particles. In: *Lidar: Range-Resolved Optical Remote Sensing of the Atmosphere*, C. Weitkamp, Ed., Springer, New York, USA, 105–141.
- Ansmann, A., M. Riebesell, U. Wandinger, C. Weitkamp, and W. Michaelis, 1992: Independent measurement of extinction and backscatter profiles in cirrus clouds by using a combined Raman elastic-backscatter lidar. *Appl. Opt.*, **29**, 3266–3272.
- Ansmann, A., M. Tesche, D. Althausen, D. Müller, P. Seifert, V. Freudenthaler, B. Heese, M. Wiegner, G. Pisani, P. Knippertz, and O. Dubovik, 2008: Influence of Saharan dust on cloud glaciation in southern Morocco during the Saharan Mineral Dust Experiment. *J. Geophys. Res.*, **113**, D04210, doi:10.1029/2007JD008785.
- Ansmann, A., F. Wagner, D. Müller, D. Althausen, A. Herber, W. von Hoyningen-Huene, and U. Wandinger, 2002: European pollution outbreaks during ACE 2: optical particle properties inferred from multiwavelength lidar and star-Sun photometry. *J. Geophys. Res.*, **107**, 4259, doi:10.1029/2001JD001109.
- Baars, H., A. Ansmann, R. Engelmann, and D. Althausen, 2008: Continuous monitoring of the boundary-layer top with lidar. *Atmos. Chem. Phys.*, **8**, 7281–7296.
- Baldocchi, D., E. Falge, L. Gu, R. Olson, D. Hollinger, S. Running, P. Anthoni, C. Bernhofer, K. Davis, R. Evans, J. Fuentes, A. Goldstein, G. Katul, B. Law,

- X. Lee, Y. Malhi, T. Meyers, W. Munger, W. Oechel, K. T. Paw, K. Pilegaard, H. P. Schmid, R. Valentini, S. Verma, T. Vesala, K. Wilson, and S. Wofsy, 2001: FLUXNET: a new tool to study the temporal and spatial variability of ecosystem-scale carbon dioxide, water vapor, and energy flux densities. *Bull. Amer. Meteor. Soc.*, **82**, 2415–2434.
- Böckmann, C., 2001: Hybrid regularization method for the ill-posed inversion of multiwavelength lidar data in the retrieval of aerosol size distributions. *Appl. Opt.*, **40**, 1329–1342.
- Bohren, C. F. and D. R. Huffman, 1983: *Absorption and Scattering of Light by Small Particles*. John Wiley & Sons, New York, USA, 530 pp.
- Brewer, W. A. and R. M. Hardesty, 1995: Development of a dual-wavelength CO₂ mini-MOPA Doppler lidar. In: *Coherent Laser Radar*, Optical Society of America, Vol. 19 of *OSA Technical Digest Series*, 293–296.
- Businger, J. A., 1986: Evaluation of the accuracy with which dry deposition can be measured with current micrometeorological techniques. *J. Appl. Meteor.*, **25**, 1100–1124.
- Buzorius, G., J. Kalogiros, and V. Varutbangkul, 2006: Airborne aerosol flux measurements with eddy correlation above the ocean in a coastal environment. *J. Aerosol Sci.*, **37**, 1267–1286.
- Buzorius, G., Ü. Rannik, J. M. Mäkelä, T. Vesala, and M. Kulmala, 1998: Vertical aerosol particle fluxes measured by eddy covariance technique using condensational particle counter. *J. Aerosol Sci.*, **29**, 157–171.
- CCSP, 2009: *Atmospheric Aerosol Properties and Impacts on Climate*. A Report by the U.S. Climate Change Science Program and the Subcommittee on Global Change Research. M. Chin, R. A. Kahn, S. E. Schwartz, Eds., National Aeronautics and Space Administration, Washington, D.C., USA, 149 pp.
- Charlson, R. J., N. C. Ahlquist, and H. Horvath, 1968: On the generality of correlation of atmospheric aerosol mass concentration and light scatter. *Atmos. Env.*, **2**, 455–464.

- Davidson, P. A., 2004: *Turbulence: An Introduction for Scientists and Engineers*. Oxford University Press, Oxford, UK, 657 pp.
- Deardorff, J. W., 1972: Numerical investigation of neutral and unstable planetary boundary layers. *J. Atmos. Sci.*, **29**, 91–115.
- Dillner, A. M., C. Stein, S. M. Larson, and R. Hitzenberger, 2001: Measuring the mass extinction efficiency of elemental carbon in rural aerosol. *Aerosol Sci. Technol.*, **35**, 1009–1021.
- Dolman, A. J., J. Noilhan, P. Durand, C. Sarrat, A. Brut, B. Piguet, A. Butet, N. Jarosz, Y. Brunet, D. Loustau, E. Lamaud, L. Tolk, R. Ronda, F. Miglietta, B. Gioli, V. Magliulo, M. Esposito, C. Gerbig, S. Körner, P. Glademard, M. Ramonet, P. Ciais, B. Neininger, R. W. A. Hutjes, J. A. Elbers, R. Macatangay, O. Schrems, G. Pérez-Landa, M. J. Sanz, Y. Scholz, G. Facon, E. Ceschia, and P. Beziat, 2006: The CarboEurope regional experiment strategy. *Bull. Amer. Meteor. Soc.*, **87**, 1367–1379.
- Dorsey, J. R., E. Nemitz, M. W. Gallagher, D. Fowler, P. I. Williams, K. N. Bower, and K. M. Beswick, 2002: Direct measurements and parameterisation of aerosol flux, concentration and emission velocity above a city. *Atmos. Environ.*, **36**, 791–800.
- Draxler, R. R. and G. D. Hess, 1998: An overview of the HYSPLIT_4 modeling system for trajectories, dispersion, and deposition. *Aust. Meteor. Mag.*, **47**, 295–308.
- Durand, Y., A. Hélière, J.-L. Bézy, and R. Meynard, 2007: The ESA EarthCARE mission: results of the ATLID instrument pre-developments. In: *Lidar Technologies, Techniques, and Measurements for Atmospheric Remote Sensing III*, N. U. Singh and G. Pappalardo, Eds., Vol. 6750 of *Proc. of the SPIE*, 675015.
- Engelmann, R., 2003: *Entwicklung eines Mini-Ramanlidar und Aufbau einer kombinierten Sende- und Empfangseinheit für ein Doppler-Wind-Lidar*. Diploma Thesis, University of Leipzig, 57 pp., available from http://lidar.tropos.de/en/publikation/publist_dd.html.

- Engelmann, R., U. Wandinger, A. Ansmann, D. Müller, E. Žeromskis, D. Althausen, and B. Wehner, 2008: Lidar observations of the vertical aerosol flux in the planetary boundary layer. *J. Atmos. Oceanic Technol.*, **25**, 1296–1306.
- Fedorovich, E., F. T. M. Nieuwstadt, and R. Kaiser, 2001: Numerical and laboratory study of a horizontally evolving convective boundary layer. Part I: transition regimes and development of the mixed layer. *J. Atmos. Sci.*, **58**, 70–86.
- Fernald, F. G., 1984: Analysis of atmospheric lidar observations: some comments. *Appl. Opt.*, **23**, 652–653.
- Ferrare, R. A., S. H. Melfi, D. N. Whiteman, K. D. Evans, and R. Leifer, 1998: Raman lidar measurements of aerosol extinction and backscattering 1. Methods and comparisons. *J. Geophys. Res.*, **103**, 19663–19672, doi:10.1029/98JD01646.
- Foken, T., 2003: *Angewandte Meteorologie: Mikrometeorologische Methoden*. Springer, Heidelberg, 289 pp.
- Frehlich, R., 2001: Estimation of velocity error for Doppler lidar measurements. *J. Atmos. Oceanic Technol.*, **18**, 1628–1639.
- Frehlich, R., S. M. Hannon, and S. W. Henderson, 1994: Performance of a 2- μm coherent Doppler lidar for wind measurements. *J. Atmos. Oceanic Technol.*, **11**, 1517–1528.
- Frigo, M. and S. G. Johnson, 2005: The design and implementation of FFTW3. *Proc. of the IEEE*, **93**, 216–231.
- Frisch, U., 1995: *Turbulence: The legacy of A. N. Kolmogorov*. Cambridge University Press, Cambridge, UK, 310 pp.
- Fruntke, J., 2009: *Charakterisierung der Grenzschicht anhand von Vertikalwindmessungen mit einem Doppler-Lidar*. Diploma Thesis, University of Leipzig, 136 pp.
- Gallagher, M. W., K. M. Beswick, J. Duyzer, H. Westrate, T. W. Choularton, and P. Hummelshøj, 1997: Measurements of aerosol fluxes to Speulder forest using a micrometeorological technique. *Atmos. Env.*, **31**, 359–373.

- Garratt, J. R., 1992: *The Atmospheric Boundary Layer*. Cambridge University Press, Cambridge, UK, 334 pp.
- Gentry, B. M., H. Chen, and S. X. Li, 2000: Wind measurements with 355-nm molecular Doppler lidar. *Opt. Lett.*, **25**, 1231–1233.
- Giez, A., 1996: *Einsatz eines Wasserdampf-DIALs und eines Heterodyn-Wind-Lidars zur Messung des Vertikalflusses von Wasserdampf in einer konvektiven Grenzschicht (Use of a water-vapor DIAL and a coherent wind lidar to measure the vertical flux of water vapor in a convective boundary layer)*. Ph.D. Thesis, University of Munich, 109 pp., Available from Deutsches Zentrum für Luft- und Raumfahrt e.V., Institut für Physik der Atmosphäre, 82234 Oberpfaffenhofen, Germany.
- Giez, A., G. Ehret, R. L. Schwiesow, K. J. Davies, and D. H. Lenschow, 1999: Water vapor flux measurements from ground-based vertically pointed water vapor differential absorption and Doppler lidars. *J. Atmos. Oceanic Technol.*, **16**, 237–250.
- Graskow, B. R., 2001: *Design and Development of a Fast Aerosol Size Spectrometer*. Ph.D. Thesis, University of Cambridge, Department of Engineering, 178 pp.
- Grund, C. J., R. M. Banta, J. L. George, J. N. Howell, M. J. Post, R. A. Richter, and A. M. Weickmann, 2001: High-resolution Doppler lidar for boundary layer and cloud research. *J. Atmos. Oceanic Technol.*, **18**, 376–393.
- Hadamard, J., 1902: On problems in partial derivatives, and their physical significance. *Princeton University Bulletin*, **13**, 82–88.
- Hänel, G., 1976: The properties of atmospheric aerosol particles as functions of the relative humidity at thermodynamic equilibrium with the surrounding moist air. In: *Advances in Geophysics*, H. E. Landsberg and J. van Mieghem, Eds., Academic Press, Inc., New York, USA, Vol. 19, 73–188.
- Harris, F. J., 1978: On the use of windows for harmonic analysis with the discrete Fourier transform. *Proc. of the IEEE*, **66**, 51–83.
- Heintzenberg, J. and R. J. Charlson, Eds., 2009: *Clouds in the Perturbed Climate System: Their Relationship to Energy Balance, Atmospheric Dynamics, and Precipitation*. Ernst Strüngmann Forum Reports, MIT Press, Cambridge, MA, USA, 576 pp.

- Held, A., 2004: *Turbulenter Austausch, Bildung und Wachstum atmosphärischer Partikel über einem Fichtenwald*. Ph.D. Thesis, University of Münster, 199 pp.
- Helmert, J., 2003: *Determination of characteristic turbulence length scales from large eddy simulation of the convective planetary boundary layer*. Ph.D. Thesis, University of Leipzig, 117 pp.
- Henderson, S., P. Gatt, D. Rees, and R. M. Huffaker, 2005: Wind lidar. In: *Laser Remote Sensing*, T. Fujii and T. Fukuchi, Eds., CRC Press, Boca Raton, FL, USA, 469–722.
- Hinze, J. O., 1975: *Turbulence*. McGraw–Hill, New York, USA, 790 pp.
- Holtslag, A. A. M. and B. A. Boville, 1993: Local versus nonlocal boundary-layer diffusion in a global climate model. *J. Climate*, **6**, 1825–1842.
- Holtslag, A. A. M., E. van Meijgaard, and W. C. de Rooy, 1995: A comparison of boundary layer diffusion schemes in unstable conditions over land. *Bound.-Layer Meteor.*, **76**, 69–95.
- Horváth, L., 2003: Dry deposition velocity of PM_{2.5} ammonium sulfate particles to a Norway spruce forest on the basis of S- and N-balance estimations. *Atmos. Env.*, **37**, 4419–4424.
- Husar, R. B., J. D. Husar, and L. Martin, 2000: Distribution of continental surface aerosol extinction based on visual range data. *Atmos. Env.*, **34**, 5067–5078.
- iLEAPS, 2005: *Science Plan and Implementation Strategy*. IGBP Report 54, IGBP Secretariat, Stockholm, Sweden, 52 pp.
- IPCC, 2007: *Climate Change 2007 - The Physical Science Basis*. Contribution of Working Group I to the Fourth Assessment Report of the Intergovernmental Panel on Climate Change., Cambridge University Press, Cambridge, UK, 1009 pp.
- Jennings, S. and R. Pinnick, 1980: Relationships between visible extinction, absorption and mass concentration of carbonaceous smokes. *Atmos. Env.*, **14**, 1123–1129.

- Kahn, R. A., J. A. Ogren, T. P. Ackerman, J. Bösenberg, R. J. Charlson, D. J. Diner, B. N. Holben, R. T. Menzies, M. A. Miller, and J. H. Seinfeld, 2004: Aerosol data sources and their roles within PARAGON. *Bull. Amer. Meteor. Soc.*, **85**, 1511–1522.
- Kaimal, J. C. and J. J. Finnigan, 1994: *Atmospheric Boundary Layer Flows*. Oxford University Press, Oxford, UK, 289 pp.
- Kaimal, J. C., J. C. Wyngaard, D. A. Haugen, O. R. Coté, Y. Izumi, S. J. Caughey, and C. J. Readings, 1976: Turbulence structure in the convective boundary layer. *J. Atmos. Sci.*, **33**, 2152–2169.
- Khain, A., M. Ovtchinnikov, M. Pinsky, A. Pokrovsky, and H. Krugliak, 2000: Notes on the state-of-the-art numerical modeling of cloud microphysics. *Atmos. Res.*, **55**, 159–224.
- Kiemle, C., A. Brewer, G. Ehret, M. Hardesty, A. Fix, C. Senff, M. Wirth, G. Poberaj, and M. LeMone, 2007: Latent heat flux profiles from collocated airborne water vapor and wind lidars during IHOP_2002. *J. Atmos. Oceanic Technol.*, **24**, 627–639.
- Kinne, S., M. Schulz, C. Textor, S. Guibert, Y. Balkanski, S. E. Bauer, T. Berntsen, T. F. Berglen, O. Boucher, M. Chin, W. Collins, F. Dentener, T. Diehl, R. Easter, J. Feichter, D. Fillmore, S. Ghan, P. Ginoux, S. Gong, A. Grini, J. Hendricks, M. Herzog, L. Horowitz, I. Isaksen, T. Iversen, A. Kirkevåg, S. Kloster, D. Koch, J. E. Kristjansson, M. Krol, A. Lauer, J. F. Lamarque, G. Lesins, X. Liu, U. Lohmann, V. Montanaro, G. Myhre, J. Penner, G. Pitari, S. Reddy, O. Seland, P. Stier, T. Takemura, and X. Tie, 2006: An AeroCom initial assessment - optical properties in aerosol component modules of global models. *Atmos. Chem. Phys.*, **6**, 1815–1834.
- Klett, J. D., 1981: Stable analytical inversion solution for processing lidar returns. *Appl. Opt.*, **20**, 211–220.
- 1985: Lidar inversion with variable backscatter/extinction ratios. *Appl. Opt.*, **24**, 1638–1643.

- Korb, C. L., B. Gentry, and C. Weng, 1992: The edge technique—theory and application to the lidar measurement of atmospheric winds. *Appl. Opt.*, **31**, 4202–4213.
- Kristensen, L., J. Mann, S. Oncley, and J. Wyngaard, 1997: How close is close enough when measuring scalar fluxes with displaced sensors? *J. Atmos. Oceanic Technol.*, **14**, 814–821.
- Law, B., 2005: Carbon dynamics in response to climate and disturbance: Recent progress from multi-scale measurements and modeling in AmeriFlux. In: *Plant Responses to Air Pollution and Global Change*, K. Omasa, I. Nouchi, and L. J. De Kok, Eds., Springer, Japan, 205–213.
- Law, D. C. and W. A. Brewer, 2006: Field programmable gate array processors for direct-detection and coherent-detection LIDAR applications. In: *Proceedings of the 7th International Symposium on Tropospheric Profiling*, 11–17th June, Boulder, CO, USA, Paper 8.21.
- Lee, X. and T. A. Black, 1994: Relating eddy correlation sensible heat flux to horizontal sensor separation in the unstable atmospheric surface layer. *J. Geophys. Res.*, **99**, 18545–18554, doi:10.1029/94JD00942.
- Lenschow, D., J. Mann, and L. Kristensen, 1993: How long is long enough when measuring fluxes and other turbulent statistics? Technical Report NCAR/TN-389+STR, NCAR, available from: <http://www.library.ucar.edu/uhtbin/hyperion-image/DR000200>.
- 1994: How long is long enough when measuring fluxes and other turbulent statistics? *J. Atmos. Oceanic Technol.*, **11**, 661–673.
- Lenschow, D. H., M. Lothon, and S. D. Mayor, 2006: Doppler lidar measurements of vertical velocity spectra, length scales, and coherence in the convective planetary boundary layer. In: *17th Symposium on Boundary Layers and Turbulence*, 21–25 May, San Diego, CA, USA, Paper 1.5, available from http://ams.confex.com/ams/BLTA9FBioA/techprogram/meeting_BLTA9FBioA.htm.
- Lenschow, D. H. and B. Stankov, 1986: Length scales in the convective boundary layer. *J. Atmos. Sci.*, **43**, 1198–1209.

- Linné, H. and J. Bösenberg, 1998: Heterodyne DIAL at high repetition rate: a solution for the data acquisition problem. In: *Nineteenth International Laser Radar Conference*, 6-10 July 1998, Annapolis, MD, USA, U. Singh, S. Ismail, and G. Schwemmer, Eds., National Aeronautics and Space Administration, Langley Research Center, NASA/CP-1998-207671/PT1, Hampton, VA, USA, 759–762.
- Linné, H., J. Bösenberg, and D. Hasselmann, 1999: Realtime spectral analysis of heterodyne DIAL signals at very high repetition rate. In: *10th Coherent Laser Radar Conference*, 28 June–2 July, Mount Hood, OR, USA, 72–75.
- Linné, H., B. Hennemuth, J. Bösenberg, and K. Ertel, 2007: Water vapour flux profiles in the convective boundary layer. *Theor. Appl. Climatol.*, **87**, 201–211.
- Lothon, M., D. Lenschow, and S. Mayor, 2006: Coherence and scale of vertical velocity in the convective boundary layer from a Doppler lidar. *Bound.-Layer Meteor.*, **121**, 521–536.
- Lumley, J. L. and H. A. Panofsky, 1964: *The Structure of Atmospheric Turbulence*. Interscience Monographs and Texts in Physics and Astronomy, John Wiley & Sons Inc, New York, USA, 239 pp.
- MacKinnon, D. J., 1969: The effect of hygroscopic particles on the backscattered power from a laser beam. *J. Atmos. Sci.*, **26**, 500–510.
- Mattis, I., 2002: *Aufbau eines Feuchte-Temperatur-Aerosol-Ramanlidars und Methodenentwicklung zur kombinierten Analyse von Trajektorien und Aerosolprofilen*. Ph.D. Thesis, University of Leipzig, 134 pp.
- Mattis, I., A. Ansmann, D. Althausen, V. Jaenisch, U. Wandinger, D. Müller, Y. Arshinov, S. Bobrovnikov, and I. Serikov, 2002: Relative-humidity profiling in the troposphere with a Raman lidar. *Appl. Opt.*, **41**, 6451–6462.
- Mattis, I., A. Ansmann, D. Müller, U. Wandinger, and D. Althausen, 2004: Multi-year aerosol observations with dual-wavelength Raman lidar in the framework of EARLINET. *J. Geophys. Res.*, **109**, D13203, doi:10.1029/2004JD004600.
- Mattis, I., D. Müller, A. Ansmann, U. Wandinger, J. Preißler, P. Seifert, and M. Tesche, 2008: Ten years of multiwavelength Raman lidar observations of free-

- tropospheric aerosol layers over central Europe: geometrical properties and annual cycle. *J. Geophys. Res.*, **113**, D20202, doi:10.1029/2007JD009636.
- Meyers, T., W. Luke, and J. Meisinger, 2006: Fluxes of ammonia and sulfate over maize using relaxed eddy accumulation. *Agric. Forest Meteorol.*, **136**, 203–213.
- Mie, G., 1908: Beiträge zur Optik trüber Medien, speziell kolloidaler Metallösungen. *Ann. der Physik*, **25**, 337–455.
- Mishchenko, M. I., L. D. Travis, and A. A. Lacis, 2002: *Scattering, Absorption, and Emission of Light by Small Particles*. Cambridge University Press, Cambridge, UK, 445 pp.
- Moeng, C.-H. and J. C. Wyngaard, 1984: Statistics of conservative scalars in the convective boundary layer. *J. Atmos. Sci.*, **41**, 3161–3169.
- Morançais, D., F. Fabre, M. Schillinger, J.-C. Barthès, M. Endemann, A. Culoma, and Y. Durand, 2004: ALADIN: the first European lidar in space. In: *5th International Conference on Space Optics*, B. Warmbein, Ed., Vol. 554 of *ESA Special Publication*, 13–17.
- Müller, D., 2007: *Characterization of Free-Tropospheric Particles With Multiwavelength Raman Lidar: Geometrical, Optical, and Microphysical Properties of Aerosol Pollution From Europe, North Africa, South Asia, and North America*. Habilitation Thesis, University of Leipzig, 208 pp.
- Müller, D., A. Ansmann, I. Mattis, M. Tesche, U. Wandinger, D. Althausen, and G. Pisani, 2007a: Aerosol-type-dependent lidar ratios observed with Raman lidar. *J. Geophys. Res.*, **112**, D16202, doi:10.1029/2006JD008292.
- Müller, D., I. Mattis, A. Ansmann, U. Wandinger, and D. Althausen, 2007b: Raman lidar for monitoring of aerosol pollution in the free troposphere. In: *Advanced Environmental Monitoring*, Y. J. Kim and U. Platt, Eds., Springer, The Netherlands, 155–166.
- Müller, D., U. Wandinger, D. Althausen, and M. Fiebig, 2001: Comprehensive particle characterization from three-wavelength Raman-lidar observations. *Appl. Opt.*, **40**, 4863–4869.

- Müller, D., U. Wandinger, and A. Ansmann, 1999: Microphysical particle parameters from extinction and backscatter lidar data by inversion with regularization: simulation. *Appl. Opt.*, **38**, 2358–2368.
- Nilsson, E. D., Ü. Rannik, M. Kulmala, G. Buzorius, and C. D. O’Dowd, 2001: Effects of continental boundary layer evolution, convection, turbulence and entrainment, on aerosol formation. *Tellus Ser. B*, **53**, 441–461.
- Nuttall, A. H., 1981: Some windows with very good sidelobe behavior. *IEEE Transactions on Acoustics, Speech and Signal Processing*, **29**, 84–91.
- O’Neill, N. T., O. Dubovik, and T. F. Eck, 2001a: Modified Ångström exponent for the characterization of submicrometer aerosols. *Appl. Opt.*, **40**, 2368–2375.
- O’Neill, N. T., B. N. Eck, A. Smirnov, O. Dubovik, and A. Royer, 2001b: Bimodal size distribution influences on the variation of Ångström derivatives in spectral and optical depth space. *J. Geophys. Res.*, **106**, 9787–9806.
- O’Neill, P. L., D. Nicolaides, D. Honnery, and J. Soria, 2004: Autocorrelation functions and the determination of integral length with reference to experimental and numerical data. In: *15th Australasian Fluid Mechanics Conference*, 13–17 December, The University of Sydney, Australia, M. Behnia, W. Lin, and G. D. McBain, Eds., Paper AFMC00064, available from <http://www.aeromech.usyd.edu.au/15afmc/proceedings/index.html>.
- Pruppacher, H. R. and J. D. Klett, 1997: *Microphysics of Clouds and Precipitation*. Kluwer Academic Publishers, Dordrecht, The Netherlands, 954 pp.
- Pryor, S. C., M. Gallagher, H. Sievering, S. E. Larsen, R. J. Barthelmie, F. Birsan, E. Nemitz, J. Rinne, M. Kulmala, T. Grönholm, R. Taipale, and T. Vesala, 2008: A review of measurement and modelling results of particle atmosphere-surface exchange. *Tellus Ser. B*, **60**, 42–75.
- Rew, R. and G. Davis, 1990: NetCDF: an interface for scientific data access. *IEEE Comput. Graph. Appl.*, **10**, 76–82.
- Rhone, P., 2004: *Development of the Data Acquisition and Analysis Systems for a Portable Raman Lidar and a Doppler Wind Li-*

- dar. Diploma Thesis, University of Leipzig, 72 pp., available from http://lidar.tropos.de/en/publikation/publist_dd.html.
- Sasano, Y., E. V. Browell, and S. Ismail, 1985: Error caused by using a constant extinction/backscattering ratio in the lidar solution. *Appl. Opt.*, **24**, 3929–3932.
- Schmidt, A. and O. Klemm, 2008: Direct determination of highly size-resolved turbulent particle fluxes with the disjunct eddy covariance method and a 12-stage electrical low pressure impactor. *Atmos. Chem. Phys.*, **8**, 7405–7417.
- Schmidt, J., 2009: *Aufbau und Test von Mehrfachstredetektionskanälen zur Messung der Wolkenröpfchengröße mit einem Ramanlidar*. Diploma Thesis, University of Leipzig, 68 pp.
- Schwiesow, R. and M. Spowart, 1996: The NCAR airborne infrared lidar system: status and applications. *J. Atmos. Oceanic Technol.*, **13**, 4–15.
- Sehmel, G. A., 1980: Particle and gas dry deposition: a review. *Atmos. Env.*, **14**, 983–1011.
- Seifert, P., R. Engelmann, A. Ansmann, U. Wandinger, I. Mattis, D. Althausen, and J. Fruntke, 2008: Characterization of specular reflections in mixed-phase and ice clouds based on scanning, polarization, and Raman lidar. In: *Reviewed and revised papers presented at the 24th International Laser Radar Conference, 23-27 June, Boulder, CO, USA*, M. Hardesty, S. Mayor, C. Senff, S. Spuler, P. Weibring, S. Tucker, A. Brewer, and B. Morley, Eds., Paper S05O–05.
- Senff, C., J. Bösenberg, and G. Peters, 1994: Measurement of water vapor flux profiles in the convective boundary layer with lidar and radar–RASS. *J. Atmos. Oceanic Technol.*, **11**, 85–93.
- Senff, C., J. Bösenberg, G. Peters, and T. Schaberl, 1996: Remote sensing of turbulent ozone fluxes and the ozone budget in the convective boundary layer with DIAL and radar–RASS: a case study. *Contr. Atmos. Phys.*, **69**, 161–176.
- Shah, S. and D. Cocker III, 2005: A fast scanning mobility particle spectrometer for monitoring transient particle size distributions. *Aerosol Sci. Technol.*, **39**, 519–526.

- Siebert, H., K. Lehmann, M. Wendisch, and R. Shaw, 2006: The helicopter-borne ACTOS for small-scale cloud turbulence observations. In: *12th Conference on Cloud Physics*, 10–14 July, Madison, WI, USA, Paper P2.38, available from <http://ams.confex.com/ams/Madison2006/techprogram/MEETING.HTM>.
- Stevens, B., 2007: On the growth of layers of nonprecipitating cumulus convection. *J. Atmos. Sci.*, **64**, 2916–2931.
- Stratmann, F., H. Siebert, G. Spindler, B. Wehner, D. Althausen, J. Heintzenberg, O. Hellmuth, R. Rinke, U. Schmieder, C. Seidel, T. Tuch, U. Uhrner, A. Wiedensohler, U. Wandinger, M. Wendisch, D. Schell, and A. Stohl, 2003: New-particle formation events in a continental boundary layer: first results from the SATURN experiment. *Atmos. Chem. Phys.*, **3**, 1445–1459.
- Stull, R. B., 1997: *An Introduction to Boundary Layer Meteorology*. Kluwer Academic Publishers, Dordrecht, The Netherlands, 670 pp.
- Swietlicki, E., J. Zhou, O. H. Berg, B. G. Martinsson, G. Frank, S.-I. Cederfelt, U. Dusek, A. Berner, W. Birmili, A. Wiedensohler, B. Yuskiewicz, and K. N. Bower, 1999: A closure study of sub-micrometer aerosol particle hygroscopic behaviour. *Atmos. Res.*, **50**, 205–240.
- Tang, I. N. and H. R. Munkelwitz, 1994: Water activities, densities, and refractive indices of aqueous sulfates and sodium nitrate droplets of atmospheric importance. *J. Geophys. Res.*, **99**, 18801–18808, doi:10.1029/94JD01345.
- Taylor, G. I., 1938: The spectrum of turbulence. *Proc. R. Soc. London, Ser. A*, **164**, 476–490.
- Tennekes, H., 1973: The logarithmic wind profile. *J. Atmos. Sci.*, **30**, 234–238.
- 1978: Turbulent flow in two and three dimensions. *Bull. Amer. Meteor. Soc.*, **59**, 22–28.
- Textor, C., M. Schulz, S. Guibert, S. Kinne, Y. Balkanski, S. Bauer, T. Berntsen, T. Berglen, O. Boucher, M. Chin, F. Dentener, T. Diehl, R. Easter, H. Feichter, D. Fillmore, S. Ghan, P. Ginoux, S. Gong, A. Grini, J. Hendricks, L. Horowitz,

- P. Huang, I. Isaksen, T. Iversen, S. Kloster, D. Koch, A. Kirkevåg, J. E. Kristjansson, M. Krol, A. Lauer, J. F. Lamarque, X. Liu, V. Montanaro, G. Myhre, J. Penner, G. Pitari, S. Reddy, Ø. Seland, P. Stier, T. Takemura, and X. Tie, 2005: Analysis and quantification of the diversities of aerosol life cycles within AeroCom. *Atmos. Chem. Phys.*, **5**, 8331–8420.
- Thomas, L., J. C. Cartwright, and D. P. Wareing, 1990: Lidar observations of the horizontal orientation of ice crystals in cirrus clouds. *Tellus Ser. B*, **42**, 211–216.
- Treviño, G. and E. L. Andreas, 2004: On Reynolds averaging and the zero integral scale constraint. In: *16th Symposium on Boundary Layers and Turbulence*, 9–13 August, Portland, ME, USA, Paper 7.8, available from http://ams.confex.com/ams/BLTAIRSE/techprogram/meeting_BLTAIRSE.htm.
- Van der Hoven, I., 1957: Power spectrum of horizontal wind speed in the frequency range from 0.0007 to 900 cycles per hour. *J. Atmos. Sci.*, **14**, 160–164.
- Van Dingenen, R., F. Raes, J.-P. Putaud, U. Baltensperger, A. Charron, M.-C. Facchini, S. Decesari, S. Fuzzi, R. Gehrig, H.-C. Hansson, R. M. Harrison, C. Hüglin, A. M. Jones, P. Laj, G. Lorbeer, W. Maenhaut, F. Palmgren, X. Querol, S. Rodriguez, J. Schneider, H. ten Brink, P. Tunved, K. Tørseth, B. Wehner, E. Weingartner, A. Wiedensohler, and P. Wåhlin, 2004: A European aerosol phenomenology—1: physical characteristics of particulate matter at kerbside, urban, rural and background sites in Europe. *Atmos. Environ.*, **38**, 2561–2577.
- Van Dop, H. and G. Verver, 2001: Countergradient transport revisited. *J. Atmos. Sci.*, **58**, 2240–2247.
- Veselovskii, I., A. Kolgotin, V. Griaznov, D. Müller, U. Wandinger, and D. N. Whiteman, 2002: Inversion with regularization for the retrieval of tropospheric aerosol parameters from multiwavelength lidar sounding. *Appl. Opt.*, **41**, 3685–3699.
- Wandinger, U., 2005: Raman lidar. In: *Lidar: Range-Resolved Optical Remote Sensing of the Atmosphere*, C. Weitkamp, Ed., Springer, New York, USA, 241–272.
- Wandinger, U. and A. Ansmann, 2002: Experimental determination of the lidar overlap profile with Raman lidar. *Appl. Opt.*, **41**, 511–514.

- Wandinger, U., H. Linné, J. Bösenberg, E. Žeromskis, D. Althausen, and D. Müller, 2004: Turbulent aerosol fluxes determined from combined observations with Doppler wind and Raman aerosol lidar. In: *Reviewed and Revised Papers Presented at the 22nd International Laser Radar Conference (ILRC 2004)*, 12–16 July, Matera, Italy, G. Pappalardo, A. Amodeo, and B. Warmbein, Eds., European Space Agency, Noordwijk, The Netherlands, Vol. SP-561, 743–746.
- Wandinger, U., D. Müller, C. Böckmann, D. Althausen, V. Matthias, J. Bösenberg, V. Weiß, M. Fiebig, M. Wendisch, A. Stohl, and A. Ansmann, 2002: Optical and microphysical characterization of biomass-burning and industrial-pollution aerosols from multiwavelength lidar and aircraft measurements. *J. Geophys. Res.*, **107**, 8125, doi:10.1029/2000JD000202.
- Wang, J., V. F. McNeill, D. R. Collins, and R. C. Flagan, 2002: Fast mixing condensation nucleus counter: application to rapid scanning differential mobility analyzer measurements. *Aerosol Sci. Technol.*, **36**, 678–689.
- Werner, C., 2005: Doppler wind lidar. In: *Lidar: Range-Resolved Optical Remote Sensing of the Atmosphere*, C. Weitkamp, Ed., Springer, New York, USA, 325–354.
- Wexler, A. S. and J. H. Seinfeld, 1991: Second-generation inorganic aerosol model. *Atmos. Environ. Part A*, **25**, 2731–2748.
- Whiteman, D. N., 2003a: Examination of the traditional Raman lidar technique. I. Evaluating the temperature-dependent lidar equations. *Appl. Opt.*, **42**, 2571–2592.
- 2003b: Examination of the traditional Raman lidar technique. II. Evaluating the ratios for water vapor and aerosols. *Appl. Opt.*, **42**, 2593–2608.
- Wulfmeyer, V., 1999: Investigation of turbulent processes in the lower troposphere with water vapor DIAL and Radar–RASS. *J. Atmos. Sci.*, **56**, 1055–1076.
- Wulfmeyer, V. and G. Feingold, 2000: On the relationship between relative humidity and particle backscattering coefficient in the marine boundary layer determined with differential absorption lidar. *J. Geophys. Res.*, **105**, 4729–4742, doi:10.1029/1999JD901030.

- Wulfmeyer, V., M. Randall, A. Brewer, and R. M. Hardesty, 2000: 2- μm Doppler lidar transmitter with high frequency stability and low chirp. *Opt. Lett.*, **25**, 1228–1230.
- Wyngaard, J. C., 1992: Atmospheric turbulence. *Annu. Rev. Fluid Mech.*, **24**, 205–234.
- Wyngaard, J. C. and R. A. Brost, 1984: Top-down and bottom-up diffusion of a scalar in the convective boundary layer. *J. Atmos. Sci.*, **41**, 102–112.
- Wyngaard, J. C. and J. C. Weil, 1991: Transport asymmetry in skewed turbulence. *Phys. Fluids*, **3**, 155–162.
- Yaglom, A. M., 1977: Comments on wind and temperature flux-profile relationships. *Bound.-Layer Meteor.*, **11**, 89–102.
- Žeromskis, E., 2009: *Development of a Coherent Doppler Lidar System for Wind Measurements in the Planetary Boundary Layer*. Ph.D. Thesis, University of Leipzig, (unpublished manuscript).
- Žeromskis, E., U. Wandinger, D. Althausen, R. Engelmann, P. Rhone, and R. Foster, 2003: Coherent Doppler lidar for wind profiling in the lower troposphere. In: *Sixth International Symposium on Tropospheric Profiling: Needs and Technologies*, 14–20 September, Leipzig, Germany, U. Wandinger, R. Engelmann, and K. Schmieder, Eds., Institute for Tropospheric Research, 71–73.
- 2004: Coherent Doppler lidar for studies of transport and mixing processes in the lower atmosphere. In: *Reviewed and Revised Papers Presented at the 22nd International Laser Radar Conference (ILRC 2004)*, 12–16 July, Matera, Italy, G. Pappalardo, A. Amodeo, and B. Warmbein, Eds., European Space Agency, Noordwijk, The Netherlands, Vol. SP-561.
- Zilitinkevich, S., V. M. Gryanik, V. N. Lykossov, and D. V. Mironov, 1999: Third-order transport and nonlocal turbulence closures for convective boundary layers. *J. Atmos. Sci.*, **56**, 3463–3477.

List of symbols

Symbol	Unit	Description
Roman letters		
A_0	V	amplitude of the laser pulse [model $M(t)$]
A_{asym}	1	asymmetry factor
A_{chirp}	MHz μs^{-1}	laser frequency chirp
A_{dd}	V	factor of direct-detection contribution
A_{offset}	V	offset voltage
A_{trend}	V s^{-1}	linear trend
A_{t}	m^2	telescope area
\dot{a}	1	Ångström exponent
\dot{a}^β	1	backscatter-related Ångström exponent
a_K	1	Kolmogorov's constant
B_j	1	base functions
$C_{\varphi,\psi}$	$[\varphi] \times [\psi] \times \text{Hz}^{-1}$	cospectrum of φ and ψ
c	$\mu\text{g cm}^{-3}$	concentration of an air constituent
c_L	m s^{-1}	speed of light
D	m	horizontal lidar displacement
D_p	nm	particle diameter
$E^{\text{kin,t}}$	$\text{m}^2 \text{s}^{-2}$	turbulent kinetic energy
F_φ	$[\varphi] \times \text{m s}^{-1}$	turbulent flux of φ
F_p	$\mu\text{g m}^{-2} \text{s}^{-1}$	turbulent flux of particle mass
f_j	1	weight factors
g_p	m^{-1}	vector of optical particle properties
K_φ	$\text{m}^2 \text{s}^{-1}$	eddy diffusivity coefficient
K_p	m^{-1}	kernel functions
k	m^{-1}	wavenumber
$M(t)$	V	beating signal of the laser pulse

Symbol	Unit	Description
M_d	$\mu\text{g cm}^{-3}$	particle mass concentration
N_L	1	number of averaged laser shots
N_R	m^{-3}	number density of the nitrogen molecules
\check{n}	1	complex refractive index
$O(z)$	1	overlap function at distance z
P_0	W	average power of a laser pulse
$P_\lambda(z)$	W	lidar signal at distance z
$Q_{\varphi,\psi}$	$[\varphi] \times [\psi] \times \text{Hz}^{-1}$	quadrature spectrum of φ and ψ
R	nm	particle radius
$R_{\varphi\varphi}(l)$	$[\varphi^2]$	autocovariance function at lag l
$r_{\varphi\varphi}(l)$	1	autocorrelation function at lag l
r_{eff}	nm	effective particle radius
$S_\varphi(i)$	$[\varphi]^2 \times \text{Hz}^{-1}$	energy spectrum of φ at frequency bin i
$\check{S}_{\varphi,\psi}$	$[\varphi] \times [\psi] \times \text{Hz}^{-1}$	cross spectrum of φ and ψ
S_d	$\mu\text{m}^2 \text{cm}^{-3}$	particle surface area concentration
$S_{\lambda_0}^p$	sr	particle lidar ratio at wavelength λ_0
\check{S}_w	1	skewness of vertical velocity
T	s	length of a time series
t	s	time
Δt	s	sampling interval of a time series
u_1, u_2, u_3	m s^{-1}	velocity components
u_n	m s^{-1}	velocity perpendicular to a surface
V_d	$\mu\text{m}^3 \text{cm}^{-3}$	particle volume concentration
$v(R)$	$\mu\text{m}^3 \text{cm}^{-3} \text{nm}^{-1}$	particle volume concentration per interval dR
w	m s^{-1}	vertical wind speed
z	m	height above ground
z_i	m	height of the convective boundary layer
Greek letters		
α	Mm^{-1}	extinction coefficient
$\alpha_{\lambda_0}^p$	Mm^{-1}	particle extinction coefficient at wavelength λ_0
β	$\text{Mm}^{-1} \text{sr}^{-1}$	backscatter coefficient

Symbol	Unit	Description
$\beta_{\lambda_0}^p$	$\text{Mm}^{-1} \text{sr}^{-1}$	particle backscatter coefficient at wavelength λ_0
Γ_φ	$[\varphi]$	discrete Fourier transform of φ
γ_a	$[\varphi] \times \text{m}^{-1}$	countergradient
ε	$\text{m}^2 \text{s}^{-3}$	energy dissipation rate per mass unit
$\varepsilon^{\text{math}}$	$\mu\text{m}^3 \text{cm}^{-3} \text{nm}^{-1}$	mathematical residual error of $\nu(R)$
$\varepsilon_p^{\text{exp}}$	Mm^{-1}	error of measured optical data g_p
η_λ	1	receiver efficiency at wavelength λ
Θ	$^\circ\text{C}$	temperature
Θ_p	$^\circ\text{C}$	potential temperature
Λ	s or m	integral time or length scale
λ	m	wavelength
ν	Hz	frequency
ν_i	Hz	frequency at bin i
ν_0	Hz	frequency of transmitted laser radiation
$\Delta\nu_{\text{int}}$	MHz	intermediate frequency offset
$\Delta\nu$	MHz	frequency interval of a spectrum
$\Delta\nu_D$	MHz	Doppler shift
ξ_n	$\text{Mm}^{-1} \text{sr}^{-1}$ or ms^{-1}	linear fit of the time series of β^p or w
ρ_p	g cm^{-3}	particle density
$\frac{d\sigma(\pi, \lambda_0)}{d\Omega}$	$\text{Mm}^2 \text{sr}^{-1}$	Raman backscattering cross section of nitrogen
σ_φ^2	$[\varphi]^2$	variance of φ
$\sigma_{F, \text{samp}}^2$	$\mu\text{g}^2 \text{m}^{-4} \text{s}^{-2}$	sampling error variance of the turbulent flux
τ	1	aerosol optical depth
τ_L	ns	laser pulse length
ϕ	1	phase